THE UNIVERSITY OF CHICAGO

NANOPHOTONIC ENGINEERING WITH QUANTUM MATERIALS

A DISSERTATION SUBMITTED TO
THE FACULTY OF THE PRITZKER SCHOOL OF MOLECULAR ENGINEERING
IN CANDIDACY FOR THE DEGREE OF
DOCTOR OF PHILOSOPHY

BY
AMY BUTCHER

CHICAGO, ILLINOIS
JUNE 2022

TABLE OF CONTENTS

LIST OF FIGURES

LIST OF TABLES

ACKNOWLEDGMENTS

I would like to thank the mentors, colleagues, and friends who have made this doctoral journey possible. First, I am deeply grateful to my research advisor, Alex High, who took me on as his first student during the summer of 2017. When I initially toured the room that would become our lab with Alex, it was empty and carpeted. Today, one can hardly tell that it was ever not an optics lab. It has been uniquely satisfying to see this space and this group of people develop over the last few years. Along the way, Alex has consistently advocated for me, granted me flexibility, and empowered me to pursue the work in which I am most interested.

I also owe enormous gratitude to Rob Shreiner and Xinghan Guo, the two other students who joined the High lab from our cohort and who built the lab from the ground up. Everything I have done was in some way built off their work. Both Rob and Xinghan have established deep expertise in their areas and I am very lucky to have been able to rely on their help and guidance in my work. I'd also like to thank all of the members of the High lab who joined in subsequent years. Our group has managed to maintain a friendly and productive environment, even during difficult times, thanks to them.

The first period of grad school was challenging because we did not initially have post-docs or senior grad students to mentor us in the lab or in the clean room. However, there were certain students from other research labs who were generous with their time and who helped me grow my understanding and build my confidence in the early years. In particular, Moshe Dolejsi from the Nealey group and Alex Crook from the Awschalom group took the time to explain key clean room concepts to me and to help me troubleshoot my fab processes. Kevin Miao and Alex Bourrassa, also from the Awschalom group, helped us early on by sharing their expertise in hardware automation, which enabled virtually all of our optical experiments.

None of the work in this thesis could have been completed without the help of the Pritzker

Nanofabrication Facility (PNF) staff. There are always unforeseen setbacks in clean room work, and we are lucky to have such responsive and knowledgeable people keeping our facility running smoothly. I owe a special thank you to the PNF technical director, Peter Duda, whose deep knowledge and experience is a major asset any time I am having difficulty with a particular process or tool. On top of that, Peter's attitude and energy in the clean room always made the work much more enjoyable.

Many colleagues at other institutions were instrumental to completing research projects here at U. Chicago. At the Institute for Photonic Sciences in Barcelona, Professor Darrick Chang and Dr. David Li provided theoretical input to a range of projects, which helped build our physical intuition and guide experiments. At Argonne National Laboratory, Joe Heremans and Nazar Delegan developed the diamond chemical vapor deposition which we relied on to build our diamond membrane platform.

Lastly, I would like to thank my friends and family for their support and guidance. I am fortunate that both of my parents have worked in science labs and truly understand the day-to-day frustrations of lab work when I vent to them, especially during times of "ojom". At U. Chicago, I've met some of the cleverest and funniest people I know and made wonderful friends. In Hyde Park dive bars, on the softball field, and on the shores of Lake Michigan, I have many happy memories that I will take with me. Finally, I would not be where I am now, both literally and figuratively, without the support of (Dr!) Peter Bennington.

ABSTRACT

Nanophotonic engineering offers powerful methods of tailoring light-matter interactions. By manipulating optical environments at the nanoscale, we can influence the rate, direction, and spectral distribution of optical emission. This thesis describes the foundations of nanophotonic engineering and discusses methods to tailor the optical response of solid-state quantum materials. We target color centers in diamond membranes and two-dimensional semiconductors, two classes of optical emitters that offer applications in quantum information processing, sensing, and integrated optoelectronics. Throughout this work, we emphasize the development of nanofabrication processes which are compatible with these materials and enable sub-wavelength control of their optical environments. Chapter 1 introduces the fundamentals of nanophotonic engineering and provides background on the material systems explored in this work. Chapter 2 describes the benchtop optical experimental methods that enable many of the measurements presented later. Following these introductory chapters, Chapter 3 details our approach to fabricating integrated photonics using templated atomic layer deposition of TiO_2. Chapter 4 presents work that leverages this nanofabrication process to integrate photonic devices with a range of quantum materials. Chapter 5 extends this approach to a novel device geometry, multi-resonant bullseye antennas. In Chapter 6, we discuss the application of off-resonant planar cavities to extend the lifetimes of optical excitations in two-dimensional semiconductors. Finally, Chapter 7 provides a summary and outlook for this work.

Chapter 1

Introduction

1.1 Principles of nanophotonic engineering

Spontaneous emission is one of few truly quantum processes that we directly experience on a daily basis. From fluorescent lightbulbs to fireflies, many natural and artificial light sources are generated by the relaxation of electrons in excited atoms or molecules. Before the development of quantum electrodynamics, it was believed that spontaneous emission was an intrinsic property of materials.[1,2] Insights into quantum uncertainty and vacuum field fluctuations revealed that these fluctuations in fact induce the electronic transitions that generate spontaneous emission.[3] This fully quantum mechanical description of light-matter interaction remains one of the great achievements of the twentieth century quantum revolution.

Due to its field dependence, the characteristics of spontaneous emission are determined not only by the electronic properties of the emitter, but also by the properties of its local electromagnetic environment. Remarkably, an atom's spontaneous emission profile can change based on the environment in which it is embedded.[2,4] The rate, wavelength, and spatial profile of emission may all be influenced by the atom's surroundings. Based on this realization, mid-century physicists proposed a series of thought experiments to investigate the implications of quantum theory on the emission of light.[5] What would happen if we could detect the light emitted by a single atom? How would its emission change if it were placed near a mirror, or inside of a box? These questions, although revealing, were treated as purely theoretical exercises at the time.

Today, these thought experiments have become reality. Individual atomic systems can be precisely manipulated in a range of physical settings, from vacuum environments to the solid state. Laser trapping and cooling can isolate neutral atoms,[6] while ion implantation and new material growth techniques can define atom-like defects inside crystal hosts.[7] Ultrafast lasers and photodetectors probe these emitters' optical behavior with increasing spectral and time resolution. Meanwhile, advanced nanofabrication methods yield sub-wavelength dielectric and plasmonic structures which can modify nearby electromagnetic fields, directing spontaneous emission profiles.[4]

These advancements not only allow fundamental investigations of light-matter interaction, but also enable a broad range of new technologies. By engineering nanophotonic environments, the characteristics of spontaneous emission can be tailored for applications in optoelectronics,[8,9] bio-sensing,[10] and quantum information.[11–13] Whether the aim is to entangle spin and optical degrees of freedom, to generate many identical photons, or to detect subtle changes in molecular environments, many exciting avenues of research are enabled by engineering light emission.

1.1.1 Fermi's golden rule

The foundation of emission engineering is Fermi's golden rule (Eqn. 1.12), which describes the spontaneous emission rate of a single atom in a given optical field. Deriving this equation requires considering the time-dependent perturbation of an optical field on the state of a two-level atom. The total Hamiltonian of the system is the sum of the unperturbed Hamiltonian and an additional interaction term, $H = H_0 + H_I$. When the perturbing Hamiltonian is turned on, the state of the system can be expressed as a time-varying linear combination of the stationary eigenstates of H_0:

$$|\psi(t)\rangle = \sum_n a_n(t)\, e^{-iE_n t/\hbar}\, |n\rangle \tag{1.1}$$

Here, $|n\rangle$ are stationary states of H_0 and E_n are the corresponding eigenvalues such that $H_0\,|n\rangle = E_n\,|n\rangle$. To determine the time-varying behavior of the atom-photon system, and therefore the atomic transition rate, the time-dependent coefficients $a_n(t)$ must be found.

The state evolves according to the time-dependent Schrodinger equation:

$$H\left|\psi(t)\right\rangle = i\hbar\frac{\delta}{\delta t}\left|\psi(t)\right\rangle \tag{1.2}$$

Inserting the total Hamiltonian and the expression for $\left|\psi(t)\right\rangle$ yields a system of differential equations, one for each $\left|n\right\rangle$:

$$(H_0 + H_I - i\hbar\frac{\delta}{\delta t})\sum_n a_n(t)\, e^{-iE_nt/\hbar}\left|n\right\rangle = 0 \tag{1.3}$$

Operating on the left with the Hamiltonian and time derivative and then cancelling terms leads to:

$$i\hbar\sum_n \frac{\delta a_n(t)}{\delta t}\, e^{-iE_nt/\hbar}\left|n\right\rangle = \sum_n a_n(t)\, e^{-iE_nt/\hbar}\, H_I\left|n\right\rangle \tag{1.4}$$

Next, multiplying each side with the conjugate of another unperturbed eigenstate, labelled $\left\langle k\right|$, gives the equation:

$$\frac{\delta a_k(t)}{\delta t} = \frac{-i}{\hbar}\sum_n a_n(t)\, e^{-i\omega_{nk}t}\left\langle k\right| H_I\left|n\right\rangle \tag{1.5}$$

where $\omega_{nk} = (E_n - E_k)/\hbar$.

We can see from this equation that when $H_I = 0$, the atom-photon state will not change. The derivatives that describe the time evolution of the system become nonzero only due to the influence of the optical field. Figure 1.1 illustrates the energy levels of the system and the available decay pathways from a single initial state with one excited atom and no emitted photons to a series of discrete states with the atom in its ground state and one emitted photon in a mode with frequency ω and wavevector $\boldsymbol{k}$. Labelling the initial state of the system as $\left|i\right\rangle$ and all the other states as $\left|k\right\rangle$, we can state $a_k(t) = \delta_{i,k}$ when there is no field interaction. Provided that the field interaction Hamiltonian H_I can be treated with first-order perturbation theory, we can insert this zero-order value into the above equation to solve for the first-order correction.

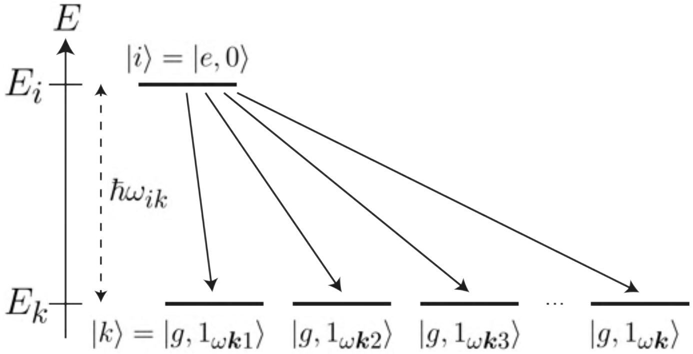

Figure 1.1 – Decay pathways for a two-level atom. The initial state $|i\rangle$ represents a single excited atom and no emitted photons. All other states $|k\rangle$ to which the system can evolve are those with the atom in its ground state and one emitted photon in a mode labelled by frequency ω and wavevector $\boldsymbol{k}$. The electronic energy difference between $|i\rangle$ and any accessible $|k\rangle$ is the energy of the emitted photon, $\hbar\omega_{ik}$.

$$\frac{\delta a_k(t)}{\delta t} = \frac{-i}{\hbar} \langle k| H_I |i\rangle \; e^{-i\omega_{ik}t} \tag{1.6}$$

Assuming that H_I does not vary over the timescale of the atomic decay, integrating with respect to time leads to an expression for the coefficients $a_k(t)$:

$$a_k(t) = \frac{i}{\hbar}\int_0^t \langle k| H_I |i\rangle \, e^{-i\omega_{ik}t} dt = \frac{i}{\hbar\omega_{ik}} \langle k| H_I |i\rangle \, (e^{i\omega_{ik}t} - 1) \tag{1.7}$$

The probability associated with a particular state $|k\rangle$ is:

$$|a_k(t)|^2 = \frac{4}{\hbar^2\omega_{ik}^2} | \langle k| H_I |i\rangle |^2 \sin^2(\omega_{ik}t/2) \tag{1.8}$$

Each ground state $|k\rangle$ represents a pathway for spontaneous decay, and they must all be considered collectively in order to describe the atomic transition rate. To calculate the total time-dependent probability that the atom transitions to its ground state and emits a photon, we sum the individual probabilities:

$$P(t) = \sum_k |a_k(t)|^2 = \frac{4}{\hbar^2} \sum_k | \langle k| H_I |i\rangle |^2 \frac{\sin^2(\omega_{ik} t/2)}{\omega_{ik}^2} \tag{1.9}$$

To account for the continuum of available photonic states rather than a discrete series of $|k\rangle$, we can replace this summation with an integral. Importantly, the probability for an atom to decay to its ground state depends on the number of photons that the surrounding optical field can accommodate at the energy difference between those atomic states, $\hbar\omega_{ik}$. Using $\rho(\omega)$ to represent the density of photon states per unit energy at a particular frequency ω, we can integrate over frequency:

$$P(t) = \frac{4}{\hbar^2} \int_{-\infty}^{\infty} | \langle k| H_I |i\rangle |^2 \frac{\sin^2(\omega_{ik} t/2)}{\omega_{ik}^2} \rho(\omega) d\omega \tag{1.10}$$

Here, the integral includes the full continuum of photon states available with the photonic density of states weighting each of these based on the conditions of the surrounding optical field. The main nonzero contribution to this integral is restricted to a small region from $\omega = -\pi/t$ to $\omega = \pi/t$. Assuming that $\rho(\omega)$ does not vary substantially over this region, it can be brought outside of the integral, as can the Hamiltonian overlap term. Integrating the remaining function yields:

$$P(t) = \frac{2\pi t}{\hbar^2} |M_{ik}|^2 \rho(\omega) \tag{1.11}$$

where the transition matrix element $M_{ik} = \langle k| H_I |i\rangle$. Finally, taking the time derivative gives the total atomic transition rate, which is also Γ, the spontaneous emission rate of the single atom system:

$$\Gamma = \frac{dP(t)}{dt} = \frac{2\pi}{\hbar^2} |M_{ik}|^2 \rho(\omega) \tag{1.12}$$

This result is known as Fermi's golden rule. It states that the spontaneous emission rate of an excited atom is constant in time and depends on both the properties of the local optical field as well as the properties of the emitter itself. We can unravel these intrinsic and extrinsic contributions by expanding the Hamiltonian overlap term:

$$|M_{ik}|^2 = \langle \boldsymbol{\mu}_{ik} \cdot \boldsymbol{E} \rangle \tag{1.13}$$

where $\boldsymbol{\mu}_{ik}$ is the electric dipole moment that corresponds to the transition between atomic states $|i\rangle$ and $|k\rangle$ and $\boldsymbol{E}$ is the local optical field. Intuitively, because the atom-field interaction Hamiltonian multiplies the atomic dipole moment with the local electric field, atomic energy levels with larger associated dipole moments will be more susceptible to transitions induced by field fluctuations.

Using Eqn. 1.12 and 1.13, we can calculate the spontaneous emission rate of an atom in a vacuum. In this case, the local optical field is the zero point vacuum field, and:

$$\langle \boldsymbol{\mu}_{ik} \cdot \boldsymbol{E} \rangle^2 = \frac{1}{3}\mu_{ik}^2 E_{\text{vac}}^2 = \frac{1}{3}\mu_{ik}^2 \Big(\frac{\hbar\omega}{2V\epsilon_0}\Big) \tag{1.14}$$

An extra factor of 1/3 comes from averaging over all possible dipole orientations. In free space, the photon density of states can be calculated by considering how many photon states with different k values can be accomodated by a finite space of volume V. As shown in Ref. [14], the photon density of states in free space is:

$$\rho_0(\omega) = \frac{\omega^2 V}{\pi^2 c^3} \tag{1.15}$$

which, combined with Eqn. 1.14, leads to the free space spontaneous emission rate:

$$\Gamma_0 = \frac{\omega_0^3 \mu_{ik}^2}{3\pi\epsilon_0\hbar c^3} \tag{1.16}$$

Provided that the transition frequency ω_0 and the transition dipole μ_{ik} are known, the emission rate of an atom in a homogeneous, free space environment can be calculated using this equation. With this value as a reference, the effect of a particular environment on spontaneous emission can be quantitatively assessed relative to free space.

1.1.2 Modifying emission: interfaces and cavities

Structured environments impose boundary conditions on optical fields, modifying the spontaneous emission of nearby emitters. An intuitive interpretation of this phenomenon is that a dipole emitter is influenced by its own field which is scattered from the local environment back to the dipole position. This semiclassical understanding clarifies why an atom's emission rate is tied inextricably to the condition of its surroundings. It is useful to note that while a quantum treatment is required to accurately calculate spontaneous emission rates, a classical treatment can still be used to determine the *relative* emission rate in comparison with a reference system.[1] In other words, the ratio of an atom's emission rate to its free space value is equal in both the classical and quantum treatments:

$$\frac{\Gamma}{\Gamma_0} = \frac{P}{P_0} \tag{1.17}$$

Here, P and P_0 represent the power radiated by an oscillating classical electric dipole. Using this framework, the spontaneous emission rate of a dipole can be expressed:[1]

$$\frac{\Gamma}{\Gamma_0} = \frac{\mathrm{Im}[\boldsymbol{p}^* \cdot \boldsymbol{E}(\boldsymbol{r}_0)]}{\mathrm{Im}[\boldsymbol{p}^* \cdot \boldsymbol{E}_{\text{free}}(\boldsymbol{r}_0)]} \tag{1.18}$$

where Γ_0 is the decay rate in free space and Γ is the total emission rate in an inhomogeneous environment. Here, $\boldsymbol{p}e^{-i\omega t}$ describes a classical oscillating point dipole representing a two-level atomic system, $\boldsymbol{E}(\boldsymbol{r}_0)$ is the total field at the dipole location including reflections from the surrounding environment, and $\boldsymbol{E}_{\text{free}}(\boldsymbol{r}_0)$ is the dipole field in a uniform medium at the dipole location.

The simplest inhomogeneous environment is a single planar interface. In 1966, the foundational Drexhage experiments investigated the effect of planar interfaces on the spontaneous decay rate of molecules.[15] These experiments demonstrated how, depending on the dipole-interface separation and the dipole orientation, emission rates may be increased or decreased compared to free space. Figure 1.2 illustrates these dependencies for the case of a single silver interface. For a dipole parallel to the interface, a standing wave is formed from the reflection off the silver surface, which causes the emission rate to alternately be increased or decreased as the dipole moves towards the surface. At small emitter-metal separations, the dipole couples significantly to plasmonic oscillations in the metal, and the (nonradiative) emission rate is substantially increased. Similar features can be seen in the perpendicular dipole case, although the standing wave is much less apparent due to the lack of s-polarized field contributions. Additionally, the perpendicular dipole couples substantially to propagating surface plasmon polaritons (SPPs) at small separations, as these guided modes generally have out-of-plane polarizations.

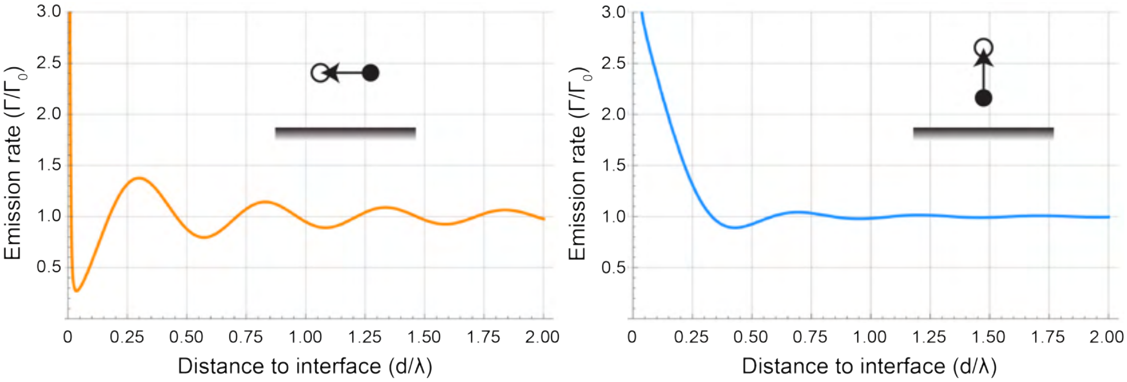

Figure 1.2 – Dipole emission near an interface. Normalized emission rates for dipoles oriented parallel (left) and perpendicular (right) to a silver plane are plotted as a function of the emitter-interface separation, which is normalized to wavelength.

To calculate emission rates in inhomogeneous environments as in Figure 1.2, the dipole field can be decomposed into its plane wave components, with s and p polarizations considered separately. Each of these plane wave contributions is multiplied by the appropriate Fresnel reflection coefficient, which is a function of both polarization and wavevector. The reflected plane wave components are then integrated to solve for the total field at the emitter position. Propagating surface modes are captured by poles in the reflectivity functions. Further details about the fundamentals of these calculations can be found in Ref. [16] and

[1].

Beyond the single interface case, more dramatic changes to dipole emission rates can occur in environments with multiple interfaces. In particular, if a parallel dipole emitter is centered between two metallic planes, its spontaneous emission can be entirely suppressed. This emission cutoff effect was experimentally demonstrated in 1987 by Jhe et *al.*, who used two mirrors separated by a 1.1 µm gap to probe the anisotropic impact of the cavity on emission from gaseous atoms.[17] Figure 1.3 illustrates the impact of the dual-interface cavity on parallel dipole emission as a function of interface-interface separation. As before, at small separations, the dipole emission rate is enhanced by emission into guided modes and nonradiative excitation of metallic electrons. Critically, when the mirror separation is near $\lambda/4$, destructive interference of the dipole field reflected from either interface eliminates any modes into which the dipole can emit and the emission rate plunges to zero. As the mirrors are brought further apart, the space between them eventually becomes large enough to accomodate a resonant mode that enhances the dipole emission compared to free space. With further increasing mirror separation, a sawtooth pattern emerges based on the overlap of the available cavity modes with the dipole emission wavelength.

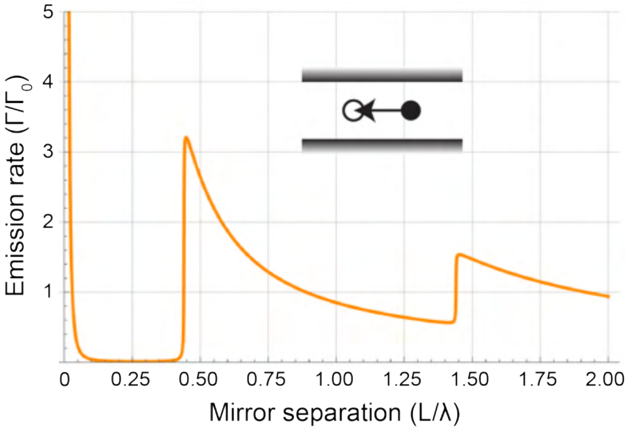

Figure 1.3 – Parallel dipole emission in a planar cavity. The normalized emission rate for a dipole oriented parallel to two silver planes is plotted as a function of the mirror-mirror separation, which is normalized to wavelength.

Perhaps the most technologically significant structures which are commonly used to modify emission rates are optical cavities resonant with targeted optical transitions. By confining and enhancing resonant fields, these devices can dramatically increase spontaneous emission rates for applications in sensing, quantum information, and more. The photon density of states for a resonant cavity is a Lorentzian function:

$$g(\omega) = \frac{2}{\pi \Delta\omega_c} \frac{\Delta\omega_c^2}{4(\omega - \omega_c)^2 + \Delta\omega_c^2} \tag{1.19}$$

where the cavity has a single mode of frequency ω_c and its resonance has a half width $\Delta\omega_c$. We can consider a single mode when only one resonant mode of the cavity is close in frequency to the emission frequency of the relevant emitter, even if there are other cavity modes that are further away in frequency. Evaluating the density of states when the dipole emission frequency, ω_0, is equal to the cavity resonance frequency yields:

$$g(\omega_0) = \frac{2}{\pi \Delta\omega_c} = \frac{2Q}{\pi \omega_0} \tag{1.20}$$

where Q is the quality factor of the resonator. Combining this equation with the result from Eqn. 1.14 for the transition matrix element of the emitter and assuming the optical dipole moment is aligned to the cavity field gives:

$$\frac{\Gamma}{\Gamma_0} = F_P = \frac{3Q(\lambda/n)^3}{4\pi^2 V} \tag{1.21}$$

Here, F_P is referred to as the Purcell factor and V represents the mode volume of the cavity. Cavities with higher quality factors and lower mode volumes generate larger Purcell factors and therefore brighter dipole emission. We note that Equation 1.21 is valid provided the atom-cavity system is in the so-called weak coupling regime. In the strong coupling regime, when the coupling rate between the emitter and cavity is substantially larger than the cavity decay rate and the emission into non-cavity modes, more exotic effects occur. The emitter and cavity modes can hybridize, leading to vacuum Rabi splitting. More information about strong coupling, its applications, and the experimental challenges with achieving this condition can be found in Ref. [5].

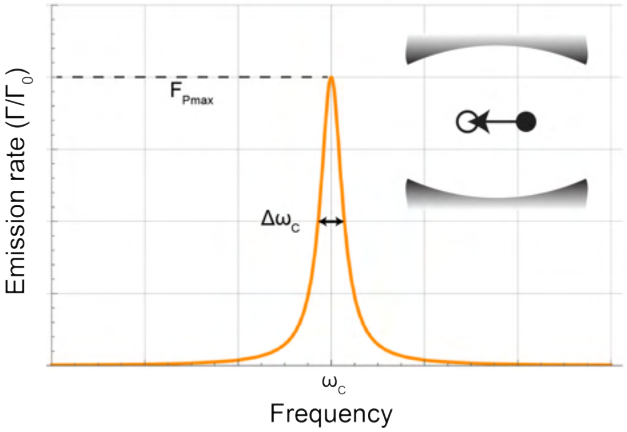

Figure 1.4 – Dipole emission in a resonant, single-mode cavity. The photon density of states and therefore the emission rate enhancement is a Lorentzian function which peaks at ω_c and has a FWHM linewidth of ω_c

The technological impact of Purcell enhancement is high, as this effect can increase optical sensing bandwidths, enable coherent light-matter interactions, and create spin-photon interfaces for quantum networks. However, fabricating high quality factor cavities at visible wavelengths can be challenging because <100 nm critical dimensions are required. Rather than shrinking Fabry-Perot cavities formed by planar or curved mirrors down to these length scales, photonic crystals are often leveraged to confine resonant optical modes, as will be described in the next section.

To summarize, spontaneous emission rates can be modified by structured optical environments for a range of technological applications. The three most relevant inhomogeneous environments for nanophotonic engineering are single interfaces, off-resonant planar cavities, and resonant cavities. These three canonical structures are illustrated in Figure 1.5, and each will be relevant to the work presented in Chapters 3-6.

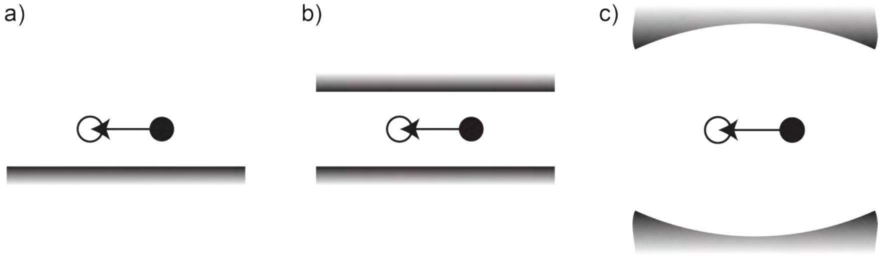

Figure 1.5 – Dipole emitters in three basic geometries: a single interface (a), a planar off-resonant cavity (b), and a resonant single mode cavity (c).

1.1.3 Photonic crystal cavities

Photonic crystal cavities (PhCCs) illustrate how advanced nanofabrication methods enable new approaches to manipulating light-matter interactions, and they are a key element in the library of nanophotonic devices. Here, we highlight the properties of PhCCs and their basic operational theory as a way to demonstrate nanophotonic engineering principles.

Photonic crystals are materials in which the index of refraction is periodically modulated. This index modulation may extend in one, two, or three dimensions, although 1D and 2D photonic crystals are more experimentally accessible. The most basic photonic crystal can be constructed by alternating thin films of two materials with different refractive indices. These multi-layer structures are often used as optical coatings to achieve extremely high reflectivity, as in Bragg mirrors, or extremely low reflectivity, as in anti-reflection coatings.

To understand the operating principle of 1D Bragg mirrors, we can consider the phase accumulated by waves which reflect from each interface in the layered film. As illustrated in Figure 1.6a, a portion of light incident on each interface is reflected and interferes with all other reflected rays. The phase accumulated by each ray includes contributions from propagation through each material and an additional π phase if the ray is reflected from a higher index material to a lower index one, a condition which alternates at each layer. When the thickness of each layer is such that the phase accumulated through propagation is $\pi/2$, each reflected ray will constructively interfere, leading to extremely high reflectivity. As a rule of thumb, the layers are designed to have thicknesses $d_1 = \lambda/4n_1$ and $d_2 = \lambda/4n_2$ to meet this condition.

A more sophisticated understanding of photonic crystals can be developed by drawing an analogy to electron wave propagation in crystals. The periodic potential generated by ions forming a crystal lattice creates an electronic bandgap; the electron wavefunctions are constrained by the periodic boundary conditions imposed by the ions, which restricts their available k-vectors. Likewise, in a photonic crystal, the periodic index of refraction constrains the propagation of light waves through the medium and leads to a photonic bandgap. The Bloch formalism that describes electron wave propagation carries over directly to the propagation of electromagnetic waves in photonic crystals.[18] Figure 1.6b illustrates two symmetric electric field distributions that are allowed in a 1D photonic crystal, which are separated in energy by a photonic bandgap.

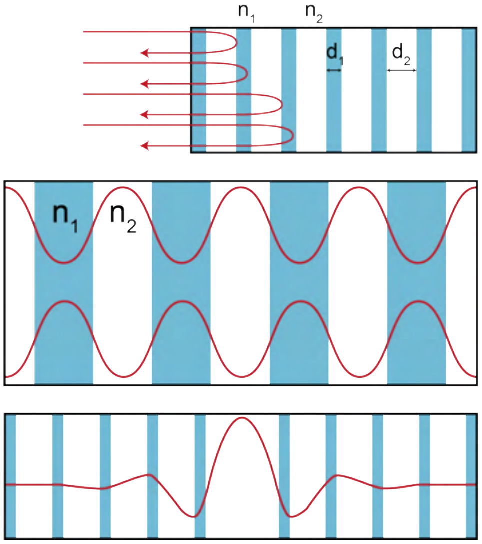

Figure 1.6 – Operation principle of photonic crystal cavities. (Top) Individual light rays reflected off a Bragg mirror constructively interfere. The labels n_1 and n_2 denote the two refractive indices in the periodic structure, and d_1 and d_2 denote the widths of the alternating layers. (Center) Two symmetric distributions of electric field propagating in a 1D photonic crystal, separated by a photonic band gap. (Bottom) A defect in a 1D photonic crystal introduces a localized region of high electric field

To generate a PhCC, a defect is introduced in the photonic crystal, which creates a local optical mode that is otherwise forbidden by the photonic band gap. This localized mode is directly analogous to an isolated electronic state within a crystal bandgap that is created by a lattice defect. We can also think of this structure as bringing two Bragg mirrors into close proximity. As light reflects between these mirrors, the electric field between them intensifies before eventually leaking out. With increasing reflectivity, the cavity resonance becomes longer lived and its quality factor increases. Consequently, the resonance linewidth narrows, as only wavelengths that are very close together will maintain coherence and constructively interfere over long times.

In most applications, photonic crystals are implemented in 1D or 2D configurations. Total internal reflection provides spatial confinement in the directions without periodic index modulation to create a 3D region of field confinement. The surrounding medium therefore needs to be sufficiently low index to maintain waveguiding for these devices to function. A wide range of photonic crystal geometries have been explored, some of which are illustrated in Figure 1.7. In the 1D case, holes or fins periodically spaced along a waveguide modulate its effective refractive index. The period of these structures is gradually tapered to create a cavity region. In 2D, PhCCs are most often fabricated by creating periodically spaced holes in a 2D slab. Both 1D and 2D devices are typically fabricated through subtractive processing, often using plasma etching. However, as we will discuss in Chapter 3, there can be advantages to using additive methods when it comes to integrating photonic devices with sensitive substrates.

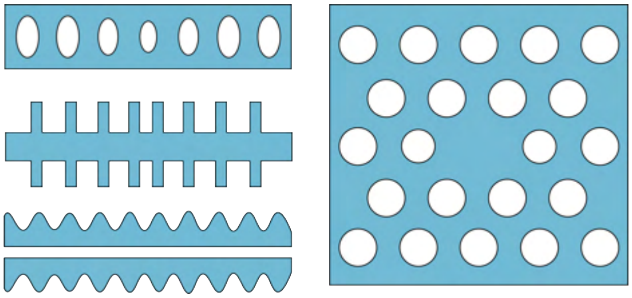

Figure 1.7 – 1D and 2D photonic crystal cavity designs.

Beyond PhCCs, a range of other nanophotonic devices can be used to generate optical resonances on the nanoscale. These include ring resonators, whispering gallery mode resonators, plasmonic bowtie antennas, Mie resonators, and more. In other applications, integrated photonic devices are used to direct the flow of light or to manipulate its phase, as in waveguides, grating couplers, Mach-Zehnder interferometers, and zone plates. Each of these devices can potentially be integrated with quantum and low-dimensional materials to enable new applications.

1.2 Background on quantum materials

As an umbrella term, the phrase "quantum materials" can have different meanings depending on context. In this work, we use the term to refer to low-dimensional material systems with properties that are defined by quantum mechanics. Specifically, the material systems we target are optically active point defects in diamond and two-dimensional semiconductors. Each of these systems offers unique opportunities and challenges for nanophotonic engineering.

1.2.1 Point defects in diamond for quantum optical networks

Recent advances in the control of quantum systems have revealed the potential for technologies which capitalize on the strangeness of non-classical phenomena. From powerful information processing[19] and simulation[20] to ultra-precise sensing[21] and invulnerable communication,[22] quantum technology promises to deliver a wide range of new capabilities. To deliver these applications, we require the ability to tailor interactions between distinct quantum systems and to scale those interactions to encompass many connected and controllable quantum nodes. Optical quantum networks are a promising avenue to achieve this goal. Using photons, which can travel long distances with minimal decoherence, optical networks are capable of transmitting quantum information and distributing entanglement.[23–25] They are also compatible with existing telecommunication fiber technology[26,27] and thus offer the possibility of long-range quantum communication.

The fundamental building block of quantum optical networks, as they were originally proposed,[28] is the atom-cavity node. As discussed earlier in Chapter 1, nano-optical cavities can confine light in a volume on the order of one cubic wavelength, which greatly increases the interaction cross section of a single photon with an atom. In quantum networks, this enhanced light-matter interaction serves two functions. First, through the Purcell effect,[2] cavities can significantly increase spontaneous emission rates. Greater spontaneous emission of photons leads to increased entanglement generation rates in communication networks and larger bandwidths for sensing applications. Second, cavity-enhanced light-matter interaction enables the manipulation of internal atomic states with individual photons. Atoms and cavity photons can interact through resonant scattering processes[29] and coherent energy swapping,[28] enabling quantum logic gates.[30] To form an integrated network, atom-cavity nodes are linked via optical channels, allowing quantum states to be transferred and for entanglement to be distributed between nodes.

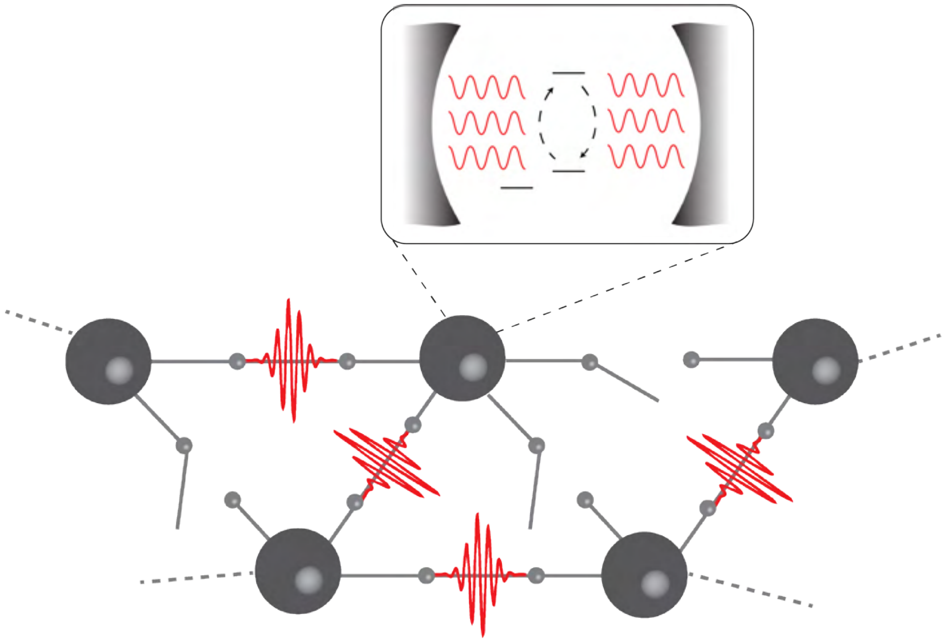

Figure 1.8 – A quantum optical network. Switchable optical channels connect atom-cavity nodes which provide spin-photon interfaces.

Experiments in the last decade have demonstrated necessary ingredients of quantum optical networks in a variety of material systems. Arguably the most developed of these platforms is trapped neutral atoms, in which deterministic quantum state transfer, entanglement distribution, and quantum logic gates have been demonstrated.[31,32] However, networks of trapped atoms are not easily integrated with nanoscale electrical and optical devices and are difficult to scale. Solid-state platforms, meanwhile, leverage mature nanofabrication techniques to offer straightforward integration and scalability.[33] Optically active point defects are particularly promising for quantum applications, as they can be created with highly reproducible emission profiles and are easily addressed by external fields.[34] Although inhomogeneous broadening can complicate quantum protocols which require identical photons, remarkable achievements have been made using solid-state defects for optical networking.[27,35]

Due to its wide electronic bandgap and rigid crystal lattice, diamond supports a variety of fluorescent point defects which can be isolated as single photon emitters. Among these, by far the most widely studied is the nitrogen-vacancy center (NV), which is comprised of a substitutional nitrogen atom next to a vacancy in the diamond carbon lattice. NVs exhibit long spin coherence times, even at room temperature, and possess spin-conserving optical transitions which offer an efficient means of initialization and read-out.[36] These features make them excellent sensors for nanoscale magnetometry[37] and thermometry.[38] However, zero phonon line (ZPL) emission constitutes only $\approx 4\%$ of total emission from NVs. While this fraction can be enhanced via integration with photonic crystal cavities,[39] it remains an impediment to reliable generation of indistinguishable photons from distinct NVs. Moreover, because NVs possess a nonzero static electric dipole moment, their optical transitions shift in response to local variations in electric field and strain.[40] Dephasing due to local charge fluctuations is even more apparent for NVs localized within nanostructures,[39] where they are closer to surfaces. This combination of low ZPL emission and spectral diffusion hinders the use of NVs for photon-mediated entanglement between quantum nodes.

On the other hand, defects with inversion symmetry, such as the silicon-vacancy (SiV) and germanium-vacancy (GeV) centers in diamond, have no permanent static dipole moment and therefore minimal spectral diffusion and inhomogeneous broadening.[41–43] These group IV defects consist of an interstitial impurity atom which sits between two vacancies in the diamond lattice. The SiV and GeV belong to the D_{3d} point group, which has the further consequence that their optical transitions occur between states with similar charge densities.[44] As a result, due to the Franck-Condon principle, the SiV and GeV optical transitions do not couple strongly to local lattice vibrations. Both of these defects therefore show strong ZPL emission, accounting for around 70% of photons emitted. They are also very bright, saturating at 100-200 kcps for individual emitters.[42] With strong and stable emission spectra, this new class of defects are excellent candidates for integration in quantum optical networks.

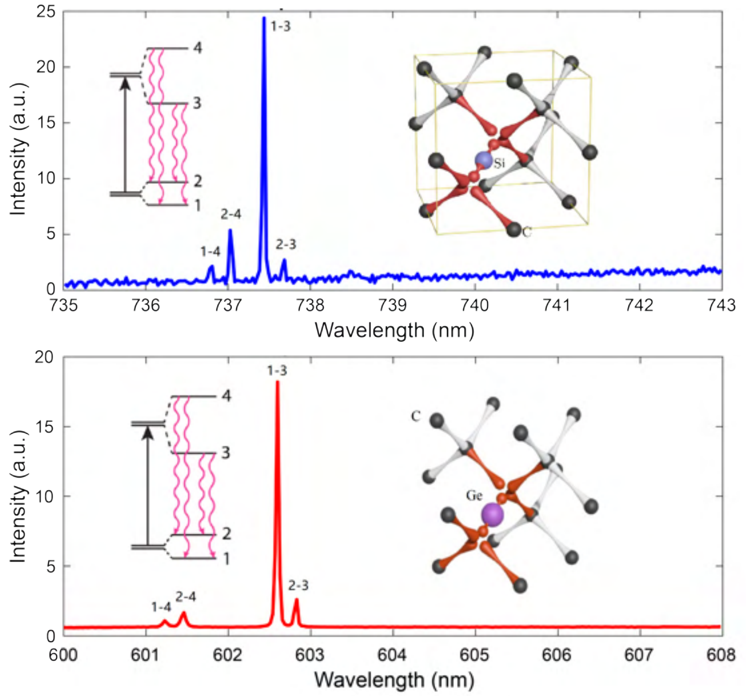

Figure 1.9 – SiV and GeV spectra in a diamond membrane. For both defects, four peaks correspond to transitions between electronic states split by spin-orbit coupling. Insets show the interstitial impurities in the diamond lattice corresponding to each color center. Figure credit Xinghan Guo.

The electronic structure of both the SiV and GeV features spin-1/2 ground and excited states with double orbital degeneracy that is split by spin-orbit coupling, as illustrated in Figure 1.9. This splitting creates a four-level energy structure with optical transitions around 602 nm for the GeV and 737 nm for the SiV. Since germanium is heavier than silicon, the GeV's spin-orbit splitting is larger than that of the SiV (though less than that of the more recently discovered tin-vacancy[45,46] and lead-vacancy centers[47,48]), which is advantageous for coherent microwave control of spin states and potential spin-photon interfacing.[49] It should be noted that the spin coherence of the group IV color centers is modest due to acoustic phonon scattering between the two ground orbital branches.[12] Dilution refrigerators are generally required for experiments relying on spin manipulation of these defects, a key disadvantage in comparison to the NV center.

Recent work exploring the optical coherence properties of group IV color centers has revealed their promise for quantum networking applications despite their relatively low spin coherence. For example, SiVs have been shown to produce identical photons in bulk diamond[43] and have been implanted in nanoscale waveguides and photonic cavities.[35,50] For SiVs in nanophotonic structures, inhomogeneous broadening of around 20 GHz was observed. Despite this broadening, researchers were able to generate indistinguishable photons from these defects through tunable Raman transitions and used this method to generate two qubit entanglement for SiVs in an optical cavity.[35] Recent interrogations of the GeV show that, unlike the SiV, its excited state lifetime does not depend strongly on temperature and shows greater sensitivity to local photonic environments.[51] These observations indicate a high quantum efficiency, making the GeV particularly promising for use in integrated photonic quantum networks. GeVs implanted in diamond waveguides demonstrated linewidths ($\approx$ 73MHz) slightly less than three times the lifetime-broadened value ($\approx$ 26 MHz).[51] In these waveguide structures, researchers showed optical Rabi oscillation decay times of approximately 6.5 ns at 5K. Impressively, in one experiment, a single GeV was able to extinguish 18% of a weak, resonant laser in one pass through a waveguide.[51] These results demonstrate the potential for high cooperativity interfaces between single GeVs and nanophotonic cavities, which would enable deterministic interactions with single photons.

More recently, GeVs have also been incorporated into micro-ring and micro-disk optical resonators fabricated from 300 nm-thick diamond membranes.[52] Ensembles of GeVs were integrated into membranes during growth, and micro-structures were subsequently patterned via etching into the diamond. The quality factor of these micro-resonators was only 1500, yielding a fairly modest fourteen times emission rate enhancement from the GeVs. Still, integration of GeVs with photonic resonators is a significant step towards implementing these defects in optical quantum networks, and incorporation into membranes will allow more efficient optical manipulation of these emitters compared to those in bulk diamond.

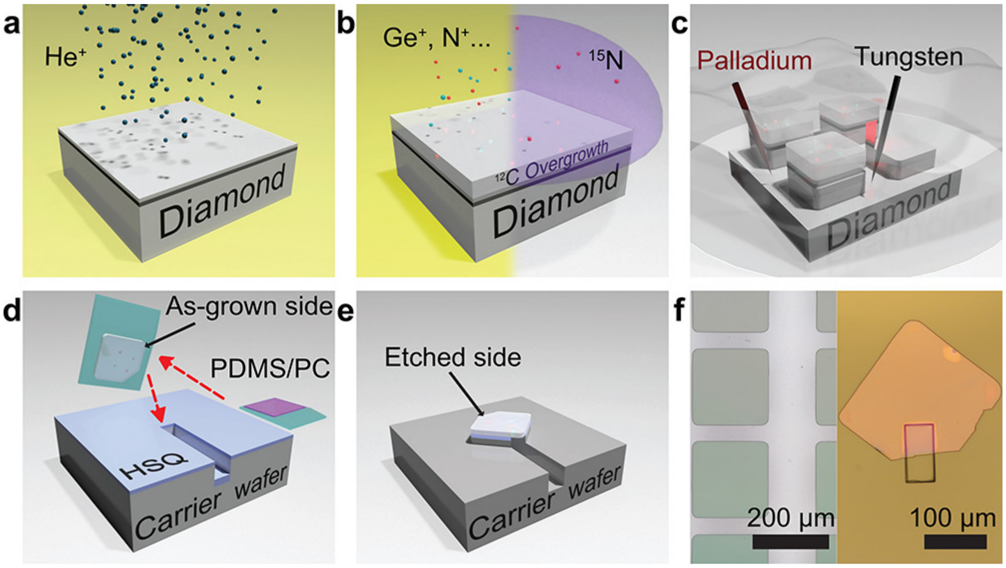

Figure 1.10 – Diamond membrane fabrication and integration. (a) He+ implantation and annealing forms the membrane and a graphitized layer underneath. (b) Color centers are incorporated either through in-situ doing during isotopically purified overgrowth (right) or ion implantation after overgrowth (left). (c) Membranes are undercut via electrochemical etching. (d) The membrane is picked up by a PDMS/PC stamp (green/purple), flipped onto another PDMS stamp (green), and bonded to a carrier wafer by HSQ resist (blue). (e) The membrane is back-etched to remove damaged material. (f) Microscope images of patterned overgrown membranes (left) and a transferred and back-etched membrane on a fused silica wafer (right). The rectangle on the right indicates a trench etched prior to the transfer to create a suspended region. Figure reproduced from Ref. [53].

Diamond membranes offer a range of benefits as hosts for quantum emitters. This geometry provides greater access to the spin and optical transitions of point defects and enables larger electric, magnetic, and strain fields to be applied in their vicinity. Moreover, membranes allow greater photon collection efficiency, which is a common issue in bulk diamond experiments due to the high refractive index of diamond. Photonic device integration is also benefitted by the membrane geometry, as we will explore in Chapters 3 and 4, because nanophotonic interfaces can be generated without etching sub-wavelength structures into the diamond lattice itself.

In our group, we have developed methods to efficiently fabricate and transfer single crystal diamond membranes and to incorporate coherent color centers into these films.[53] Figure 1.10 illustrates these processes. The membrane fabrication begins with He ion bombardment and annealing, which creates a graphitized layer with uniform depth across the diamond bulk. Overgrowth through chemical vapor deposition is then used to generate a single crystal layer on top. Color centers can be incorporated during this growth step or afterwards via ion implantation. A combination of electrochemical etching and polymer-based dry stamping is used to undercut, release, and transfer individual membranes to carriers. The membranes are adhered to the substrate with hydrogen silsesquioxane (HSQ) and can be placed over etched trenches if suspended areas are desired. Finally, damaged material previously on the bottom side is etched away using plasma etching. The integration capability of this membrane platform promises next-generation quantum network nodes in which a variety of optical, electronic, and microfluidic devices can be combined into functional heterostructures.

1.2.2 Two-dimensional transition metal dichalcogenides

At the same time that research surrounding solid-state quantum control has intensified in the last decade, two-dimensional (2D) materials have likewise attracted an increasing level of scientific interest due to their unique mechanical, electronic, and optical properties. These so-called van der Waals materials feature strong in-plane bonds and weak out-of-plane bonds, allowing atomically thin layers to be separated from their bulk crystals. Of particular interest for photonics and optoelectronics are the family of transition metal dichalcogenides (TMDs),[54] which feature remarkably strong optical responses that are widely tunable by doping, strain, and external fields.[55]

The unique optical properties of monolayer TMDs arise from their 2D confinement and crystal symmetry. The most widely studied TMDs are those containing group VI elements in a molecular structure MX_2, where M = Mo or W and X = S, Se, or Te. A monolayer of these materials has an X-M-X structure in the z-direction and a honeycomb lattice with broken inversion symmetry in the x-y plane, as illustrated in Figure 1.11a. In their bulk form, TMDs are indirect bandgap semiconductors. When reduced to a monolayer, however, their bandgap becomes direct, as out-of-plane p_z orbitals that contribute to electronic states at the Γ point no longer play a role in the band structure of the monolayer.[56] Consequently, the indirect bandgap between the Γ point and a point along the Γ-K direction grows, leaving the doubly degenerate direct gap at the K and K' points to dominate.

Owing to the direct bandgap and reduced dimensionality in 2D TMDs, their optical response is governed by tightly-bound excitons (Figure 1.11a). Excitons are bound electron-hole pairs which are formed via absorption of photons. A photo-excited electron and the positively charged hole it leaves in the conduction band are attracted through the Coulomb interaction to form this hydrogen-like quasiparticle. In a 2D material, the electric field lines which mediate the electron-hole interaction pass both through the semiconducting host material and through the surrounding medium, typically a dielectric. Reduced electrostatic screening in the surrounding dielectric, combined with 2D confinement and large effective electron masses, causes exciton binding energies to be significantly larger for excitons in 2D TMDs than for those in bulk crystals.[58,59] In TMDs, these binding energies are in the range of hundreds of meV, over an order of magnitude larger than those in quasi-2D quantum

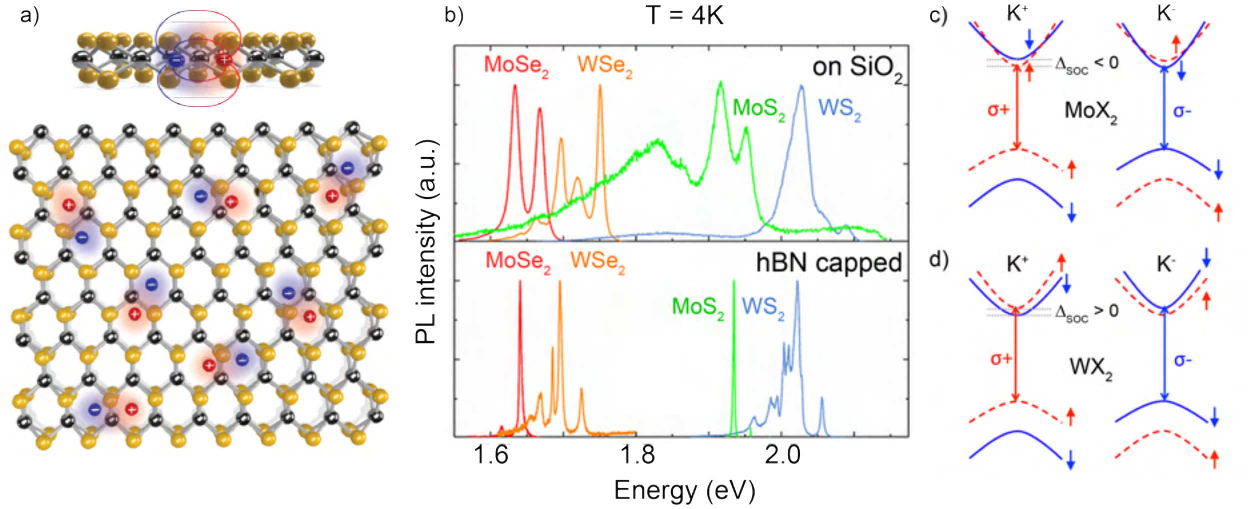

Figure 1.11 – Optical response of monolayer transition metal dichalcogenides. (a) 2D-confined excitons comprised of photo-excited electron-hole pairs in monolayer TMDs. (b) Optical spectra corresponding to exciton resonances in molybdenum- and tungsten-based TMDs on SiO$_2$ substrates and encapculated in hBN. Reproduced from Ref. [57] (c,d) Band structure of molybdenum- and tungsten-based 2D TMDs and valley-dependent optical selection rules. Reproduced from Ref. [55].

wells.[60] They correspond to exciton Bohr radii of around 1 nm and rapid radiative decay times on the order of 10-100 ps at low temperature.[55]

With these dominant exciton dynamics, monolayer TMDs exhibit highly efficient light-matter coupling. One experiment which demonstrates the out-sized effect an individual monolayer can have on incident light is the work by Scuri *et al.* from 2018.[61] These researchers created an atomically thin mirror from monolayer MoSe$_2$ with an observed reflectance of 85% at its exciton resonance. In the absence of nonradiative decay mechanisms, a TMD monolayer behaves as a perfectly reflective mirror through resonant scattering and destructive interference. With the increasing quality of monolayer TMDs, radiative linewidths can be nearly ten times larger than nonradiative linewidths, enabling this landmark result.[61]

Improvements to monolayer TMD optical quality are in large part due to encapsulation in hexagonal boron nitride (hBN), another van der Waals material that is chemically inert and electrically insulating. As shown in Figure 1.11b, encapsulation significantly reduces inhomogeneous (nonradiative) broadening.[57] In the case of MoS_2, encapsulation has been shown to reduce photoluminescence linewidths from 50 meV to 2 meV at 4K by protecting the monolayer from charge transfers, local electric fields, and substrate roughness.[57] Encapsulation is essential to nanophotonic engineering with 2D TMDs, as it allows radiative decay to dominate over nonradiative decay mechanisms.

Importantly, exciton resonances in TMDs are highly tunable via manipulation of electrostatic screening in and around monolayers. By encapsulating in a dielectric, for instance, exciton resonances redshift due to increased screening compared to ambient conditions.[62] Resonances can similarly be tuned through electrical doping of the monolayer via applied gate voltage.[63] Simply depositing an electrode in contact with a monolayer therefore enables direct control of light-matter interactions in TMDs. For example, in the work by Scuri *et al.*, the high reflectance of the $MoSe_2$ monolayer was switched on and off by modulating its free carrier density.[61] By sweeping a gate voltage between the monolayer and the backside of its substrate, researchers changed the monolayer doping from intrinsic to n-type and were able to extinguish the high reflectance of light tuned to the intrinsic exciton resonance.

Strong, tunable exciton dynamics are not the only unique optical property of monolayer TMDs. Due to their broken inversion symmetry and strong spin-orbit coupling, they also exhibit spin-valley locking at their K and K' points. The spin-orbit interaction causes spin splitting of several hundred meV in the valence band and a few to tens of meV in the conduction band, with spin states oppositely ordered in opposing valleys.[64] The ordering of these spin sub-levels differs for Mo- and W-based materials, as shown in Figure 1.11c. The level arrangement leads to valley-dependent chiral optical selection rules: righthand circularly polarized light (σ^+) is absorbed in the K valley while lefthand circularly polarized light (σ^-) is absorbed in the K' valley. As a result, excitation with one circular polarization leads to valley polarization of excitons in monolayer TMDs.[65] It has further been shown that the energetic degeneracy at these points can be lifted with an applied magnetic field.[66,67]

Investigating and manipulating intertwined spin-valley dynamics is an area of increasing interest in 2D TMD research.

Finally, due to their bond structure, monolayer TMDs are easily assembled into heterostructures and transferred to arbitrary substrates. Stacking TMDs with other van der Waals materials can improve their optical quality, as in the case of encapsulation with hBN, or add new functionalities.[68] For instance, heterostructures of two distinct monolayers (ex. $MoSe_2$ and WSe_2) can support interlayer excitons in which the hole and electron reside in separate layers. Additionally, the twist angle of the individual layers in these heterostructures can be tuned to modulate their electronic bandstructure and transport properties.[69,70]

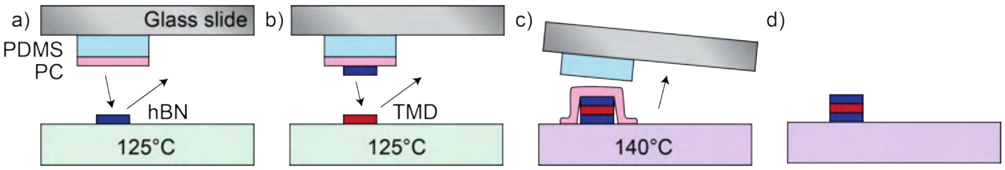

Figure 1.12 – Assembly of van der Waals heterostructures. (a) A computer-aided positioner aligns a polymer stamp (polycarbonate (PC) film on polydimethylsiloxane (PDMS)) to an exfoliated flake. When heated, the PC layer adheres to the 2D material and lifts it off the substrate as the stamp is retracted. (b) This alignment and pickup process is repeated with additional layers. (c) The full stack of 2D materials and PC film can be disengaged onto an arbitrary substrate with additional heating. (d) The PC film is dissolved in chloroform, leaving the heterostructure behind.

A variety of techniques exist to assemble heterostructures from 2D TMDs. Often, dry stamping with heated polymers is used to pick up individual exfoliated flakes and stack them together.[71] In our work, we use such a method, as shown in Figure 1.12. A polycarbonate (PC) film is placed on a polydimethylsiloxane (PDMS) stamp, which adheres to an exfoliated sample when heated. After individual layers are aligned and stacked, the PC film can be disengaged from the PDMS stamp and then dissolved in chloroform. With this technique, we can assemble heterostructures from 2D TMDs, hBN, and graphene that are tens of microns in lateral dimension.[72] Generating wafer-scale monolayers and heterostructures remains an outstanding challenge in this field, though recent advances in TMD monolayer growth[73] and new large-area exfoliation techniques[74,75] could significantly expand the technological applications of 2D TMDs.

Due to their excellent integration capability and efficient light-matter coupling, 2D TMDs offer a rich platform for nanophotonic engineering.[9,76–78] In the simplest geometries, planar interfaces have been used to manipulate exciton radiative lifetimes by an order of magnitude through destructive and constructive interference.[79–81] In the weak coupling regime, 2D TMDs have been integrated with a range of nanophotonic and plasmonic structures, including photonic crystals[82], waveguides[83,84], nanoantennas[78,85], and microdisks[86,87] to enhance and direct their photoluminescence emission. Meanwhile, strong coupling between excitons and optical cavities has opened up new research into the properties of exciton-polaritons, hybrid light-matter states formed via coherent energy swapping between the two resonances.[77] Further developments in nanophotonics fabrication techniques will help unlock the potential of 2D TMDs for optoelectronics applications.

Chapter 2

Experimental Techniques

ABSTRACT

The optical properties of solid state systems can be probed by a wide range of spectroscopic techniques, including photoluminescence, reflection, and resonance scanning spectroscopy. These measurements enable investigations both of engineered nanophotonic environments and of their influence on the optical emission from nearby materials. For quantum and low-dimensional systems, high degrees of spatial resolution, contrast, and light collection efficiency are generally required to collect meaningful optical data. Confocal microscopy satisfies these conditions while providing a flexible platform for a variety of measurement protocols. In this section, we will introduce the core principles of scanning confocal microscopy. We will then describe the confocal apparatus used for the majority of optical experiments described in later chapters.

2.1 Principles of confocal microscopy

Confocal microscopy relies on spatial filtering to restrict light collection to a small region of a sample. In most set-ups, laser light is focused onto the sample surface by an objective lens and emitted light is collected through the same lens. Before arriving at a detector, the collected light is focused onto a pinhole which shares the same focal plane as the sample surface, hence the name “confocal” microscope. Eliminating out-of-focus light from the detection pathway enables high-contrast, high-resolution imaging. The role of the spatial filter can be fulfilled by either a pinhole aperture or a single-mode fiber, provided that either aperture is positioned at an image plane which is conjugate to the sample surface.

With both excitation and collection restricted to a small region of a particular focal plane, selectivity and spatial resolution are enhanced relative to widefield microscopy, in which a large area of the sample is flooded with light that then passes directly to a detector. Generally, the maximum lateral spatial resolution for confocal microscopy is $0.61\lambda/\text{NA}$, which corresponds to the Abbe diffraction limit[1]. While there are techniques using near-field optics or nonclassical photon statistics to exceed this resolution limit,[1,88] we will not discuss them here. In order to reach this high resolution, only a small area of the sample is probed at a time. Therefore, to construct a complete two-dimensional image of a sample, either the sample or the illumination source must be scanned in the focal plane. Enhanced spatial resolution therefore comes at the cost of increased experiment time.

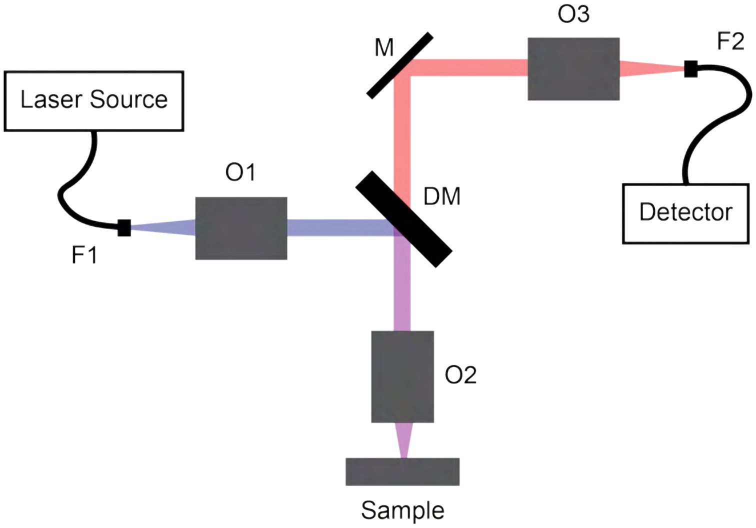

Figure 2.1 – A basic confocal microscopy set-up. A laser source is out-coupled from a single mode fiber (F1) by an objective (O1), reflected by a dichroic mirror (DM) and focused (O2) onto a sample. Red-shifted signal is transmitted through the dichroic and coupled (O3) into another single mode fiber (F2), which is then coupled to a detector.

The confocal principle can be applied to a wide range of microscopy techniques, both linear and nonlinear as well as pulsed and continuous wave. To discriminate excitation light from signal, wavelength and/or polarization filters are often required, depending on application. Dichroic mirrors and polarizing beam splitters can be used for these purposes.

In the generic confocal set-up shown in Figure 2.1, a dichroic mirror (DM) separates red-shifted photoluminescence (PL) signal from the excitation path. For this experiment, a laser source is sent through a single-mode fiber (F1) and is then collimated by an infinity-corrected objective (O1). The collimated beam reflects off the dichroic mirror (DM) and is directed to the back aperture of another objective (O2), which focuses the beam onto the sample surface. After interacting with the sample, the incident light is reflected and scattered, generally at both the excitation wavelength(s) as well as at shifted wavelengths. A portion of this light is collected by the illumination objective (O2) and re-collimated. The red-shifted PL signal passes through the dichroic mirror (DM) and is directed to the detection optics. Here, the beam passes through the inverse of the excitation pathway; an objective (O3) focuses the light onto the aperture of a single-mode fiber (F2), which is connected to a detector (D). Only the light which emanated from the focus of the illuminating objective (O2) is accepted by the single mode fiber.

To achieve the maximum possible spatial resolution and collection efficiency in a home-built confocal microscope, it is important to consider the widths of the objective apertures and beams as well as the numerical aperture of each component. In particular, to ensure the focus spot size on the sample is as small as possible, the back aperture of the illuminating objective should be completely filled if not slightly over-filled. Matching the beam diameter to the aperture size ensures the full numerical aperture of the objective is used for focusing. This condition is summarized in the following equation:

$$D = 2f \tan(\arcsin(\mathrm{NA})) \tag{2.1}$$

where NA is the numerical aperture of the illuminating objective, f is its effective focal length, and D is the beam diameter which fills its back aperture.

With a few additional optics, the apparatus depicted in Figure 2.1 can be modified to enable the excitation laser to scan across the sample surface. The confocal microscope shown

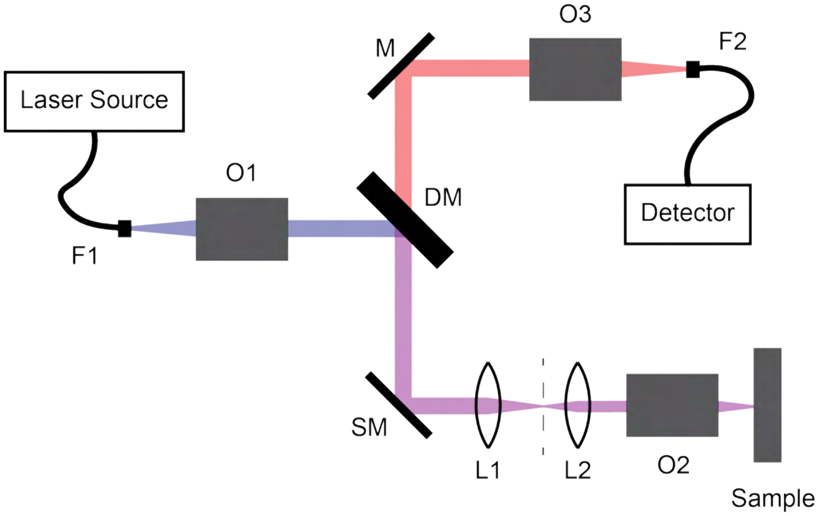

Figure 2.2 – A basic scanning confocal miroscope. A scanning mirror (SM) and lens pair (L1, L2) are used to adjust the position of the excitation laser relative to the sample.

in Figure 2.2 features a voltage-controlled scanning mirror (SM) and two lenses (L1, L2) in front of the illuminating objective. The two lenses are positioned such that their focal planes coincide and the distance from the second lens to the objective is equal to that lens's focal length. In this arrangement, adjustments to the angle of the scanning mirror shift the position of the beam focus on the sample surface. Figure 2.3 illustrates this function in more detail. In this schematic, the illuminating objective is depicted as a single lens for simplicity. Note that the focal lengths of L1 and L2 do not need to be identical. These lenses can therefore simultaneously act as a telescope to adjust beam diameter for objective aperture filling.

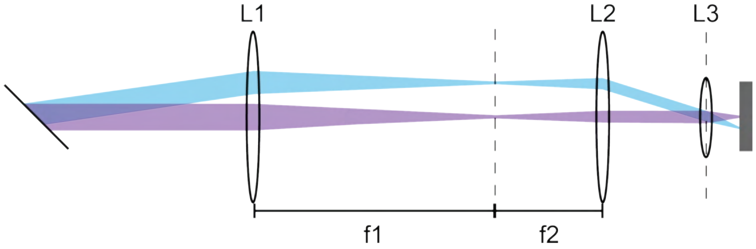

Figure 2.3 – Confocal microscopy scanning principle. As the steering mirror angle is rotated (purple beam versus cyan beam), the lens pair (L1, L2) plus objective lens (L3) move the lateral position of the beam on the sample.

2.2 Experimental apparatus

At its core, our experimental apparatus functions in the same way as the generic set-up displayed in Figure 2.2. Single mode fibers function as spatial filters for confocal imaging while a pair of large lenses are used to scan focal regions across a sample surface. The apparatus was designed to enable a wide range of optical measurements, both at room temperature and in a 4K cryostat. In this section we will walk through the elements of the set-up and the design choices made during its construction.

The schematic in Figure 2.4 shows all of the major elements of the optical apparatus, neglecting additional steering mirrors for simplicity. Asterisks indicate optical components which are mounted on either magnetic mounts or flip stands and can therefore be easily removed from the beam path during an experiment. With this capability, the apparatus can be reconfigured to probe a wide range of material systems, including nanophotonic structures, color centers, and 2D semiconductors.

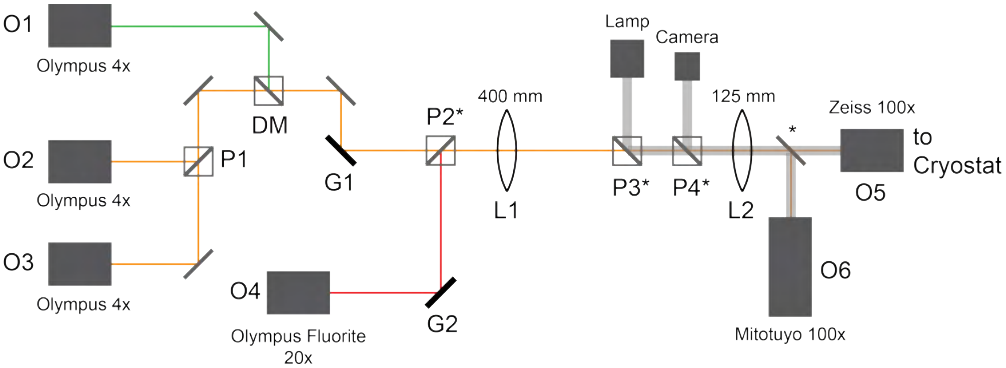

Figure 2.4 – Full benchtop experimental apparatus. Four fiber-objective beam launchers (O1-O4) create multiple collection and excitation pathways. Two galvanometers (G1, G2) function as scanning mirrors to control beam position. Pellicle beam splitters are used to combine or add additional beam paths (P1, P2) and to enable sample viewing (P3, P4). A removable mirror controls whether the beams are directed to the cryostat or room-temperature sample mount. All optics with an asterix are on magnetic or flip mounts for reconfigurability.

As shown on the right-hand side of Figure 2.4, a removable mirror controls which of two illuminating objectives is used for a given experiment. One objective is connected to a 4K cryostat while the other is used for room temperature measurements. Generally, the room temperature sample mount is used for rapid characterization of nanophotonic structures via transmission or reflection spectroscopy. The 4K set-up meanwhile is used for photoluminescence, resonance scanning, and reflectivity measurements on quantum defects and two-dimensional materials.

For virtually all of these experiments, it is necessary to locate regions of interest on a given sample. The lamp and camera located between the two large lenses (L1, L2) can be added to the beam path with pellicle beam splitters (P3, P4) attached to flip mounts. When both pellicles are inserted, the region of interest can be located by adjusting the sample mount position while looking into the camera view. Inside the cryostat, a stack of piezoelectric scanner-positioners manipulates the sample position, and the room temperature mount is adjusted using a manual three-axis translation stage plus a piezo-controlled z-axis for fine focusing.

Focal regions for excitation and collection are positioned using scanning mirrors with the sample position held fixed. In our case, two separate voltage-controlled galvanometers (G1, G2) direct beams onto the two primary lenses (L1, L2). This dual scanning capability enables increased functionality. For example, an excitation laser can be fixed by one galvanometer while the collection focus is scanned across the sample with the other. This feature is critical for the polarization-resolved experiments described in Chapter 4.2. Likewise, for transmission spectroscopy of nanophotonic structures, the multi-port set-up enables physical separation between static collection and excitation spots on the sample surface, as described in Chapter 3 and Chapter 4.1.

Each galvanometer steers collimated beams that originate from single-mode fibers coupled to objectives (O1, O2, O3, O4). These objective-fiber pairings can be reconfigured at any time by changing the patch fibers to which they connect. Typically, objective O1 is used for photoluminescence excitation with a green diode laser and O4 is used for broadband excitation with a supercontinuum source. Objectives O2 and O3 are generally connected to detectors, either avalanche photodiodes (APDs) or a spectrometer connected to a charge-coupled device (CCD) camera.

The particular objectives at each of the four fiber-launching ports were chosen with the aim of optimizing light collection efficiency by matching beam diameters to the back apertures of the illuminating objectives. The Zeiss 100x objective used for cold temperature measurements has an NA of 0.75 and effective working distance f = 1.65 mm, corresponding to a back aperture diameter of 3.74 mm, using Eqn. 2.1. To match this diameter, given the beam reduction of 3.2 arising from the two lenses (L1, L2), the collimated beam diameters should be approximately 11.8 mm. We chose Olympus 4x objectives with effective focal lengths f = 45 mm for O1-O3. Given that each fiber has an NA = 0.12, these objectives yield beams with diameters 10.88 mm, close to the desired width.

A different beam diameter is required to match the back aperture the illuminating objective used for room temperature measurements. The Olympus 100x used for these experiments has an NA = 0.9 and f = 1.8 mm, which implies a back aperture of 4.08 mm. However, the nanophotonic structures characterized with this set-up include grating couplers which accept light at a much smaller angle than that implied by the full objective NA, often in as narrow a region as 10-15 degrees. This narrow coupling implies an optimal beam diameter of 0.63 – 0.93 mm at the back aperture of the objective, which corresponds to a 2.02 – 2.98 mm collimated beam. We therefore chose an Olympus 20x objective with f = 9 mm for O4, yielding a beam diameter of 2.16 mm.

To clarify how the multi-port confocal apparatus is reconfigured for different experiments, we show two examples of experiments for which is it commonly used. The first instance, shown in Figure 2.5, enables PL mapping of quantum defects and excitons in TMDs. A green diode laser reflects off a dichroic mirror (DM) and is steered by a galvanometer onto a sample inside the cryostat. Red-shifted light is collected via the same beam path, passes through

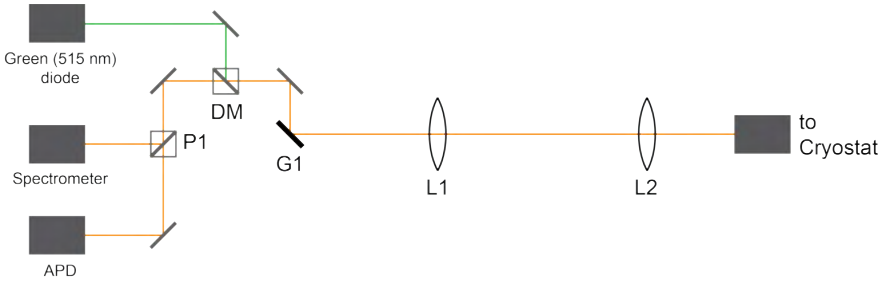

Figure 2.5 – Experimental apparatus configured for photoluminesence spectroscopy.

the dichroic mirror, and is directed to both a spectrometer and APD with a pellicle beam splitter (P1). In another instance, shown in Figure 2.6, collection and excitation pathways are steered separately by the two galvanometers to enable transmission spectroscopy of optical resonators. A broadband supercontinuum source is coupled into a nanophotonic structure in one position while the detection optics are focused on a separate region by the other galvanometer. Using a visible laser that is collinear with the detection pathway enables the collection region to be positioned precisely on the sample surface. These illustrations give a sense of how the apparatus is used and context for the design choices that were made, though there are a range of other configurations and optical measurements that are also enabled by this set-up.

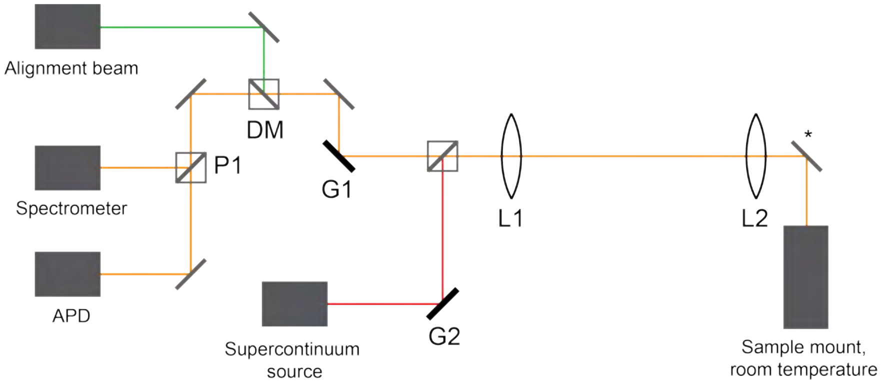

Figure 2.6 – Experimental apparatus configured for transmission spectroscopy of nanophotonic devices.

Chapter 3

Nanophotonic Device Fabrication with Templated Atomic Layer Deposition[†]

ABSTRACT

As discussed in Chapter 1, quantum and low-dimensional materials offer unique opportunities for nanophotonic engineering. However, these systems can be challenging to integrate into nanoscale devices while maintaining their desired properties. In the case of diamond color centers, etching subwavelength features into the diamond lattice introduces strain and poorly controlled surface states which degrade the spin and optical coherence of quantum emitters. 2D materials, meanwhile, are easily degraded by etching processes and are highly sensitive to strain. With these target systems in mind, we developed a novel approach to interfacing nanophotonic devices with optical materials of interest based on templated atomic layer deposition (ALD) of TiO_2. This process can build low-loss, high quality factor resonators on arbitrary substrates without exposing them to etching, enabling efficient optical interfaces with quantum materials. In this chapter, we provide an overview of the process and explain in detail its most critical elements, the electron beam lithography and TiO_2 deposition. We then demonstrate high quality factor ring resonators and photonic crystal cavities fabricated with this approach.

3.1 Process overview

We begin our fabrication process (illustrated in Figure 3.1 a-c) by patterning device templates into poly(methyl methacrylate) (PMMA) via electron beam lithography. In some

---

[†]. Portions of the work in this chapter were reported in Ref. [89]

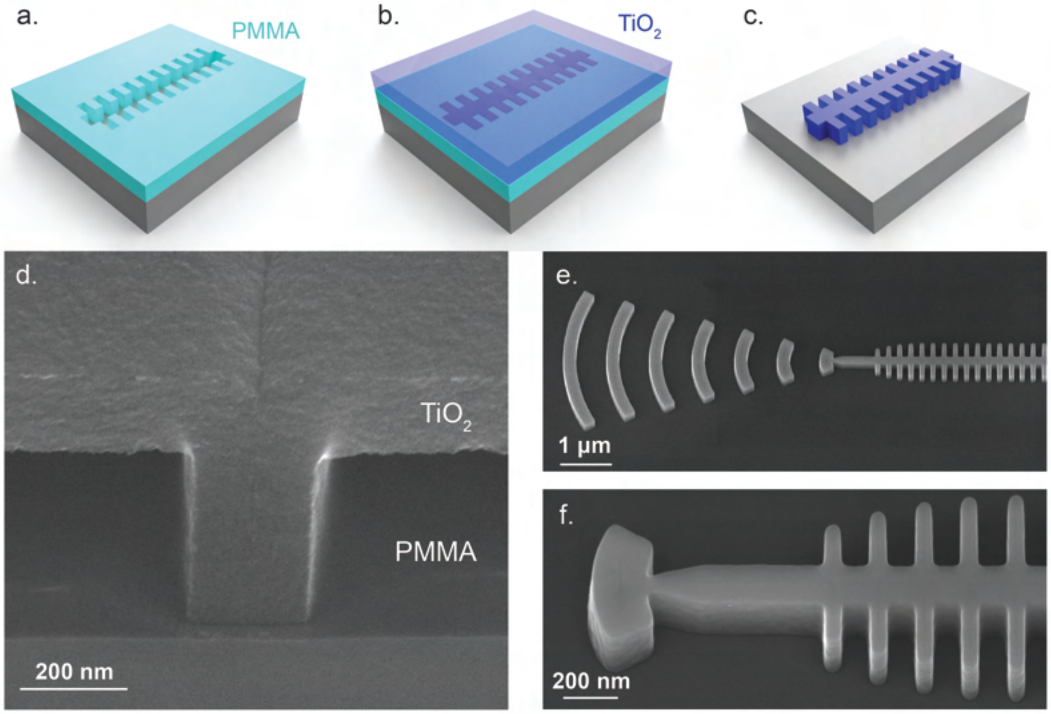

Figure 3.1 – Nanofabrication process. (a) Nanophotonic device templates are patterned into e-beam resist and then (b) conformally filled with ALD TiO$_2$. (c) Overfilled TiO$_2$ is etched back and resist template is stripped. (d) 45 degree cross-sectional scanning electron microscope (SEM) image of a resist trench over-filled with TiO$_2$. (e, f) 30 degree SEM images of completed nanophotonic structures.

applications, we follow lithogrpahy with a brief, three second oxygen plasma exposure to remove residual polymer adsorbates at the bottom of the templates. In contrast to prolonged plasma etching, this step does not damage the underlying substrate and simply ensures the template is clean and ready to be filled.

Next, we use ALD to conformally fill the resist templates with high-index TiO_2. To avoid re-flowing the resist, the deposition occurs at 90 C, which is below the glass transition temperature of most resists ($\approx$ 105 C for PMMA). A low chamber temperature also ensures that the TiO_2 remains amorphous rather than rutile or anatase. These other phases of TiO_2 develop during ALD at higher deposition temperatures and form grain boundaries, which can lead to scattering loss.[90] We significantly over-fill the device templates to help planarize the top TiO_2 surface, where a slight crease forms (Figure 3.1d) due to the conformal filling profile.

After deposition, we etch away the excess TiO_2 with inductively coupled plasma reactive ion etching (ICP RIE) to expose the resist underneath. Importantly, because we do not etch through the resist template during this step, neither the substrate nor the device sidewalls are etched by the ICP. After removing the TiO_2 overfill, we chemically strip the remaining resist and any etch residues with Nanostrip (MicroChem) to reveal the templated devices (Figure 3.1 e-f). Lastly, we anneal the TiO_2 structures on a hot plate at 250 C for at least two hours, which we found was critical for reducing material optical loss.

3.1.1 Electron beam lithography of device templates

The e-beam lithography step is perhaps the most critical element of this nanofabrication process, as the final TiO_2 devices are virtually perfect negative images of the PMMA template. The ideal device template should be fully exposed and developed down to the substrate, have smooth, vertical sidewalls, and re-create as precisely as possible the critical dimensions of the device. With resonant photonic devices, these critical dimensions can be as small as several nanometers, particularly for photonic crystal cavities which rely on subtle tapering of sub-wavelength features to achieve high quality factors. An additional, critical consideration is that e-beam lithography on electrically insulating substrates often leads to charging effects in which accumulated electrons in the resist and substrate deflect the incident electron beam. Figure 3.2a illustrates this effect. The result is a distored pattern, with some areas over- or under-exposed based on the deflection of the beam away from its intended position during the write.

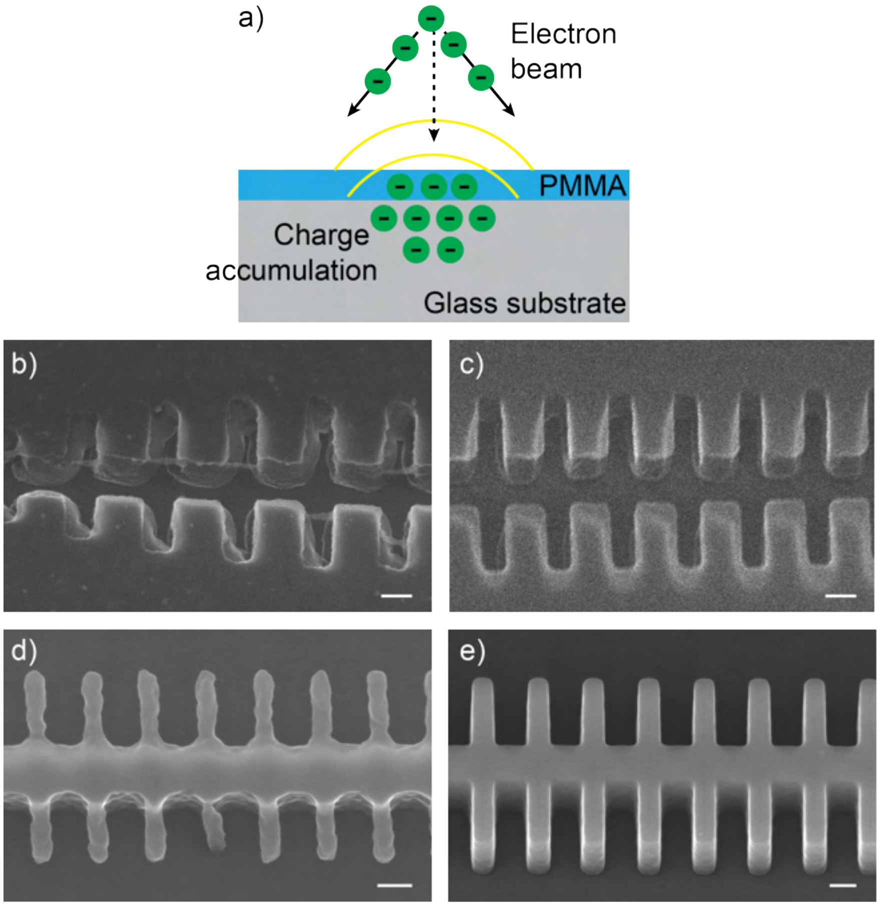

Figure 3.2 – (a) Illustration of charging effects during e-beam lithography. Negative charge accumulation in the substrate and resist can deflect the incident electron beam. (b) SEM image of a PMMA device template that was distorted due to charging effects. (c) SEM image of a pristine PMMA template. (d) Final TiO_2 structure produced by a template similar to (b). (e) Final TiO_2 device produced by a pristine template similar to (c).

A common solution to charging issues during e-beam lithography is the deposition of an electrically conductive layer, either on top of or directly underneath the resist. In our case, we deposit 20 nm of gold as a conduction layer on top of the PMMA before lithography. However, even with this relatively thick conduction layer, we still observed the results of charging effects on fused silica, our substrate of choice for device testing due to its low index of refraction. Figure 3.2b displays distorted device templates that were produced despite the presence of a conduction layer. When the full fabrication process is carried out using a template that suffered from charging-induced distortion, the result is a structure which appears flakey on the edges, with some pieces of TiO_2 hanging off the main device structure and others missing entirely, as pictured in Figure 3.2d. This pathology is due to the template being under-exposed in areas that jut out from the central waveguide. Because the TiO_2 is deposited on top of an area that is not fully exposed, it can be torn off during the wet etch removal of the PMMA device template, leaving ragged structures behind.

Fortunately, additional strategies to mitigate charging effects can eliminate these issues. First, electron beams with lower currents are less susceptible to charging effects. Typically, beam currents are chosen based on beam diameter and exposure time, with larger beam currents corresponding to wider beam diameters and therefore reduced resolution but shorter exposure times. Below a certain beam current ($\approx$ 10 nA on our tool), the beam diameter is not reduced any further, and smaller beam currents are not commonly used. In our case, however, we use a 0.3 nA beam current to pattern device templates on glass for the purpose of reducing substrate charging. Second, the path traversed by the electron beam during the exposure, or the writing order, can be modified in order to avoid the beam dwelling in one location long enough to build up negative charge. We generally select a write order in which the beam jumps around inside the writing field rather than one which follows the pattern geometry, as shown in Figure 3.3. Third, multipass exposure, in which one pattern is exposed multiple times in a row with a lower dose, can also reduce the duration of time the electron beam dwells in a given location. In our case, we expose four times at a quarter of the total exposure dose. This method also improves line edge roughness by averaging out electron beam position noise,[91] which benefits our nanophotonic devices. Each of these three techniques has the drawback of increasing writing time, as there is a fundamental tradeoff between reducing charging effects and minimizing exposure times. However, put together, they yield pristine device templates which generate high quality TiO_2 devices, as shown in Figure 3.2d,e.

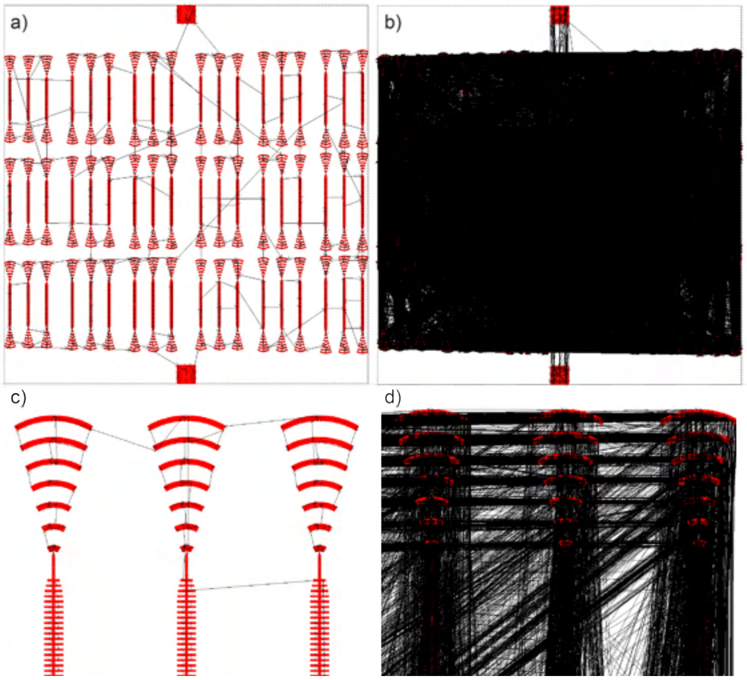

Figure 3.3 – Electron beam writing order. (a, c) Beam path that follows the feature geometry. (b, d) Disordered beam path used to mitigate charging effects.

After e-beam exposure, we remove the gold conduction layer with TFA gold etchant (KI_2 in iodine solution) and then carry out a short post-exposure bake (60 s at 115C). Baking resist after exposure is more common in photolithography as a way to eliminate standing waves formed by back-reflected UV beams in micron-thick photoresist.[92] With e-beam lithography, there is some evidence it can help generate smoother sidewalls,[93] and we found this step improved our device performance somewhat. The final aspect of the lithography step is the resist development. During development of a positive resist, short polymer chains generated by scission due to electron beam exposure are selectively dissolved away, leaving the un-exposed areas behind. For our PMMA process, we use a 1:3 MIBK:IPA mixture as developer and an IPA rinse as the development stopper. To help achieve smooth sidewalls, we develop on a cold plate set to 7 C.[94] In principle, the cold temperature improves development because shorter polymer chains have lower transition glass temperatures than longer chains do. Therefore, at lower temperatures, there is a greater selectivity between short and long chains.

3.1.2 TiO_2 deposition and characterization

Besides the lithography of the device templates, the TiO_2 growth step is the next most critical process in this nanofabrication procedure. To ensure the deposited material was high quality, we characterized amorphous TiO_2 films grown with our ALD recipe using a combination of ellipsometry, atomic force microscopy (AFM), and X-ray photoelectron spectroscopy (XPS). These methods provide information on the refractive index, surface roughness, and elemental content of the films, respectively. For our nanophotonics applications, the ideal film would be uniform and stoichiometric, with a high index and smooth surfaces.

Our ellipsometry data (Figure 3.4a) confirms the deposited TiO_2 has a high index over a broad wavelength range ($n > 2.3$ out to 1550 nm) and a bandgap of approximately 3.3 eV. We fit a Tauc-Lorentz curve to this data and used this model to gauge film thickness following deposition and etching processes. The refractive index we measured is consistent with previous work[95,96] and is high enough to maintain waveguiding on a variety of lower-index substrates.

With AFM (Figure 3.4c,d), we measured the surface roughness of ALD-grown TiO_2 films and the fused silica substrates used to characterize nanophotonic device performance. These roughness values indicate the bottom and top surfaces of our optical resonators are smooth; each surface exhibits a root mean square (RMS) roughness of less than one nanometer over

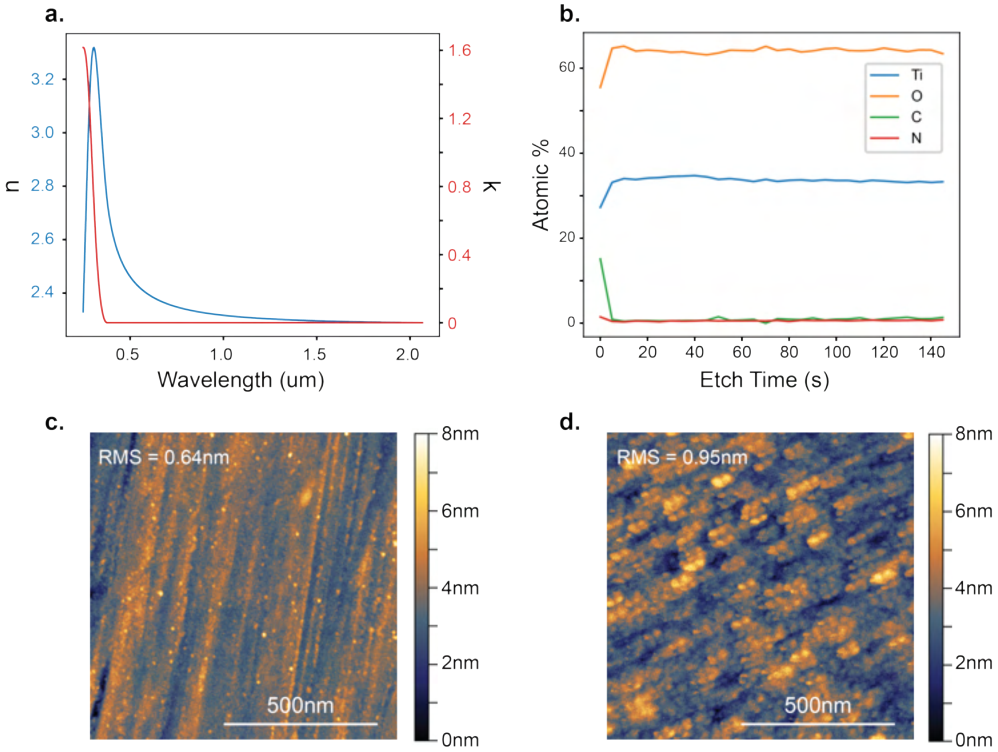

Figure 3.4 – TiO_2 film characterization. a) Real and imaginary refractive index for as-deposited TiO_2, measured on a 250 nm-thick film. b) XPS data for as-deposited TiO_2 indicating atomic percentage of various elements versus sputtering etch time, a proxy for film depth. The titanium line represents the sum of all oxidation states. c) AFM scan of a 1 µm x 1 µm region on a fused silica substrate used for the initial photonics characterization experiments. d) AFM scan of a 1 µm x 1 µm region of an approximately 700 nm thick TiO_2 film after annealing.

a 1 µm by 1 µm square area. The bottom surface is characterized by polishing marks, while the top surface shows a tight granular structure which is also visible in SEM images (see Figure 3.1). We expect the top surface of the TiO_2 nanostructures is similar to that of the thin films, as the TiO_2 etching process does not introduce additional roughness. Also, because AFM scans of the high-aspect ratio ($\approx$ 1:3) nanostructures often include significant scanning artifacts, the thin film AFM scans are our most reliable indicator of top surface roughness. It is particularly important that the top and bottom surfaces of our 1D photonic crystal cavities are smooth because the cavity modes are largely concentrated in these areas (see Figure 3.7).

We used XPS to determine if carbon and/or nitrogen impurities were present in our TiO_2 films from un-oxidized tetrakis(dimethylamido) titanium (TDMAT) precursor ligands. Initially, we found significant levels of both carbon and nitrogen in our films, up to 12% and 7%, respectively. Although we do not have optical loss data that proves that these additional ligand elements negatively impact device performance, their presence likely indicates the presence of dangling bonds in the amorphous films, which can generate optical loss. We concluded that the residence time of the precursor gasses in the deposition chamber was likely too low for the TDMAT oxidation reaction to occur fully, at least at the relatively low temperature of our deposition process (90 C).

To ensure the oxidation reaction was complete, we modified the sequence in which the ALD chamber valves were actuated in order to drive up the pressure and residence time of the oxidizing precursor, which in our case is water. The sequence is as follows: the TDMAT precursor is pulsed and then purged, then the ALD chamber stop valve is closed. Only then is the water precursor pulsed into the chamber and allowed to build pressure. After a few seconds, the chamber stop valve is re-opened and the water precursor is purged. With this static oxidation process, we were able to virtually eliminate residual TDMAT ligand elements in our films according to XPS data. Figure 3.4b shows that our films contain atomic percentages of carbon and nitrogen that are below the fitting error threshold of the XPS analysis software used. Beyond a surface level of adsorbed carbon, the film appears uniform as a function of depth when all titanium oxidation states are summed together.

Curiously, we found that annealing was necessary to observe optical resonances in our high-Q devices. The annealing temperature, 250 C, was chosen to be low enough to avoid grain formation in the TiO_2,[97] and ambient hot plate conditions were taken for convenience. We suspect that the increase in device performance from annealing is due to the satisfaction of oxygen vacancies within the waveguiding TiO_2. Oxygen vacancies can make amorphous TiO_2 films “leaky” in optoelectronic applications[98] and could be a source of optical absorption loss in our cavity devices. Annealing may also lead to densification of the amorphous material and removal of excess precursor ligands. We have some evidence of these effects based on XPS data from films that were grown before we began using the static oxidation method. These films showed reductions in carbon and nitrogen content (from 12.1% to 3.3% and from 6.6% to 1.6%, respectively) after a 2 hr anneal at 250 C. That said, for films grown using our static oxidation recipe, both the annealed and un-annealed TiO_2 films show similar XPS profiles as pictured in Figure 3.4b, so changes in carbon and nitrogen content from annealing are not detectable with the resolution of our XPS measurements.

3.2 Nanophotonic devices on fused silica

To demonstrate the performance of this platform for nanophotonic device fabrication, we designed and built high quality factor optical resonators on fused silica substrates. High-Q resonators are sensitive to loss from material optical absorption and scattering, particularly at short wavelengths. Therefore, our measurements of device performance offer compelling examples of the capability of this nanofabrication approach for low loss photonics.

3.2.1 Grating couplers

The resonator devices we fabricated to test our platform all function via on-chip waveguiding. To efficiently couple far-field beams from our confocal microscopy set-up into and out of waveguide modes, we designed and fabricated integrated grating couplers. These devices function through the second-order Bragg condition, as light scattered from individual grating elements constructively interferes in the direction of the waveguide mode propagation and couples into the device. In the reverse direction, the waveguide mode scatters off the grating and constructively interferes at an out-of-plane angle near normal.

Using a ray optics picture, we can determine the grating period which will efficiently scatter light from a waveguide mode to a particular out-of-plane angle. For constructive interference, the path length difference between a ray which is scattered off one grating element should be such that the phase difference between that ray and the one scattered off the next grating element is a multiple of 2 π:

$$\frac{2\pi}{\lambda} n_{\text{eff}} a - \frac{2\pi}{\lambda} n_1 b = 2\pi m \tag{3.1}$$

Here, n_{eff} is the effective index of refraction at the location of the grating element, a is the grating period, n_1 is the refractive index of the surrounding medium, and b is the path length of the first ray, labelled in Figure 3.5b. Using this geometrical picture, we can re-write this equation to include θ, the scattering angle:

$$n_{\text{eff}} a - n_1 a \sin(\theta) = m\lambda \tag{3.2}$$

This relationship provides a sense of what grating period is appropriate to achieve phase matching, and therefore efficient coupling, into and out of a wavegiude mode at a particular wavelength. However, optimizing grating transmission generally requires numerical simulation, and we relied on parameter sweeps in FDTD simulations to enhance our grating

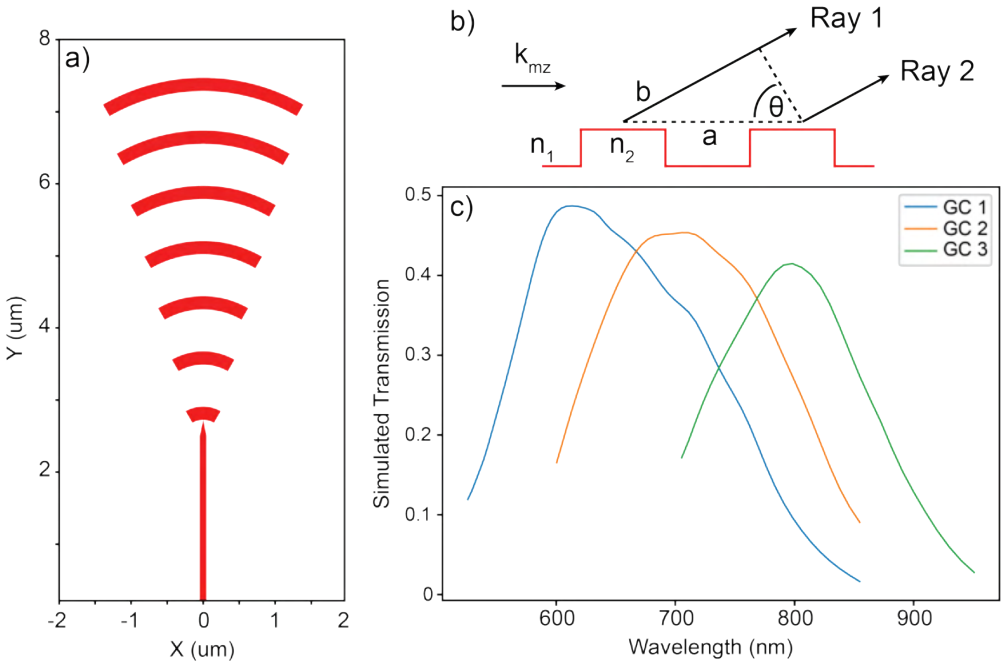

Figure 3.5 – Grating coupler design and simulation. a) Device pattern used for e-beam lithography of grating couplers featuring a tapered waveguide and 60 degree sections of circular fins. b) Simulated out-coupling transmission spectra for structures with geometry pictured in a) on fused silica (n = 1.4) substrates. The three curves correspond to gratings with different circular fin pitch, which sets the peak wavelength (GC 1 pitch 345 nm, GC 2 pitch 407 nm, GC 3 pitch 494 nm). Data have been cropped to indicate the approximate regions for which each structure has been designed to provide high in- and out-coupling.

performance beyond this starting point.

Pictured in Figure 3.5a, our design features a tapered waveguide leading to a curved grating of seven fins. Each fin is a sixty-degree cut of a circle, with increasing radii moving outward from the waveguide. We used Lumerical FDTD software to simulate how much of a waveguide mode source is deflected upwards by this structure and optimized this value depending on the grating's geometrical parameters. For these simulations, we placed the devices on an n = 1.4 substrate to approximate the fused silica on which we eventually fabricated them. The height of the structures was 250 nm, which matches the height of the resonators that we targeted.

We designed three grating couplers that were optimized for different wavelength ranges. Each included the same general geometry but with different pitches of the circular fins. Figure 3.5b shows the transmission spectra of devices with pitches of 345 nm, 407 nm, and 494 nm, which are respectively labelled GC1, GC2, and GC3. After designing optical resonators for a particular wavelength, we selected the grating coupler design with the highest simulated transmission at that wavelength and added this structure to the overall device template for fabrication.

While we did not experimentally determine the coupling efficiency of these gratings, we note that for each of the three structures we proceeded with, simulated peak transmission was 40-50%. It should also be noted that light outcoupled from these structures does not propagate at a 90 degree angle relative to the substrate but rather at an angle 10-25 degrees from normal, depending on the particular structure simulated. Since our confocal microscopy set-up is not designed to match this angle, it is unlikely that we are coupling the maximum simulated percentages of light into and out of our structures. That said, when we couple an excitation laser into an optical resonator using these gratings, we are able to visually detect a bright out-coupling spot from the grating on the opposing side (see Figure 3.6 and Figure 3.7. Therefore, these gratings provide an efficient means of performing transmission spectroscopy of on-chip optical resonators.

3.2.2 Ring resonators

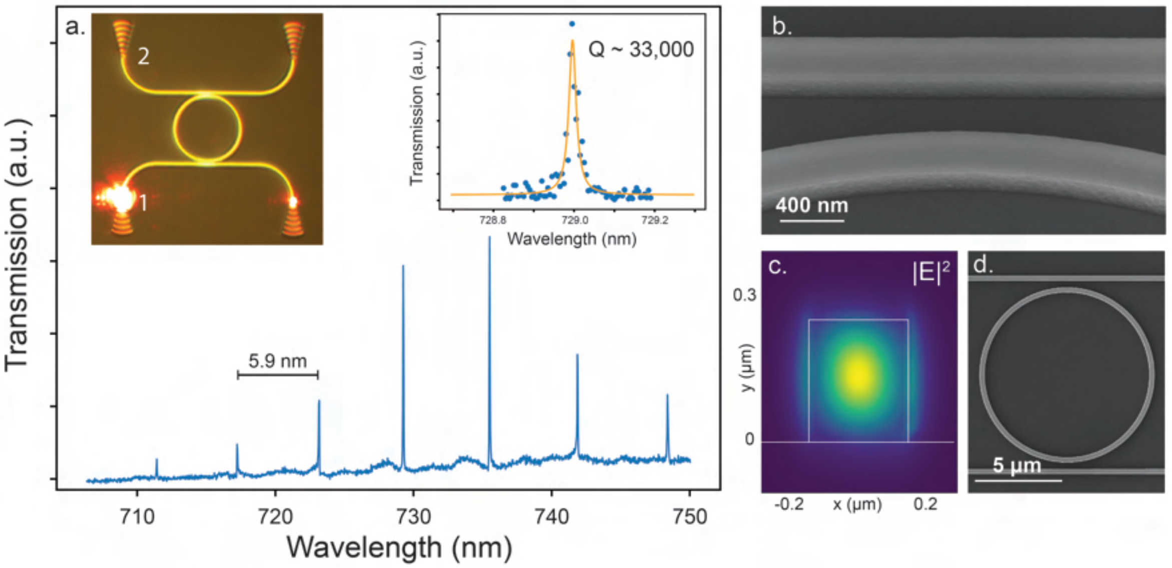

Figure 3.6 – Microring resonators on fused silica. (a) Transmission spectrum for a ring resonator with 5 μm radius. Left inset: camera view of laser in- and out-coupling. Excitation and collection ports are labelled one and two, respectively. Right inset: high-resolution resonance scan showing Q = 33,260. (b) 30 degree tilted SEM image of waveguide coupling region for device in (a). (c) Simulated cross-sectional electric field intensity of the TE resonator mode. (d) Top-down SEM image of ring resonator in (a), (b).

To demonstrate the performance of this fabrication platform, we first built high-Q microring resonators on fused silica substrates. Ring resonators can function as spectral filters in integrated photonic networks[99] and are attractive for applications in sensing[10] and chiral quantum optics.[100] We fabricated resonators in an add-drop geometry, where two linear bus waveguides couple to either side of a 5um-radius circular loop (Fig. 2a and d). The waveguides were 300 nm wide and 250 nm tall, with coupling distances of 375 nm between the buses and resonator (Figure 3.6b). At each end of the bus waveguides, we included grating couplers that can couple up to ≈ 48% of incident light into and out of the waveguides.

To probe the ring resonator spectra, we coupled a broadband excitation source into one bus waveguide and measured transmitted signal through the drop port. As depicted in the inset of Figure 3.6a, a bright outcoupling spot appears at the opposite end of the excitation waveguide, where most of the broadband source is transmitted, while a weaker spot containing only resonant frequencies is detected at the drop port. For these 5 µm -radius devices, the spectra feature standing wave resonances separated by approximately 5.9 nm. Because the resonance linewidths are too narrow to be fully resolved by our spectrometer, we scan a tunable laser across each peak and measure transmitted intensity to accurately quantify quality factors for these devices. Typical Q values were 20,000-30,000. While it is challenging to compare resonators with different radii and operating wavelengths, these values are competitive with state-of-the-art quality factors reported elsewhere.[10,101,102] This result demonstrates that our low-loss templated ALD platform can yield high performance optical resonators.

3.2.3 Photonic crystal cavities

We next designed and fabricated 1D photonic crystal cavities, which have significantly lower mode volumes than ring resonators and can consequently induce larger Purcell enhancement for a given quality factor. Our design features a 150 nm-wide and 250 nm-tall central waveguide with fins that periodically modulate the effective refractive index along its length (Figure 3.7a). The cavity region is formed at the center of the waveguide, where the pitch of the fins gradually decreases by 10%. Quality factors for these structures depend on the number of fins on either side of the central cavity region, with more fins corresponding to higher reflectivity and higher Qs. Unlike the ring resonators, in which the resonator modes are concentrated at the center of the waveguide cross-section Figure 3.6c, we design the 1D cavities to accommodate a single mode concentrated near the waveguide's top and bottom (Figure 3.7b-c). Notably, this design increases the electric field intensity near underlying

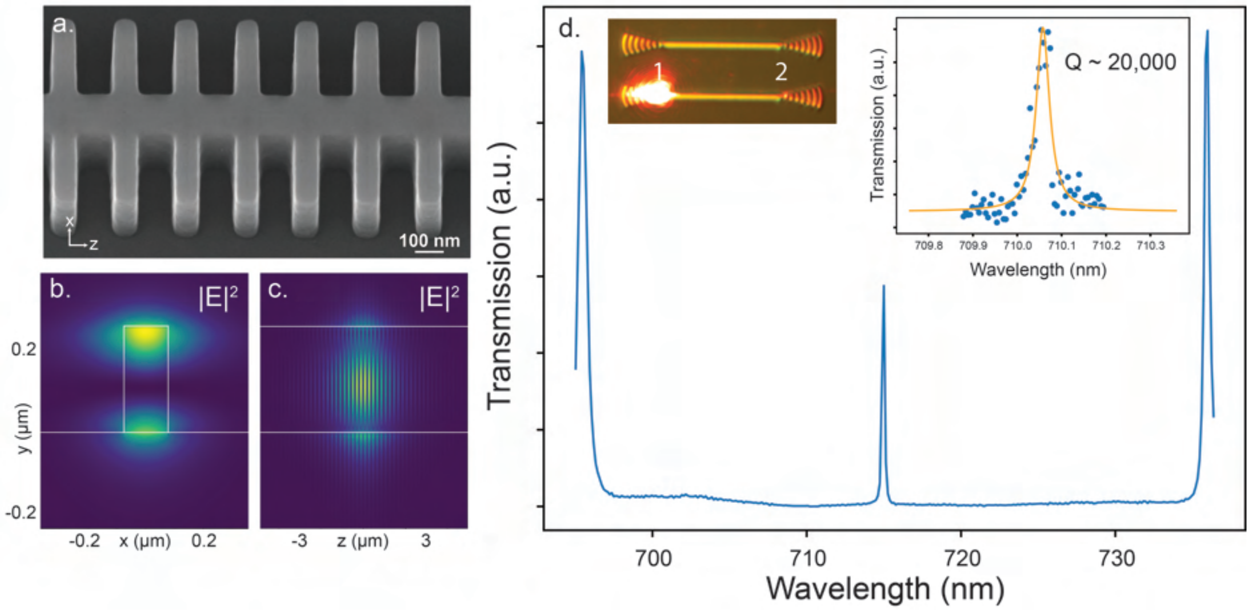

Figure 3.7 – 1D cavities on fused silica. (a) 30 degree tilted SEM image of 1D photonic crystal cavity. (b), (c) Simulated cross-sectional electric field intensity of the cavity mode across the cavity center and along the cavity length, respectively. (d) Transmission spectrum for a 1D cavity on fused silica with 20-fin reflectors. Left inset: camera view of laser in- and out-coupling. Excitation and collection ports are labelled one and two, respectively. Right inset: high-resolution resonance scan for 25-fin device in (a) showing Q = 19,640.

elements, which enhances light-matter coupling in those regions.

To validate the performance and reproducibility of these devices, we first characterized their spectra on fused silica substrates. Table 3.1 shows that cavity resonance wavelengths are highly deterministic, with standard deviations in the range of 0.5-1.4 nm. These statistics were averaged over ten devices with 25-fin reflectors at each of three wavelengths. Although it was not possible to scan our tunable laser at wavelengths lower than 700 nm, spectrometer data gives a lower bound for quality factors, which exceed 6,000 for even the shortest-wavelength resonances. By scanning over device resonances near 710 nm, we measured quality factors approaching 20,000, more than twice what is approximated by spectrometer-limited data (Fig 3d). These results, combined with SEM images, indicate that device sidewalls are sufficiently smooth for high-Q visible frequency operation.

Table 3.1 – Resonance statistics averaged over ten 25-fin 1D photonic crystal cavities at each of three wavelengths. Due to limited spectrometer resolution, the listed quality factors are interpreted as lower bounds only.

Mean λ (nm)	Std. dev. λ (nm)	Mean Q
606.499	0.623	6,040
655.804	0.561	7,210
710.341	1.326	9,070

Chapter 4

Integrating TiO_2 Photonics with Quantum Materials

ABSTRACT

The templated atomic layer deposition process described in the previous chapter is uniquely suitable for building nanophotonic interfaces with quantum materials due to its integration capability. Here, we showcase this capability with two applications. In the first, we demonstrate our platform's potential to enable spin-photon interfacing with quantum defects by fabricating high-Q resonators on a single crystal diamond membrane. With cavity modes concentrated largely within the membrane itself, we show that this platform can enable large defect-cavity cooperativities for efficient spin-photon interfacing. In the second experiment, we build an electrically controllable chiral nanophotonic interface with monolayer WSe_2 and demonstrate propagation direction-dependent interactions between waveguide modes and circularly dichroic excitons. We further show that this nanophotonic waveguide can function as a near-field source for diffusive exciton fluxes, which display valley and spin polarizations that are inherited from the interface chirality. Overall, the deterministic integration of nanophotonic devices with both diamond membranes and van der Waals heterostructures unlocks new ways to manipulate light-matter interactions.

4.1 Integration with diamond membranes[†]

4.1.1 Introduction

Diamond color centers are a promising basis for emerging quantum technologies due to their robust spin coherence, optical addressability, and on-chip integration capability.[103]

[†]. The work in this section was reported in Ref. [89]

Nanophotonic resonators are critical for building quantum networks based on these centers, as they enable deterministic interactions between individual optical photons and electronic spin states.[23] By providing a light–matter interface, integrated nanophotonic devices can mediate entanglement between separated color centers[28] while simultaneously enhancing their quantum emission rates and improving photon indistinguishability through the Purcell effect.[2] In order to capitalize on the potential of integrated photonics for quantum networking, a scalable and deterministic method of device fabrication is needed.

Current methods for integrating diamond color centers with nanophotonic resonators[11] suffer from low yield and are often incompatible with the fabrication of other on-chip devices. These approaches rely on 1) angled or quasi-isotropic etching into bulk diamond to generate suspended structures,[104–107] 2) etching devices vertically into sub-wavelength thick diamond membranes,[101,108,109] or 3) etching devices vertically into gallium phosphide-diamond heterostructures.[110–112] In the last decade, these techniques have enabled landmark demonstrations of zero-phonon line (ZPL) enhancement[101,110,113] and coherent light-matter interactions in single devices.[35] However, carving wavelength-scale features into diamond damages and strains the crystal lattice and brings poorly controlled surface states into close proximity with color centers.[114–116] These effects significantly degrade color center spin coherence compared to bulk values[113] and consequently limit operational device yield. Additionally, suspended structures generated from bulk diamond are subject to geometrical constraints which complicate their integration with on-chip single photon detectors, electronics, or other devices that could enhance quantum network functionality.

Scattering from surface roughness creates further challenges for diamond nanophotonics, particularly in the visible wavelength regime. Along with the nitrogen-vacancy center,[117] with its ZPL at 637 nm, several group-IV color centers operate in the visible, including the silicon-vacancy (ZPL 737 nm),[43,118] germanium-vacancy (ZPL 602 nm),[49,51] and tin-vacancy (ZPL 620 nm)[45] centers. For a given root-mean-square roughness σ, scattering loss is proportional to σ^2/λ^3.[119] Accordingly, to overcome this loss at short wavelengths, optical devices designed to interact with diamond color centers ought to be exceptionally smooth. Because diamond is both extremely hard and inert, it is difficult to micromachine its surfaces smoothly, and quality factors for diamond nanophotonics are often limited by surface scattering as a result.

An alternative approach is to build nanophotonic resonators on top of diamond membranes rather than out of diamond itself. This strategy avoids micromachining diamond and consequently minimizes crystal distortion and sidewall roughness in final structures. Importantly, with sufficiently thin membranes, overlying devices retain the potential to enable coherent single photon-spin interactions. Here, we used templated atomic layer deposition (ALD)[95,96,120] of TiO_2 to generate smooth, high-Q optical resonators on a diamond membrane without a substrate or sidewall etching step. With a high refractive index ($n > 2.3$) over a broad range of wavelengths and a relatively large bandgap ($\approx$ 3.3 eV),[90,95,102] TiO_2 is uniquely suited for waveguiding on diamond ($n \approx 2.4$) and for visible frequency device operation, promising efficient spin-photon interfaces with color centers.

4.1.2 Photonic crystal cavities on diamond membranes

To demonstrate the potential of our ALD TiO_2 process to interface with color centers in diamond, we fabricated 1D photonic crystal cavities on a 50 nm-thick single crystal diamond membrane (Figure 4.1a,b). The membrane was generated via ion bombardment and chemical vapor deposition overgrowth.[53,121] It was then adhered to a Si carrier chip using hydrogen silsesquioxane (HSQ),[53,122,123] which we subsequently annealed to produce a low index substrate. Our fabrication procedure for the resonators on the membrane was identical to the fused silica case described in Chapter 3, except we built devices slightly taller (300 nm instead of 250 nm) to maintain waveguiding on the higher-index ($n \approx 2.4$) diamond.

For 1D cavities on the diamond membrane, we measured quality factors reaching 4,400

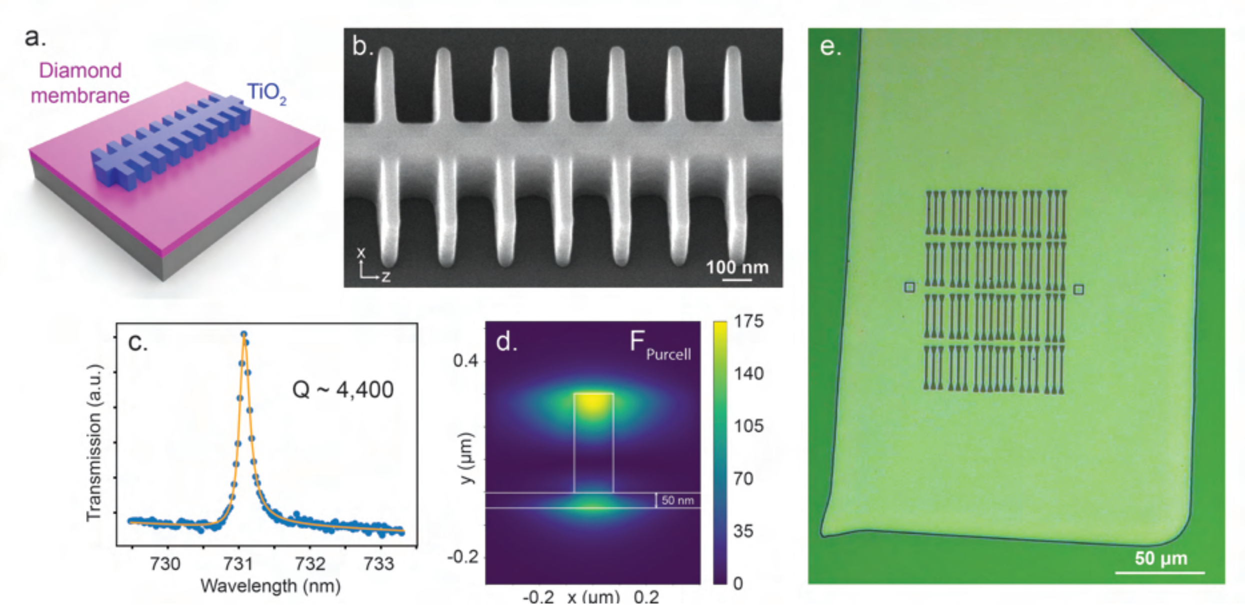

Figure 4.1 – 1D cavities on diamond membranes. (a) Schematic of a 1D photonic crystal cavity on a diamond membrane. (b) 30 degree tilted SEM image of a cavity on a 50 nm-thick diamond membrane. (c) Transmission spectrum of device pictured in (b) showing Q = 4,410. (d) Simulated maximum Purcell factor (F_{Purcell}) across the cavity center given a quality factor of 4,400. (e) Microscope image of 72 cavities fabricated on a 50 nm-thick diamond membrane with 200 µm x 300 µm lateral area.

(Figure 4.1c), with the majority of devices showing Q $\approx$ 4,000. These values are lower than those measured for similar devices on fused silica substrates (Chapter 3). One possible explanation for this difference is that the hydrogen silsesquioxane (HSQ) layer which adheres the diamond membrane to its carrier chip is optically lossy. Because the 1D cavity mode is concentrated partly within this underlying layer (see Figure 4.1d), optical loss in the HSQ would certainly be detrimental to device performance. To investigate this possibility, we fabricated cavities directly on an HSQ layer after it was processed in the same manner as in the diamond membrane experiments. A 600-700 nm layer of FOX16 HSQ (Dow Corning) was spin-coated on a silicon chip which was then annealed in an Ar gas tube furnace for 8 hours at 420 C to nominally convert the HSQ to $\approx$ 500 nm fused silica. Ideally, this annealing process removes Si-H bonds, collapses pores, and reduces stress in the HSQ layer to produce a low-index, low-loss substrate.[124] The device fabrication process then proceeded as described in Chapter 3.

After the annealing process described above, the HSQ layer appears pitted under microscope imaging, as shown in Figure 4.2a, which suggests scattering loss may be present. Nevertheless, transmission spectroscopy (Figure 4.2b,c) reveals that devices on HSQ exhibit higher quality factors than those on diamond membrane-HSQ heterostructures and similar performance to those on fused silica, at least within spectrometer resolution. There may still be avoidable optical loss in the HSQ layer, and previous work optimizing HSQ as a substrate for nanophotonics indicates that higher temperature annealing may result in less-lossy films.[124] However, we must consider potential damage to diamond membrane samples from these more extreme annealing conditions. An alternative route to reducing loss in the HSQ layer under these membranes may be to use high-dose electron beam exposure.[125]

Other possible loss mechanisms in our diamond membrane-HSQ devices are absorption loss within the diamond membrane itself and absorption loss at the TiO_2-diamond interface. Despite high- quality overgrowth, the diamond membranes used in this work likely contain

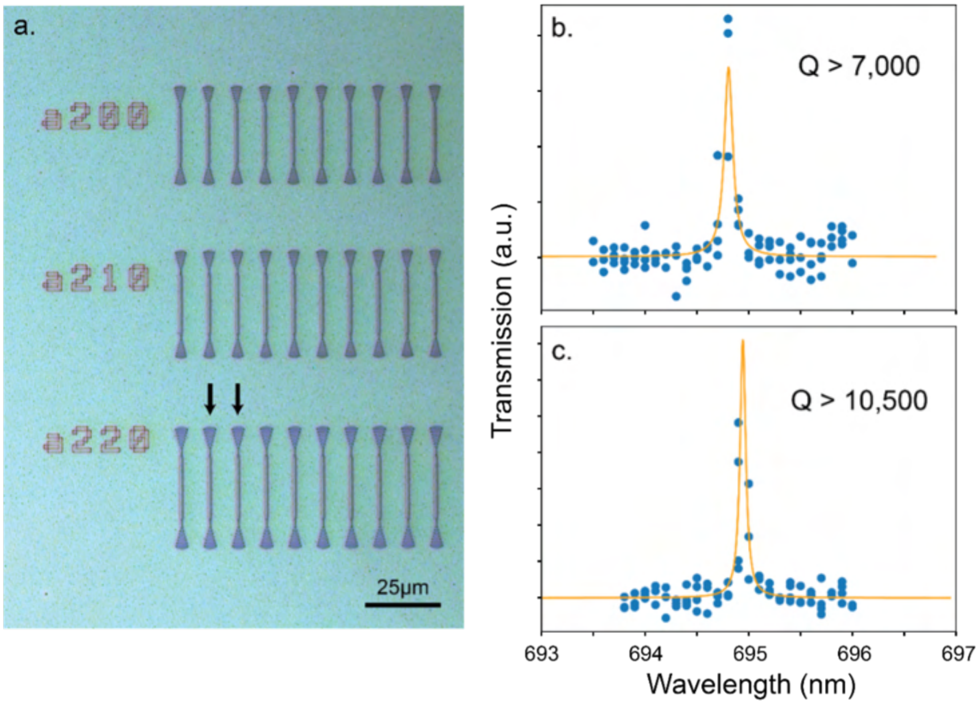

Figure 4.2 – 1D cavities on HSQ. (a) Microscope image of 1D photonic crystal cavities fabricated directly on a 500 nm-thick layer of annealed HSQ. (b,c) Transmission spectra for 25-fin devices with 200 nm fin pitch indicated with arrows in (a). Spectrometer-limited linewidths indicate quality factors greater than 7,000 and 10,500.

more optically active crystal defects than bulk diamond. Meanwhile, the adhesion of the TiO_2 photonic structures to the diamond membranes is fairly weak. Although this feature is an advantage when it comes to iterating the device fabrication procedure, it may also indicate a layer of optically lossy unsatisfied bonds.

While examining the additional loss mechanisms for devices fabricated on diamond will likely improve their performance further, the experimentally measured quality factors are already sufficient for high-efficiency spin-photon interfacing with diamond color centers. To determine the maximum Purcell factor achievable with our 1D photonic crystal cavities, we used Lumerical FDTD software to simulate their mode volumes. The equation used for mode volume is:

$$V_{\text{mode}} = \frac{\int_V \epsilon(r)|E(r)|^2 d^3r}{\max(\epsilon(r)|E(r)|^2)} \tag{4.1}$$

where $\epsilon(r)$ is the dielectric index at spatial position r and $E(r)$ is the electric field at this position. The calculated mode volume for a cavity simulated to operate at the silicon-vacancy center's zero phonon line (737 nm) on a 50 nm diamond membrane was:

$$V_{\text{mode}} = 6.179 \times 10^{-20} m^3 \approx 2.0\Big(\frac{\lambda}{n}\Big)^3 \tag{4.2}$$

Here we have used 2.35 as the index of refraction of the TiO_2 resonator. Taking the experimentally measured quality factor value of 4,400, we can determine the maximum Purcell enhancement at the peak of the cavity mode intensity profile using:

$$F_P = \frac{3}{4\pi^2}\Big(\frac{\lambda}{n}\Big)^3 \frac{Q}{V_{\text{mode}}} = \frac{3}{4\pi^2}\Big(\frac{737 \times 10^{-9} m}{2.35}\Big)^3 \frac{4,400}{6.179 \times 10^{-20} m^3} \tag{4.3}$$

This equation assumes that the cavity is on resonance with an SiV and that the SiV is aligned with the electric field vector at the cavity mode maximum. It gives a value of 175. Within the underlying diamond membrane, the electric field intensity is roughly 2/3 of the peak electric field intensity in the cavity cross-section, leading to a maximum Purcell factor of ≈ 115 for color centers residing within the membrane, as shown in Figure 4.1.

By comparing our quality factor and mode volume values to literature values elsewhere, we can estimate the cooperativity we expect to see when our TiO_2 cavities are coupled to diamond color centers. In the work presented in Ref. [126], a cooperativity $C = 1.4$ was achieved with a 1D cavity exhibiting $Q \approx 8,300$ and $V_{\text{mode}} \approx 1.8(\lambda/n)^3$, values similar to our system. Meanwhile in Ref. [127], $C > 100$ was demonstrated with cavities that exhibit $Q \approx 20,000$ and $V_{\text{mode}} \approx 0.5(\lambda/n)^3$. Since cooperativity is proportional to $\frac{Q}{V_{\text{mode}}}$, we may expect $C \approx$ 6-7 if we can achieve the same degree of color center placement precision as in that work. We conclude that we can reasonably expect cooperativity values in the range 1-10 for these integrated TiO_2/diamond membrane heterostructures, which is sufficient for quantum optical networking applications.

Finally, we note that this fabrication process can be iterated multiple times on one membrane and can generate a large number of resonators in arbitrary orientations. After TiO_2 resonators are fabricated, they can be mechanically removed via ultrasonication without removing or damaging the underlying membrane. Therefore, if alignment to a particular color center is not ideal, or if a fabrication step fails, additional attempts can be made. The data displayed in Figure 4.1c were acquired from the third round of cavity fabrication on a single membrane sample. Each of these three rounds yielded devices with typical quality factors $Q \approx 4,000$. Meanwhile, atomic force microscopy scans do not show significant difference to the surface roughness of the diamond between fabrication rounds. This flexibility is a distinct advantage compared to diamond etching methods, which require re-polishing and potentially re-implanting the diamond to generate new color centers for each iteration. Moreover, as pictured in Figure 4.1e, many devices can be fabricated at once and in arbitrary positions and orientations relative to one another, which is beneficial for on-chip device multiplexing.

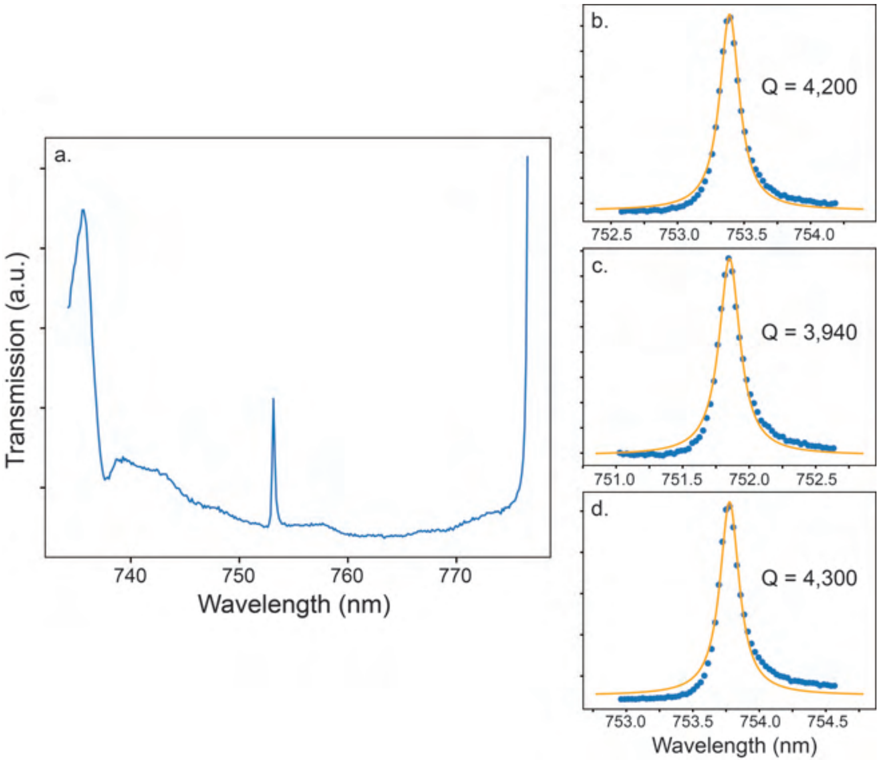

Figure 4.3 – Additional spectra of cavities on diamond. (a) Broadband transmission spectrum for a 25-fin TiO_2 cavity on a 50 nm diamond membrane. (b) Higher-resolution transmission spectrum for device measured in (a), displaying quality factor Q = 4,200. (c,d) Transmission spectra for two additional devices with the same geometry as in (a,b), displaying Q = 3,940 and Q = 4,300.

4.1.3 Conclusion

Integration of TiO_2 nanophotonic devices with diamond membranes offers a robust and non-invasive approach to optically addressing color centers that is more scalable and deterministic than conventional etched nanophotonics. Our ALD-based fabrication platform offers the dual benefits of minimized surface roughness and highly reproducible resonator spectra. Looking forward, we aim to use this platform to build quantum networks by aligning cavities to individual color centers within membranes and gas tuning their resonances to the defects' zero phonon line.[128] With high quality factors and low mode volumes, we anticipate that efficient spin-photon interfacing will be achieved. Finally, we note that this platform is flexible to both wavelength and substrate, allowing for integration with defects in silicon carbide,[129–131] rare earth ions,[13] or other material systems beyond diamond.

4.2 Integration with monolayer TMDs[†]

4.2.1 Introduction

In tightly confined, propagating optical fields, Gauss' law requires that a rapidly varying electric field in the transverse direction must be accompanied by an electric field in the longitudinal direction that is 90° out of phase with the transverse field.[132,133] The transverse and longitudinal fields combine to create regions of elliptical polarization, in which the transverse optical spin angular momentum is locked to the direction of the wavevector of the optical mode. In these chiral fields, the optical spin angular momentum is perpendicular to the propagation direction, in contrast to conventional circularly polarized free space optical fields. This phenomenon, referred to as optical spin-orbit coupling (OSOC), has been observed in a variety of experimental platforms, including optical fibers,[134–136] whispering gallery mode resonators,[136,137] photonic crystal waveguides,[138,139] plasmonic waveguides,[83]

[†] †. The work in this section was reported in Ref. [72]

and hyperbolic metamaterials[140] and metasurfaces.[120]

Photonic structures exhibiting OSOC can be coupled with circularly dichroic materials – *i.e.*, materials that interact selectively with circularly polarized light – to generate chiral light-matter interfaces. Such interfaces create light-matter interactions that depend on the propagation direction of light and provide a foundation for new photonic and plasmonic technologies, such as on-chip beam splitting for circularly polarized input light[141] and optically driven optical isolation.[142] Beyond classical systems, OSOC enables directional quantum nonlinear interactions between quantum states of photons and matter and has stimulated the development of chiral quantum optics.[135,139,143] More broadly, chiral interfaces have found application in the sensitive optical detection of chiral molecules with aims towards enhanced biosensing.[144–147]

An emerging platform for these chiral optical interfaces are atomically thin transition metal dichalcogenides (TMDs). As discussed in Chapter 1, TMD monolayers are direct bandgap semiconductors with optical resonances in the visible and near-infrared range dominated by excitonic states.[148,149] Due to broken inversion symmetry in the monolayer crystal lattice, two inequivalent sets of bandgap minima exist at the momentum space K points (i.e., K and K' valleys), which couple to light of opposite circular polarization.[64,65,150,151] Preliminary demonstrations with plasmonic, nanowire, and photonic crystal systems[83,152–156] have shown the feasibility of coupling light to TMD valley excitonic states through OSOC. However, the scalable, deterministic incorporation of such architectures in existing integrated photonic platforms is challenging to achieve. Moreover, the chiral TMD interfaces demonstrated so far are passive. A scalable nanophotonic-TMD interface equipped with active electrical tunability could enable new applications in optoelectronic and integrated photonic technologies. Valley polarization, which characterizes the circular dichroism of TMDs, can be modified by electrostatic doping,[157] providing an avenue for active control. Additionally, in monolayer TMDs the exciton valley index determines the spin configurations of the underlying charge carriers in charged excitonic states.[64] Therefore, a photonic-TMD interface also opens the opportunity to control semiconductor spins[158] with integrated photonics, enabling nanoscale optical manipulation of solid-state memories.[159,160]

4.2.2 Directional optical spin-orbit coupling

Here, we demonstrate an interface which exploits these unique material properties to realize electrically tunable chirality. The interface is based on the nanophotonics fabrication platform described in Chapter 3 and can be applied to a range of devices, facilitating broader application of chiral interfaces in nanophotonic circuitry. Our device consists of a TiO_2 nanophotonic waveguide fabricated on a hexagonal boron nitride (hBN)-encapsulated WSe_2 monolayer (Figure 4.4a). Encapsulation with hBN significantly reduces inhomogeneity in TMDs[57,62] and serves as a dielectric for electrostatic tuning.[161] Electrical control is achieved with few-layer graphene back-gate and contact flakes. We fabricate TiO_2 waveguides on top of these heterostructures using templated atomic layer deposition.[89] We again emphasize that this fabrication method produces low-loss nanophotonic structures (Figure 4.4b) without damaging the underlying substrate, making it ideal for interfacing with two-dimensional materials. Following waveguide fabrication, the WSe_2 monolayer exhibits narrow linewidth excitonic emission (Figure 4.4c), confirming that our photonic integration process generates minimal inhomogeneities in the van der Waals heterostructure and is suitable for photonic integration with TMDs.

Figure 4.4d illustrates the directional coupling that emerges between the waveguide modes and the TMD material. The electric field distribution of the propagating TE mode is tightly confined (waveguide width $< \lambda/2$), manifesting in-plane, circularly polarized evanescent fields (Figure 4.4d, right inset). The sign of the polarization, σ^+ or σ^-, inverts across the waveguide and with propagation direction. Depending on location, excitons in the K and K' valleys (Figure 4.4d, left inset) will selectively couple to left- or rightward propagating modes

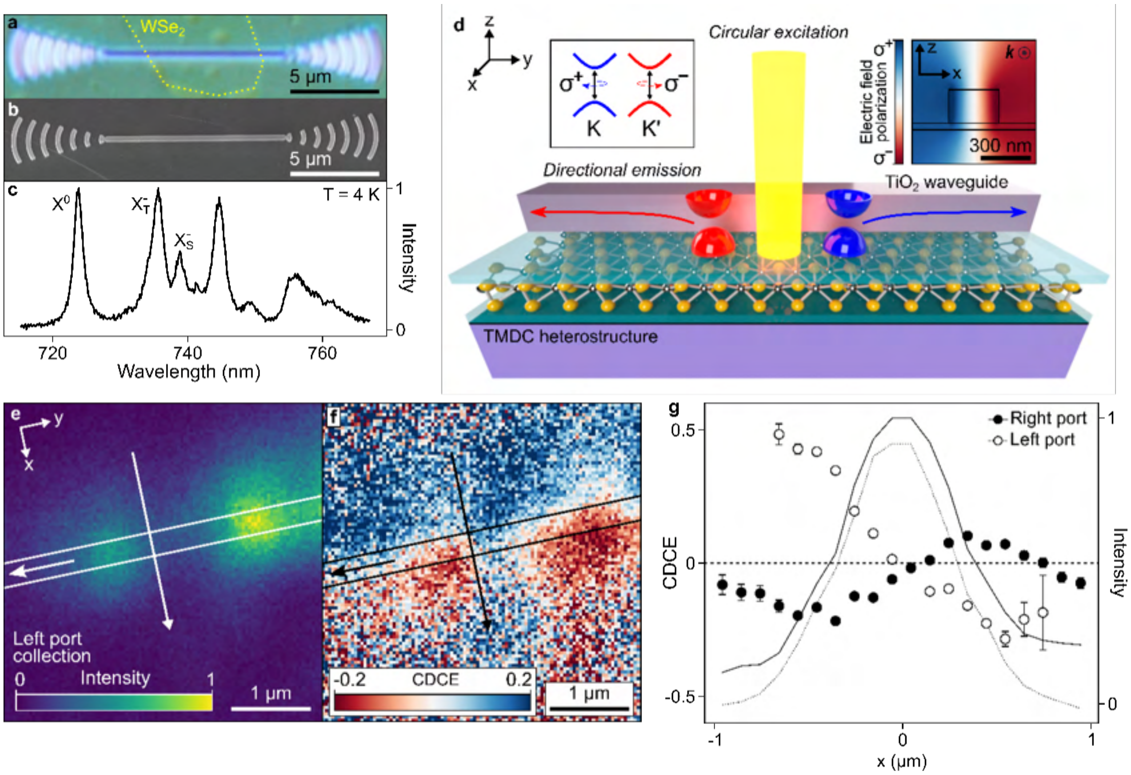

Figure 4.4 – (a) Optical and (b) scanning electron microscope images of the TMD-waveguide interface. (c) PL of encapsulated WSe$_2$ at 4K shows prominent exciton, trion and charged biexciton peaks. (d) Schematic depicting chiral-directional coupling. Left inset: Valley-dependent optical selection rules of monolayer TMDs. Right inset: Polarization of electric field intensity distribution of waveguide mode propagating out of the page. (e) Spatial mapping of PL intensity measured through the left port under linear far-field excitation. (f) Spatial mapping of CDCE through the left port under circular far-field excitations. (g) Line cuts of CDCE across the waveguide along the arrow direction in (e) and (f) for left (open circles) and right (solid circles) ports. Lines show total intensity (i.e., $I_{GP}^{\sigma+} + I_{GP}^{\sigma-}$) measured for each port.

of the waveguide, thus establishing chiral-directional coupling at the waveguide-monolayer interface.

To characterize the interface, we first generated excitons and observed their radiative emission into the guided optical modes of the waveguide. The monolayer is excited from the far-field by a 660 nm laser with a spot size $\approx$ 495 nm. Excitonic photoluminescence (PL) couples to the waveguide and is detected by collecting the light scattered from gratings at the waveguide ends. Figure 4.4e displays the measured PL intensity from the left port when a linearly polarized excitation is scanned around the waveguide. To study the chiral-directional coupling, we switch the polarization of the excitation laser from linear to circular, σ^+ and σ^-, creating valley-polarized excitonic states that preferably emit with the same polarization as the excitation (Figure 4.4d). We characterize the interface by the chiral-directional coupling efficiency:

$$\mathrm{CDCE}(x,y) = \frac{I_{GP}(x,y)^{\sigma^+} - I_{GP}(x,y)^{\sigma^-}}{I_{GP}(x,y)^{\sigma^+} + I_{GP}(x,y)^{\sigma^-}} \tag{4.4}$$

where $I_{GP}(x,y)^{\sigma^+(\sigma^-)}$ is the PL intensity measured from a specific grating port under $\sigma^+(\sigma^-)$ excitation at position (x,y). Figure 4.4f shows the spatial mapping of the CDCE for left port collection. As anticipated,[83,155] we observe that the sign of the CDCE inverts as the excitation spot crosses the waveguide, approaching a magnitude of 20%, and that the sign of the CDCE flips between the two outcoupling ports (Figure 4.4g). We also note that under linearly polarized excitation, the chiral-directional coupling vanishes as expected. For both ports, the CDCE goes to zero near the center of the waveguide, where the mode polarization is linear (Figure 4.4d, right inset). Far from the waveguide center, the CDCE also falls to zero as low-signal noise dominates. These experimental signatures directly verify the predicted chiral interface between the TMD monolayer and photonic waveguide.

The integration of contacts and electrodes in our device architecture enables us to electrically dope the TMD monolayer and, in turn, control the chirality of our integrated photonic interface. To study this tunability, we apply a gate voltage to the TMD monolayer and investigate the impact on the chiral–directional coupling. Figure 4.5a,b show the spatially mapped CDCE measured for gate voltages of -5 V and 5 V, respectively. The CDCE notably diminishes under negative applied bias. Comparing transverse line cuts across the waveguide (Figure 4.5c), the CDCE spatial dependence at -5 V flattens to zero, whereas at +5 V it displays the expected crossing at x = 0 µm . At a fixed displacement of ≈ 300 nm away from the waveguide, we observe a sharp transition in CDCE from near 0% at -5 V to around 15% at -2.5 V (Figure 4.5c, inset). This result directly demonstrates the active electrical control over the chirality of the TMD–waveguide interface.

To investigate the electrical tuning in more detail, we perform spectrally resolved measurements of the out-coupled photoluminescence. Figure 4.5d-g show gate-dependent PL spectra collected from the right grating port for fixed-position off-waveguide σ+ and σ- excitations. We attribute characteristic peaks to neutral and charged exciton and biexciton states delineated in recent literature.[157,162,163] Combining this spectroscopic information with the electrostatic control afforded by our high-quality interface, we analyze the chiral-directional coupling for each excitonic state. From the spectra in Figure 4.5d-g, we find that the positive trion (X^+) and neutral exciton (X^0) states display balanced emission into the waveguide independent of the excitation polarization. In contrast, the negative trion (X^- and X^{--}) and biexciton (XX^0 and XX^-) states exhibit directional emission. More completely, Figure 4.5h-k(l-o) show the wavelength-resolved right (left) port CDCE versus the position of the excitation beam. Minimal variation is observed for the X^+ and X^0 peaks, whereas for the X^-, X^{--}, XX^0 and XX^- peaks, the CDCE inverts across the waveguide and reaches magnitudes near 20% on either side. These measurements indicate that the different excitonic states in the monolayer exhibit varying degrees of chiral-directional coupling and that the electrostatic control of this coupling correlates with switching between dominant excitonic states.

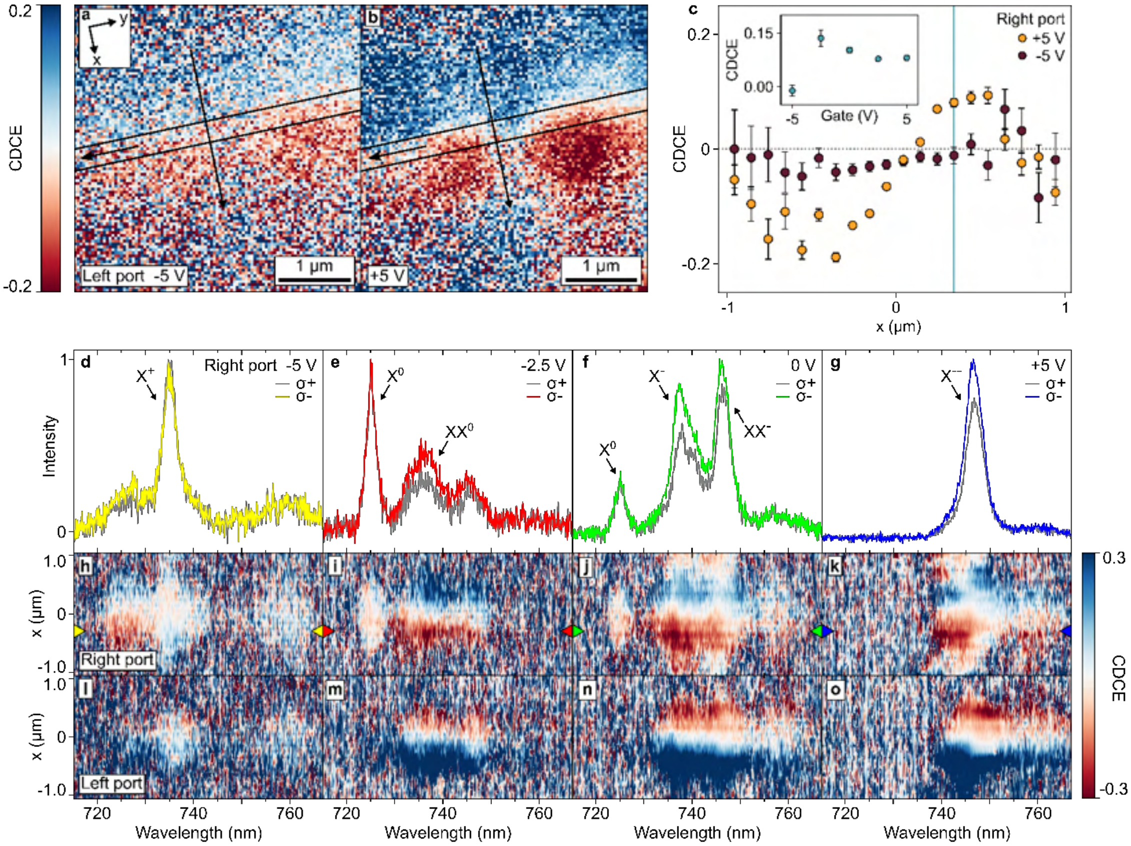

Figure 4.5 – Electrostatic tuning of waveguide-TMD interface. (a,b) Spatial mapping of CDCE of emission collected through left port under applied gate biases of (a) -5 V and (b) 5 V. c, Line cuts of CDCE of emission collected through right port along the arrow direction in a and b. Inset: Gate dependence of CDCE at x = +300 nm (blue vertical line in c). d-g, PL out-coupled from right port under selected gate voltages with σ^+ and σ^- excitations fixed at x = -300 nm. Excitonic states are labeled. h-k (l-o), Spectrally resolved spatial mapping of right (left) port CDCE at selected voltages. Colored triangles indicate the corresponding spectra line cuts in d through g.

4.2.3 Spin-polarized exciton diffusion

In addition to enabling electrical control over chiral-directional coupling of the excitonic emission, the TMD-waveguide interface opens new possibilities to locally create and manipulate excitons and spins. With improvements in sample quality and the observation of long-lived excitons in heterostructures, exciton diffusion in 2D semiconductors has recently garnered increasing interest, providing a context for fundamental explorations of planar spatial dynamics in systems with many-particle interactions[164,165] and enabling such optoelectronic technologies as room-temperature excitonic transistors[166]. Unlike in bare, few-layer samples,[83] the encapsulated TMD monolayers in our interface provide reduced-disorder environments for studying exciton propagation[167] and preserve spin-valley locking, allowing the simultaneous transport of spin-polarized charge carriers. Compared with the far-field optical excitations currently utilized to drive exciton diffusion, the waveguide modes of high-index nanophotonic structures can act as compact, tailored, on-chip sources of exciton fluxes. Moreover, the high degree of circular polarization of their evanescent fields enables the generation of valley-polarized exciton fluxes,[167,168] which can be directionally reconfigured (Figure 4.6a). Therefore, a new modality for injecting spin currents in semiconductors with integrated photonics – as opposed to with conventional ferroelectric contacts[169,170] – can be realized, promising advancements in optical computing and spintronics.[171]

With our device, we first show that the waveguide can locally generate diffusive excitons. To probe this functionality, we couple the excitation laser into the right grating port and collect photoluminescence emitted from the TMD monolayer into the far-field. Figure 4.6b shows the spatial distribution of exciton PL spectrally selected over wavelength regions of interest. The shaded area illustrates the simulated electric field intensity of the waveguide mode. The quickly decaying evanescent tail implies a large density gradient of the excitonic states generated by the mode, which induces their diffusive transport away from the waveguide. Considering the measured resolution of our collection channel, we compute the

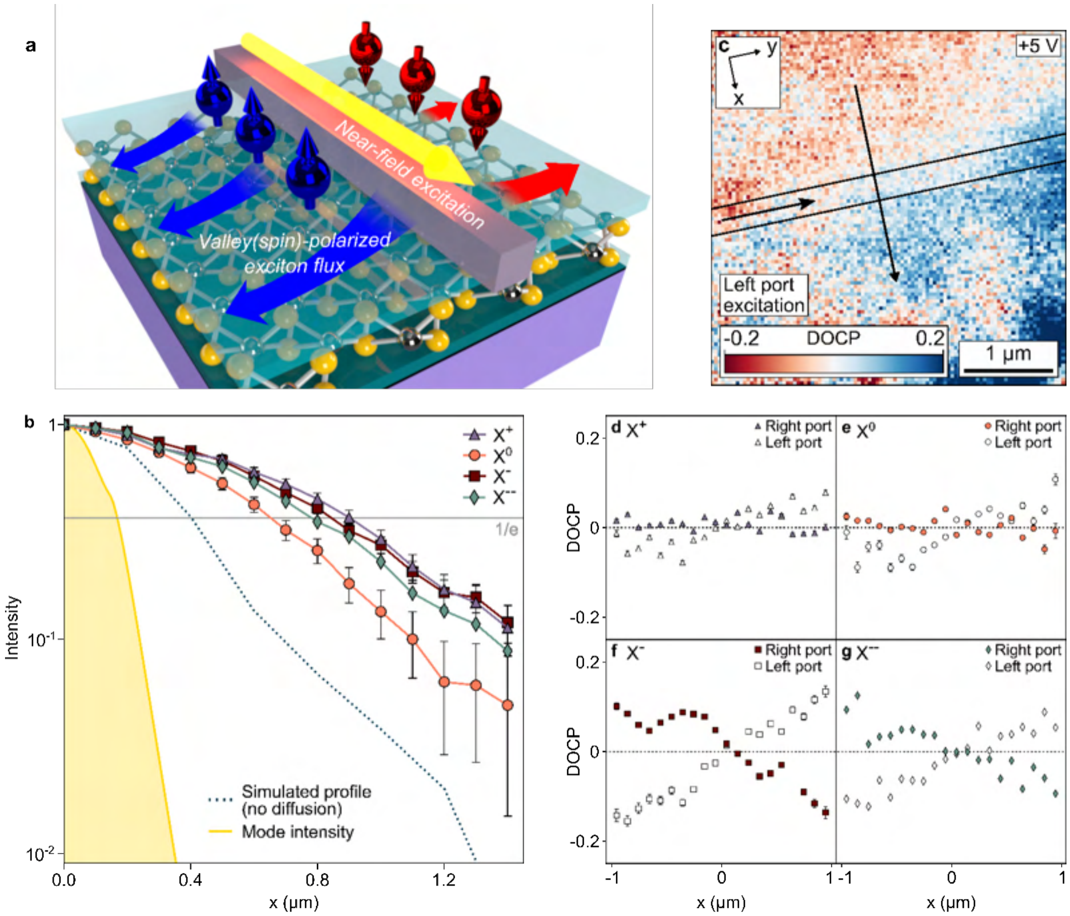

,

Figure 4.6 – (a) Schematic of valley(spin)-polarized exciton flux generation. Outward arrows (blue/red) indicate diffusion of oppositely valley-polarized excitons carrying spins for fixed propagation direction of the waveguide excitation mode (yellow). (b) Normalized PL intensity distributions versus distance from waveguide (center at x = 0 μm) for different excitonic states. Shaded area is the simulated electric field intensity profile of the guided mode in the waveguide. Dashed line shows the simulated collection profile in the absence of diffusion given experimental resolution. (c) DOCP map under 5 V gate bias, left port excitation, and far-field collection. (d-g) DOCP of different excitonic states along the arrow direction in (c) Open (solid) circles correspond to rightward (leftward) propagating waveguide excitation in-coupled through the left (right) grating port.

anticipated PL spatial distribution in the absence of exciton diffusion (dashed line in Figure 4.6b). We find that the profiles of the excitonic states extend beyond this boundary, indicating their diffusion away from the waveguide. For the charged excitons, both negative and positive, we extract 1/e diffusion lengths $L_{X^{\pm}} \approx 0.45$ µm based on the predicted no-diffusion profile. The neutral exciton displays a diffusion length $L_{X^0} \approx 0.25$ µm . These diffusion lengths of hundreds of nanometers are comparable to literature values.[172] The excellent sample quality and comprehensive electrostatic control over our interface enable this extraction of state-specific diffusion.

We next examine the valley(spin)-polarization of these near-field driven exciton fluxes. As before, the evanescent fields on either side of the waveguide exhibit opposite nearly circular polarizations and therefore populate excitonic states in opposite valleys (Figure 4.6a). To measure this resulting valley polarization, we analyze the circular polarization of the far-field PL. The valley polarization of the excitonic states is characterized by the PL degree of circular polarization:

$$DOCP(x,y) = \frac{I_{FF}(x,y)^{\sigma^+} - I_{FF}(x,y)^{\sigma^-}}{I_{FF}(x,y)^{\sigma^+} + I_{FF}(x,y)^{\sigma^-}} \tag{4.5}$$

where $I_{FF}(x,y)^{\sigma^+(\sigma^-)}$ is the $\sigma^+(\sigma^-)$ component of the far-field PL intensity collected at position (x,y). Figure 4.6c shows the DOCP measured under left port excitation and 5 V gate bias, confirming the generation of valley-polarized excitonic states. Figure 4.6d-g display the position-dependent, spectrally resolved DOCP for the respective X^+, X^0, X^-, and X^{--} peaks. Like the CDCE (Figure 4.5d-g) results, negative trions exhibit a large DOCP, whereas positive trions and neutral excitons show nearly zero DOCP. We also note the presence of prominent dark trion peaks at ≈ 750 nm.[173] Due to their linear out-of-plane dipole moment,[161] dark trions predominantly couple to the TM mode, showing biased DOCP with a spatial profile independent of the excitation port. For negative trions, due to valley-spin locking, the paired hole spin is fixed by the valley index. Thus, spin-polarized holes are injected with the valley-polarized X^- and X^{--} states. With the diffusion measurements described above, we conclude that our chiral photonic interface serves as a directionally reconfigurable source for injecting hole spin currents in atomically thin semiconductors.

4.2.4 Conclusion

We have demonstrated a photonic waveguide interfaced with an hBN-encapsulated, electrically gated WSe_2 monolayer. The interface exhibits a CDCE that is electrically tunable from 0% to 20% and generates valley(spin)-polarized exciton fluxes via near-field excitation. Beyond linear waveguides, our versatile nanophotonic fabrication method can interface TMDs with more complicated photonic structures where device geometry and size are limited only by the constraints of advanced lithography,[89] enabling photonic ring modulators and inteferometers[174] and exciton–polaritons in photonic crystals.[156] Combined with recent advances in large-area growth,[175] exfoliation,[74,75] and assembly[176] of two-dimensional materials, which will improve heterostructure yield and scalability beyond current limitations, this work establishes a universal platform for their deterministic, wafer-scale integration with nanophotonic circuitry. Importantly, this interface's tunable chirality, previously unavailable in other chiral optical interfaces, relies on the doping-dependent valley dynamics of exciton states in the TMD monolayer. Multilayer and twisted van der Waals heterostructures display engineered, exotic valley properties[168,177,178] that can also be combined with this waveguide interface for additional chiral functionalities, such as gate-reversible emission routing,[179] and offering new photonic logic and control schemes based on two-dimensional materials. In addition, nanophotonic driving of exciton diffusion in atomically thin semiconductors creates a bridge between distributed photonic elements and local excitonic circuits.[180–182] Moreover, near-field optical pumping through chiral TMD–photonic interfaces can be used to generate the spin polarization of resident charge carriers in monolayers.[73,183,184] Such optically prepared spin-polarized electronic states, which are sensitive to the carrier doping level, can break the time-reversal symmetry of the interface, enabling gate-activated all-optical non-reciprocity in integrated nanophotonic architectures.[185]

Chapter 5

Multi-resonant TiO_2 Bullseye Antennas[†]

ABSTRACT

Integrated devices that generate multiple optical resonances in the same volume can enhance on-chip nonlinear frequency generation, nonlinear spectroscopy, and quantum sensing. Here, we demonstrate circular Bragg antennas that exhibit multiple spatially overlapping, polarization-selective optical resonances. Using templated atomic layer deposition of TiO_2, these devices can be fabricated on arbitrary substrates, making them compatible with a wide range of nonlinear materials and sensing targets, and couple efficiently to underlying films. In this work, we detail the design, simulation, and fabrication of all-dielectric multi-resonant bullseye antennas and characterize their performance using polarized broadband reflection spectroscopy.

5.1 Introduction

By confining and enhancing optical fields at pre-designed wavelengths, nanophotonic resonators enable coherent light-matter interactions,[30,187] ultra-resolution quantum and biosensing,[10,188] integrated light sources,[189,190] and more. Nonlinear light-matter interactions underly on-chip nonlinear frequency conversion, critical for entangled photon sources and optical information processing,[191–195] and are enhanced by devices which spatially overlap multiple optical resonances at different frequencies. Similarly, coherent anti-Stokes Raman spectroscopy and other nonlinear spectroscopies can be made more efficient and extended to smaller probe volumes by simultaneously confining the pump and signal frequencies.[196,197]

[†]. The work in this section was reported in Ref. [186]

Meanwhile, in optical sensing applications, multi-resonant structures can increase optical pumping efficiency while simultaneously increasing fluorescence emission rates.[197,198]

However, generating devices which overlap multiple optical resonances at arbitrary frequencies is challenging, both in terms of design and fabrication. Many nanophotonic resonators rely on photonic band gap engineering, in which a resonance exists within forbidden photonic states. Although multiple resonances can exist within one band gap, their frequency separation is constrained by the width of the photonic band gap, and it is difficult to independently control the field strength and quality factors of the resonant modes. Ring resonators, meanwhile, do not rely on band gap engineering, support a series of standing wave resonances, and are generally easier to fabricate than photonic crystals. These devices are commonly used for on-chip nonlinear frequency generation and for sensing[192,199–201] though their disadvantages include larger footprints and mode volumes than photonic crystal cavities. For nonlinear applications, a key challenge is that the cross-sectional spatial profiles of ring resonator modes vary with wavelength, and careful engineering of waveguide cross sections is often required to enable substantial mode overlap.[202]

Alternatively, circular Bragg resonators (CBRs), also called bullseye antennas, offer unique benefits for nanophotonic engineering. These structures efficiently couple to low-NA far-field beams and exhibit smaller mode volumes and footprints than ring resonators.[16,113,203–207] Additionally, CBRs offer a relatively broadband optical response and are therefore easier to spectrally overlap with targeted dipole emission. CBRs were initially used for classical optoelectronic devices like optical switches and lasers.[203–205] More recently, they have been integrated with a variety of quantum and low-dimensional materials. CBRs have been etched into diamond membranes to increase collection efficiency of nitrogen-vacancy center emission,[113] used to efficiently extract entangled photon pairs from quantum dots,[206] and integrated with two-dimensional semiconductors to enhance photoluminescence and second harmonic generation.[16,207]

Breaking azimuthal symmetry allows multiple resonances in CBRs while maintaining their unique advantages. This symmetry breaking enables both wavelength and polarization multiplexing, as segments with different grating periods behave like polarization-selective antennas. This concept was demonstrated in plasmonic CBRs fabricated by focused ion beam milling of epitaxially grown single-crystal silver.[208] However, plasmonic devices suffer from large nonradiative losses compared to dielectric structures. Moreover, silver epitaxy and ion milling offer limited integration capability with many nonlinear materials.

In this work, we use templated atomic layer deposition (ALD) to build all-dielectric TiO_2 bullseye antennas which exhibit multiple polarization-sensitive, spatially overlapping resonances. We previously demonstrated that this fabrication approach can efficiently couple nanophotonic devices with underlying materials and can be integrated with arbitrary substrates.[89] Specifically, templated ALD maintains the optical performance of underlying 2D materials[72] and is uniquely suited for integration with quantum emitters in membranes.[53,89] Here, we detail the design, fabrication, and spectroscopic characterization of multi-resonant TiO_2 bullseye antennas and demonstrate their potential to interface with underlying optical materials.

5.2 Device design and simulation

5.2.1 *Device geometry and operating principle*

Circular Bragg resonators (CBRs) typically feature a central disk concentric with periodically spaced rings. The rings are spaced according to the second order Bragg condition and serve the dual function of reflective feedback to the central cavity and deflection out-of-plane, thereby coupling the cavity mode to low-NA propagating beams. With quality factors on the order of 102, these devices offer a relatively broadband response (several nm), combined with a small footprint (< 5 µm) and mode volume ($\approx (\lambda/n)^3$). Variations on this basic geometry that have previously been explored include chirped cavities for high-Q applications,[209] elliptical cavities for geometric birefringence,[206] and Doppler gratings for wavelength multiplexing.[196]

For the azimuthally segmented, multi-resonant devices we designed, the operating mechanism is the same as that of basic CBRs, except each segment has its own central disc radius and grating pitch. The structure is symmetric about its center, with each grating pitch repeated on the opposite side of the device. As illustrated in Figure 5.1a, these devices can be defined by six parameters: a_1 and a_2 are the two grating periods, R_1 and R_2 are the corresponding central disc radii, and θ_1 and θ_2 define the angular spread of each segment, with $\theta_1 + \theta_2 = 180°$.

To demonstrate the potential of multi-resonant bullseye antennas to interface with underlying materials, we used finite difference time domain (FDTD) simulations (Lumerical) to model devices on 50 nm TiO_2 films on fused silica (n = 1.4) substrates, as depicted in Figure 5.1b. Because the index of refraction of TiO_2 is close to that of lithium niobate ($n \approx 2.3$), diamond ($n \approx 2.4$), silicon carbide ($n \approx 2.6$), and hexagonal boron nitride ($n \approx 2.2$), this substrate choice is a suitable stand-in for materials relevant to a range of practical applications in nonlinear and quantum optics. We note that the resonator modes are concentrated within the bullseye antenna and in the film directly underneath, as shown in Figure 5.1c,d, in contrast to zone plates or metalenses which are often used to focus an incident beam to a point away from the structure itself.[210]

We identified device parameters that concentrated multiple resonances within the underlying film by linearly varying the two grating periods and disc radii and monitoring the electric field intensity underneath the resonator. In all simulations, the height of the devices was fixed at 300 nm, and the index of refraction of TiO_2 was input from ellipsometry data. Additionally, the duty cycle of each grating was set such that the width of each grating element was equal to the grating period divided by 2.1. Once resonance conditions were

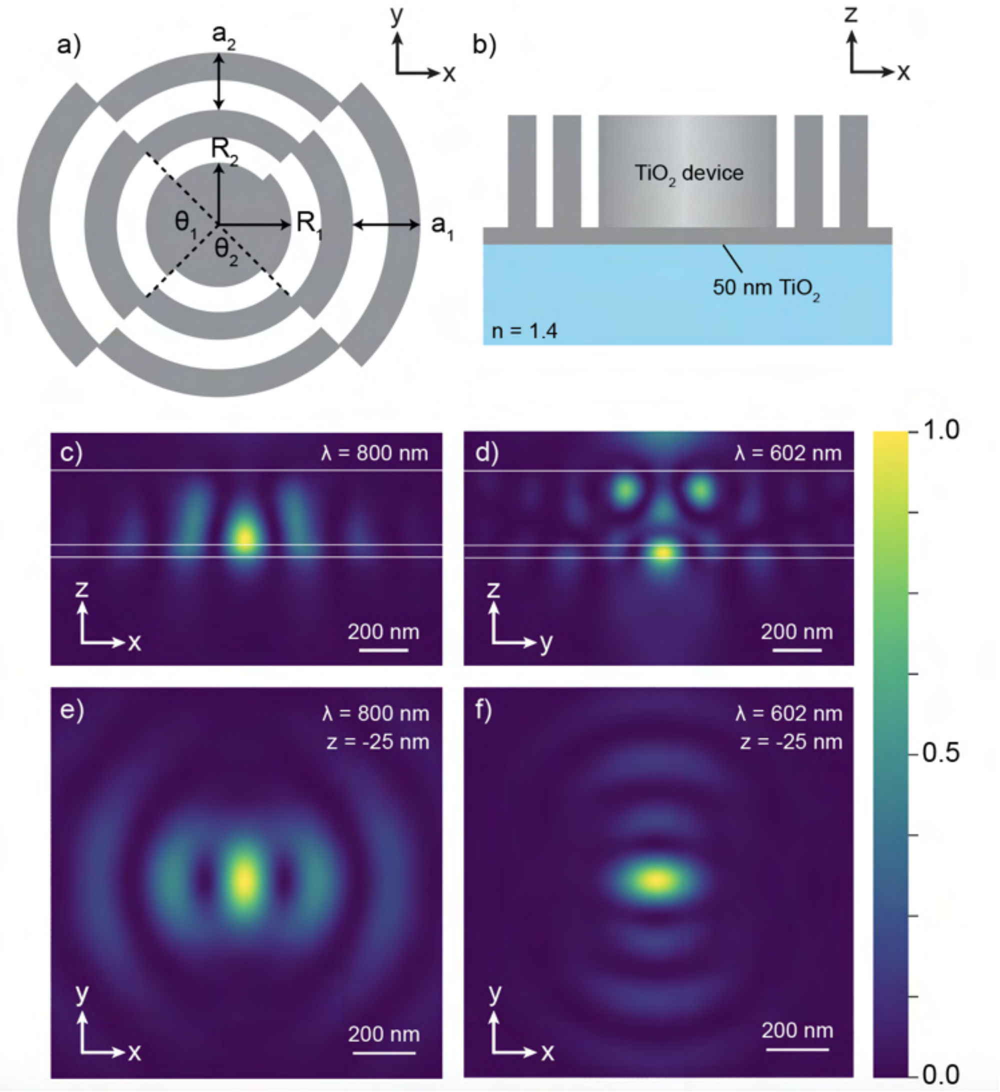

Figure 5.1 – Multi-resonant device design (a) The geometrical parameters that define the device are the radius of the central disc segment for each resonance (R_1, R_2), the corresponding pitch values (a_1, a_2), and the angles subtended by each segment (θ_1, θ_2, where $\theta_1 + \theta_2 = 180°$). (b) Side view of the simulated device and substrate. (c, d) Simulated electric field intensity in the x-z and y-z planes for a device with resonances at 800 nm (c) and 602 nm (d) on 50 nm TiO_2 film. (e, f) Simulated electric field intensity in the x-y plane at the center of the underlying film (z = -25 nm) for each of the two resonances, demonstrating substantial mode overlap. All field intensity plots are normalized.

identified, we found that each resonant wavelength varies linearly with small changes to either the central disc radius or the grating period. However, a large variation in one of these parameters generally leads to a loss of the resonance condition without a compensating adjustment in the other. We therefore identified a series of pairs of parameters that yielded strong resonances to explore further. This design process, which relies on individual variable sweeps, can likely be further optimized using field-based or inverse design methods.[73,211]

In Figure 5.1e,f, we plot the in-plane electric field intensity profiles underneath (z = -25 nm) a device with parameters (a_1, R_1, a_2, R_2) = (179, 212, 233, 248) nm, which generates resonances at both 800 and 602 nm. These results demonstrate substantial mode overlap at the center of the underlying film, even for wavelengths separated by nearly 200 nm.

5.2.2 Simulated incident beam enhancement

To investigate the polarization selectivity of the multi-resonant TiO_2 bullseye antennas, we simulated a focused, linearly polarized Gaussian beam normally incident on the center of the device and varied its polarization angle. Figure 5.2a and Figure 5.2b illustrate that perpendicularly polarized beams couple selectively to one resonance or the other. Imagining a line that passes through the center of a particular grating segment, a beam polarized perpendicular to that line will couple most effectively to the resonance defined by that segment. In the illustration, the orange (blue) beam preferentially couples to the shorter (longer) pitch grating.

We recorded the simulated electric field intensity at the center of the TiO_2 film underneath the bullseye resonator (z = -25 nm) as the beam source polarization was varied. Figure 5.2c-e plot in polar coordinates the intensity enhancement at the two resonant wavelengths of a given device as a function of beam polarization angle. All three of the dual resonance devices demonstrated here display clear polarization selectivity, regardless of the spectral separation of the two primary resonances. These devices demonstrate that the multi-resonant bullseyes

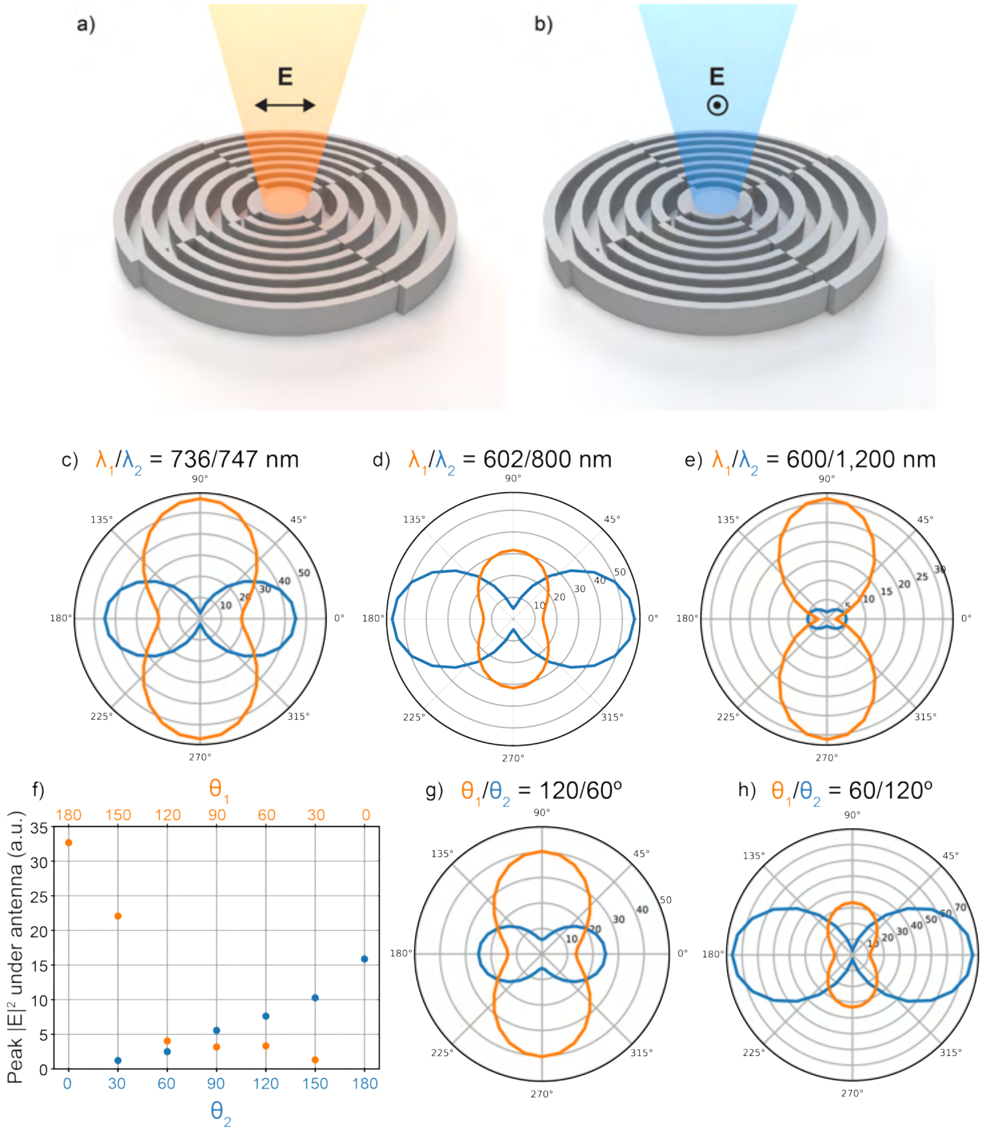

Figure 5.2 – Incident beam intensity enhancement.(a, b) Incident beams polarized in the x-direction (a) and in the y-direction (b) preferentially couple to different resonances in the azimuthally segmented bullseyes. (c-e) Simulated electric field intensity in the film underneath the devices (z = -25 nm) as a function of incident beam polarization for different combinations of resonances. In these three plots, $\theta_1 = \theta_2 = 90°$. (f) Peak electric field intensity in the underlying film for the same device as in (d) as a function of θ_1 and θ_2. (g, h) Electric field intensity (z = -25 nm) versus beam polarization for $\theta_1 = 120°$ (g) and $\theta_1 = 60°$ (h). In these two plots, the other device parameters are the same as in (d) and (f).

can be designed for two wavelengths that are relatively close together (Figure 5.2c), several hundred nm apart (Figure 5.2d) or even for fundamental and second harmonic wavelengths (Figure 5.2e).

Varying the angle subtended by each segment of the device offers a method of tuning the relative intensity of the two resonances. Figure 5.2f demonstrates that as θ_1 (θ_2) is increased (decreased) the shorter wavelength resonance becomes more (less) intense and vice versa. Importantly, even when θ_1 and θ_2 are not 90°, the device retains its selectivity to orthogonal polarizations, as shown in Figure 5.2g and Figure 5.2h.

5.2.3 Simulated dipole emission enhancement and out-coupling profile

Next, using a point dipole source located in the center of the underlying film (z = -25 nm), we simulated the Purcell enhancement and far field emission profiles generated by the multi-resonant Bragg antennas. Like the case of an incident polarized beam, underlying dipoles with orthogonal, in-plane dipole moments (x or y) couple selectively to different resonances in the device, as illustrated in Figure 5.3a,b. Purcell factors were extracted directly from simulations using the built-in Lumerical FDTD analysis, which calculates these values based on the local density of optical states at the dipole position.

For each simulated device, we recorded the Purcell factor for dipole emission at the two resonant wavelengths as a function of the dipole orientation angle. Figure 5.3c-e plot these results in polar coordinates for the same devices that were investigated in Figure 5.2c-e, each with $\theta_1 = \theta_2 = 90°$. As expected, the Purcell factor for underlying dipoles displays a similar polarization selectivity as the intensity of incident beams displayed in the prior set of simulations. Likewise, varying the angle subtended by each resonance modulates the degree of dipole emission enhancement at the two resonant wavelengths. As θ_1 (θ_2) is increased (decreased) the shorter wavelength dipole is more (less) enhanced and vice versa. Here, the Purcell enhancement achieved by single resonance devices (θ_1 or $\theta_2 = 90°$) is in the

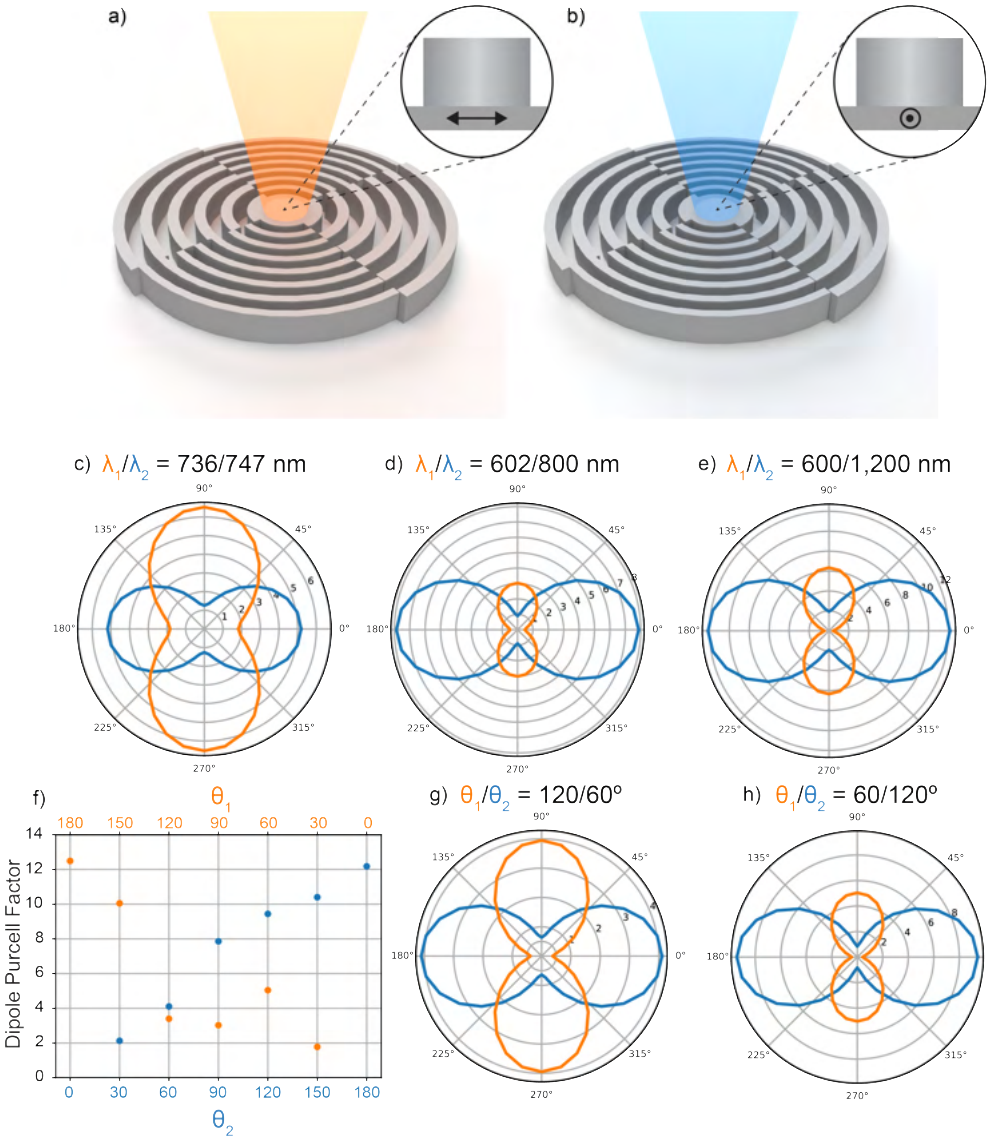

Figure 5.3 – Dipole Purcell enhancement. (a, b) Dipoles with moments in the x-direction (a) and in the y-direction (b) preferentially couple to different resonances in the azimuthally segmented bullseyes. (c-e) Simulated Purcell factor for a dipole in the center underneath the devices ($z = -25$ nm) as a function of dipole orientation for different combinations of resonances. In these three plots, $\theta_1 = \theta_2 = 90°$. (f) Peak Purcell factor for underlying dipoles for the same device as in (d) as a function of $\vartheta 1$ and $\vartheta 2$. (g, h) Purcell factor ($z = -25$ nm) versus dipole orientation for $\theta_1 = 120°$ (g) and $\theta_1 = 60°$ (h). In these two plots, the other device parameters are the same as in (d).

range 10-20, which is similar to previous work investigating dipole emission enhancement by CBRs,[113] despite the fact that these dipoles are underneath rather than inside of the device itself. Finally, we again see that when θ_1 and θ_2 are not 90°, the device retains its selectivity to orthogonal polarizations, as shown in Figure 5.3g and Figure 5.3h.

To test if the azimuthally segmented devices efficiently couple dipole emission into low-NA far field modes like single resonance CBRs, we investigated the spatial distribution of emission from underlying dipoles. For these simulations, we analyzed a device with resonances at 799 and 598 nm and considered emission profiles of dipoles oriented in the x- and y-directions that were on resonance with these two wavelengths. The dipoles were again placed in the center of the TiO_2 film under the antenna (z = -25 nm) and the device angles were $\theta_1 = \theta_2 = 90°$.

The cross-sectional electric field intensity profiles, plotted in Figure 5.4a,b with a $\log_{10}$ scale, demonstrate that dipole emission is significantly vertical, in both the upward (+z) and downward (-z) directions. This vertical characteristic is evident for both x-oriented and y-oriented dipoles at the appropriate resonance wavelength. Because the simulated substrate has a higher index of refraction (n = 1.4) than the surrounding medium (n = 1.0), more radiation is emitted downwards than upwards. Nevertheless, 41% of emission from an x-oriented dipole at 799 nm and 27% from a y-oriented dipole at 598 nm is directed upward [33].

Figure 5.4c and Figure 5.4d display the far field projections of upward dipole emission. While the emission profiles are not Gaussian, the emission of an x-oriented (y-oriented) dipole at the shorter (longer) wavelength resonance is primarily concentrated with NA = 0.75. In applications where collection efficiency is paramount, such as in quantum sensing, objectives with numerical apertures in air of up to 0.9 are commonly used and can therefore collect nearly the full upward emission from dipoles coupled to these multi-resonant devices. Combined with Purcell enhancement, we can expect multi-resonant bullseye antennas to significantly increase experimental collection efficiency.

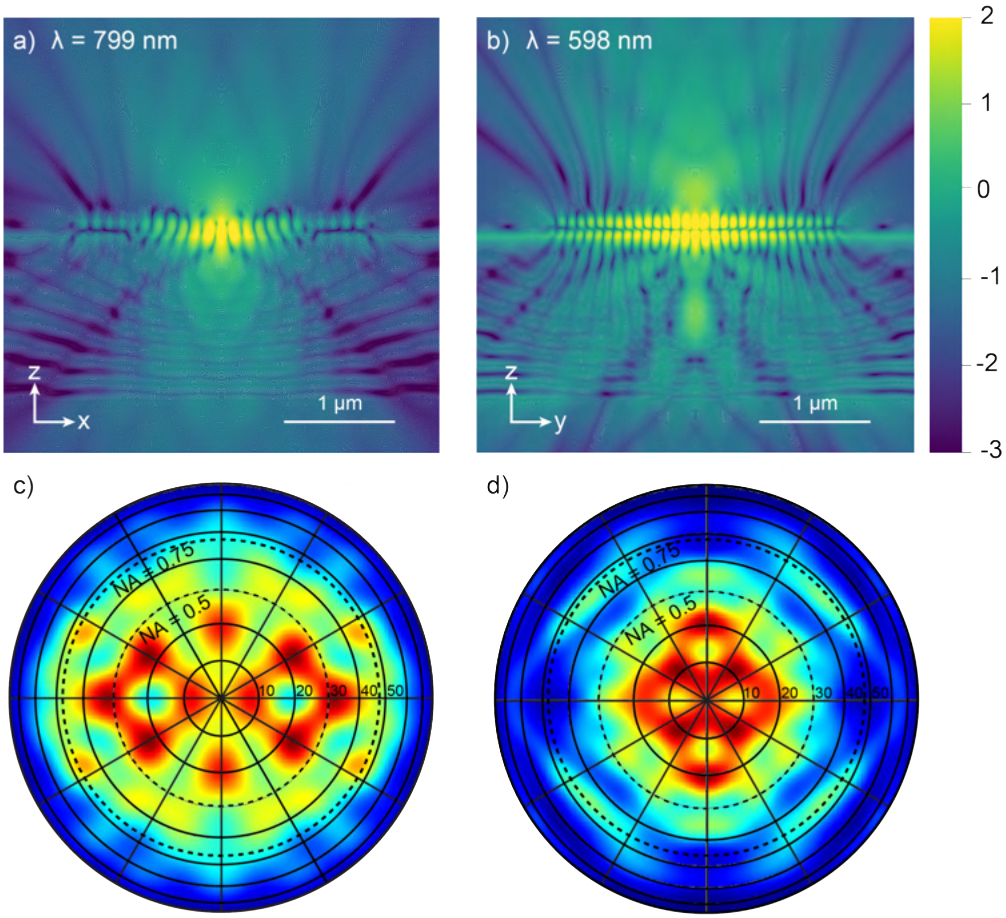

Figure 5.4 – Dipole emission profiles. (a, b) Cross sections of dipole emission profiles at the two device resonances, plotted with a $\log_{10}$ scale. In (a) the dipole orientation is in the x-direction and in (b) the dipole orientation is in the y-direction. (c, d) Far field electric field intensity projections of upward dipole emission. (c) Far field projection for a dipole orientated in the x-direction, on resonance at the longer resonance wavelength ($\lambda = 799$ nm). (d) Corresponding projection for a dipole oriented in the y-direction, on resonance at the shorter resonance wavelength ($\lambda = 598$ nm).

5.3 Nanofabrication with templated atomic layer deposition

The procedure used to fabricate the circular Bragg resonators is detailed in [28]. Briefly, electron beam lithography is used to define a device template into polymethyl methacrylate (PMMA), which is then filled by conformal deposition of high-index (n $\approx$ 2.4), low-loss TiO_2 via ALD. After excess TiO_2 is removed by dry etching, the PMMA template is stripped with a wet etch (Nanostrip) and the final devices are annealed on a hot plate at 250 C for two hours.

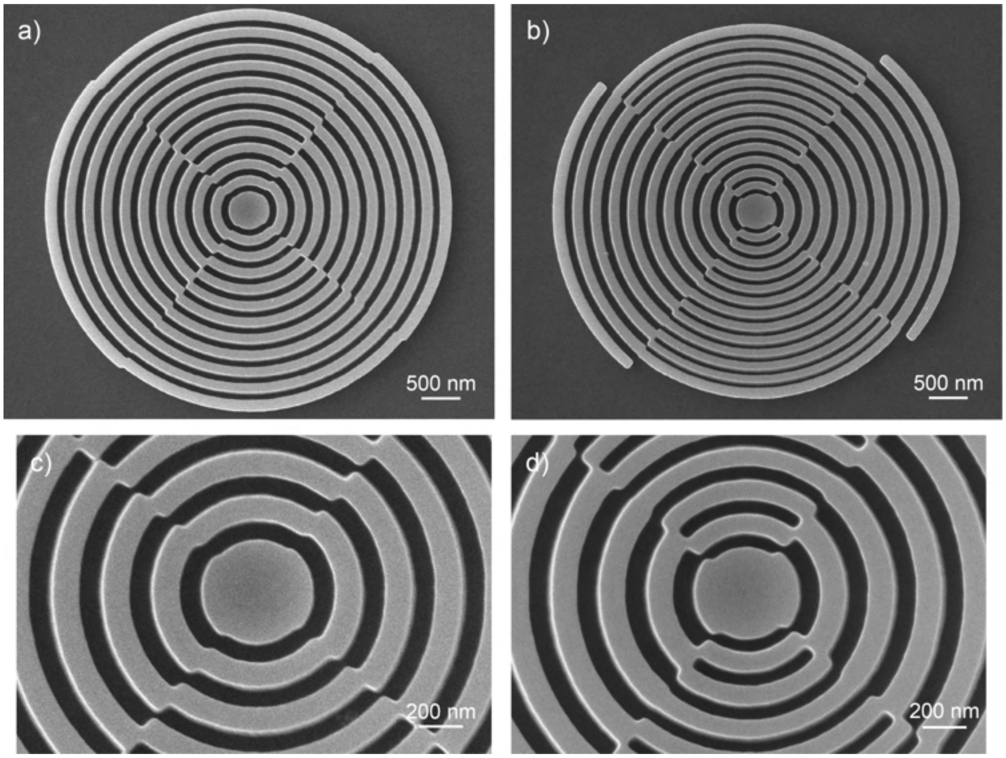

Figure 5.5 – Scanning electron microscopy (SEM) of dual resonance devices. (a,c) Device with parameters $(a_1, R_1) = (210, 226)$ nm, $(a_2, R_2) = (235, 250)$ nm and $\theta_1 = \theta_2 = 90°$. (b, d) Device with parameters $(a_1, R_1) = (179, 212)$ nm, $(a_2, R_2) = (235, 250)$ nm and $\theta_1 = \theta_2 = 90°$.

As discussed in previous work,[89] this process yields high-performance nanophotonic devices with minimal surface roughness on arbitrary substrates. It offers uniquely high integration capability because the substrate underlying the resonators is never exposed to plasma etching, and the ALD step can be performed on virtually any substrate, including two-dimensional materials which lack out-of-plane bonds [29]. To match our simulations and to demonstrate the devices' performance when interfaced with thin films, we fabricated devices on 50 nm TiO_2 films which were grown on fused silica using the same ALD process as the resonators themselves.

The scanning electron microscope (SEM) images in Figure 5.5 show the fabricated dual resonance devices. Different combinations of grating period and disc radius can yield qualitatively different geometries, which can be seen by comparing Figure 5.5c Figure 5.5d. Because our fabrication approach is ambivalent to the device geometry, and because the critical dimensions of these devices are well above the electron beam writing resolution, we do not detect any degradation of fabrication outcomes as the structure geometry varies.

5.4 Polarized reflection spectroscopy

5.4.1 Experimental apparatus

We used a home-built confocal microscopy apparatus to probe the resonances of the multi-resonant devices with reflection spectroscopy. A supercontiunuum source (YSL Photonics) was focused onto the sample by an objective lens and aligned to each device using voltage-controlled galvanometer mirrors. Reflected light was collected into a spectrometer and CCD detector (300 g/mm, Princeton Instruments). A linear polarizer plus half-wave plate were used to rotate the polarization of the excitation laser. In our experiments, we measured devices which exhibit resonances in the 700-900 nm range, as this wavelength range overlaps high intensity output from the supercontinuum source and high quantum efficiency of the CCD detector used in the experiments. Because TiO_2 has a relatively large bandgap (≈ 3.3 eV) and high index through the visible and IR ($n > 2.3$ at 1550 nm),[89] these devices can also be extended to further wavelength ranges.

5.4.2 Dual resonance device spectroscopy

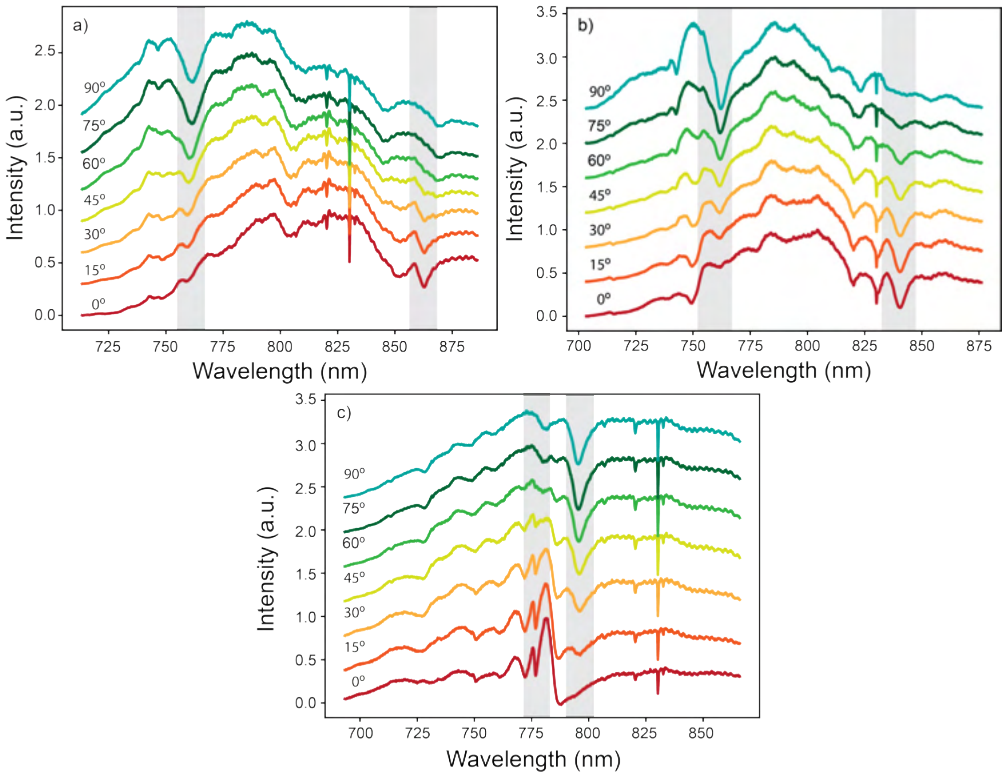

Figure 5.6 – Polarized reflection spectroscopy of dual resonant devices. (a-c) Reflected spectra versus beam polarization for devices with varying combinations of resonances. The data are not background subtracted, and the sharp feature near 830 nm is due to the supercontinuum source spectrum. For each device measured, $\theta_1 = \theta_2 = 90°$.

The bullseye antenna resonances appear as asymmetric Fano lineshapes in reflection spectroscopy due to the interference of the resonator mode(s) with reflection from the underlying thin film and substrate. As shown in Figure 5.6, for dual resonance devices, we detect multiple resonances on top of the supercontinuum source background that vary in intensity as the excitation polarization is rotated. We note that the sharp feature near 830 nm that appears in all spectra is an artifact from the supercontinuum generation and is unrelated to the antenna devices. The three plots in Figure 5.6 correspond to three different devices with varying grating periods and disc radii, which yield different combinations of resonance wavelengths. As the beam polarization is varied in 15° increments from 0 to 90°, one resonance in each device becomes less intense while the other grows more intense. Comparing the spectra when the excitation beam is polarized at 0° and 90°, the polarization selectivity of each resonance is clear, and the features of these spectra agree with predictions from simulations. By fitting the resonance features to Fano lineshapes, we extracted quality factors in the range 85-205, which are also in accordance with our simulated devices.

5.4.3 Triple resonance devices

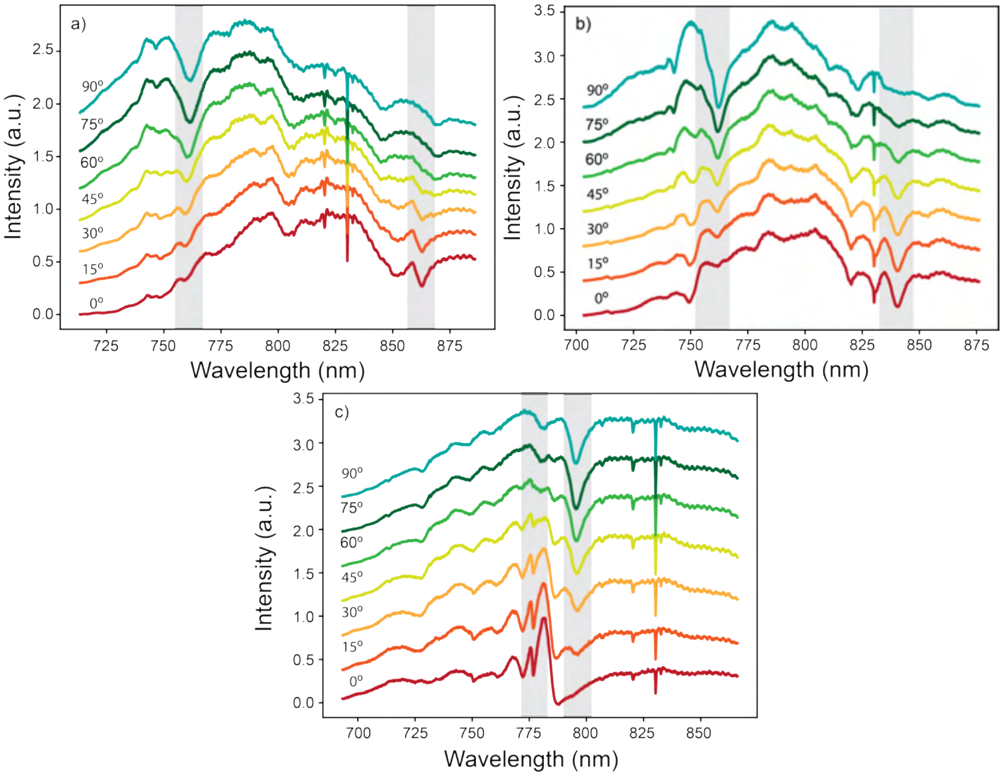

Figure 5.7 – Triple resonance devices. (a) Simulated beam intensity at z = -25 nm as a function of polarization for a device with three resonances and $\theta_1 = \theta_2 = \theta_3 = 60°$. (b, c) SEM images of a fabricated triple resonance device. (d) Reflection spectroscopy versus beam polarization for a triple resonance device with $\theta_1 = \theta_2 = \theta_3 = 60°$.

Because circular Bragg resonators are rotationally symmetric, we can extend the features of dual resonance devices to devices with a larger number of resonances. To demonstrate this principle, we simulated, fabricated, and measured the reflection response of triple resonance devices. To generate a third polarization-selective resonance, we simply segment the bullseye into three, introducing a third set of grating period, central disc radius, and subtended angle parameters (a_3, R_3, θ_3).

Figure 5.7a shows the simulated electric field intensity underneath a three-resonance device as a function of incident beam polarization. In principle, the three resonances should be maximized at 0°, 60°, and 120°, respectively. However, crosstalk between the resonances skews these values slightly, which can be seen in the polar plot. The SEM images in Figure 5.7b,c indicate that our ALD-based fabrication method can readily produce devices with three or more resonances, as we do not see any defects in the TiO_2 structure. Finally, reflection spectroscopy of triple resonance devices demonstrates that we can generate three polarization-selective resonances in one structure. For the device measured in Figure 5.7d, the three resonances vary in intensity as the excitation beam polarization is rotated fully from 0° to 180°. The resonances are nominally maximized at 0°, 60°, and 120°, as anticipated.

5.5 Conclusions

We have shown all-dielectric, multi-resonant CBR devices that combine wavelength and polarization multiplexing with the ability to efficiently direct underlying dipole emission into collection optics. The nanofabrication approach used to generate these devices offers high integration capability, making them compatible with a range of quantum and low-dimensional materials for applications in sensing and nonlinear frequency generation.[212–214] In other applications, multi-resonant CBRs may find use as ultracompact polarimeters[215] or polarization-tunable transmissive color filters.[216]

Chapter 6

Engineering Exciton Lifetimes with Off-Resonant Planar Cavities

ABSTRACT

Two-dimensional transition metal dichalcogenides have recently attracted interest as a basis to explore many-body physics such as Bose-Einstein condensation and other quantum coherence phenomena. However, these exotic states generally require thermal equilibrium, which is difficult to produce given the extremely short optical lifetimes of exciton and trion states in 2D TMDs. Increasing the excited state lifetime of these species by suppressing their emission rates can potentially unlock new avenues of research into their many-body interactions. In this chapter, we explore a method of increasing the optical lifetimes of direct excitons and trions in monolayer TMDs by embedding them in off-resonant planar cavities. We present simulated emission cutoff results, sample fabrication procedures, and intial data demonstrating extended emitter lifetimes. We then discuss potential avenues to improve these results through novel sample fabrication processes.

6.1 Introduction

In addition to their application in optoelectronic devices, two-dimensional transition metal dichalcogenides (2D TMDs) have attracted growing interest as a platform to study many-body physics and quantum phases of matter.[73,206,217–223] Excitons in these materials serve as bosonic quasi-particles which can participate in many-body interactions at high densities. Due to their large binding energies, Bose Einstein condensation (BEC) of excitons in 2D TMDs is predicted at higher temperatures than in quasi-2D quantum wells.[206] However, excitonic condensation is hindered by the short lifetime of optical excitations in monolayer

TMDs,[224] which prevents the development of thermodynamic equilibrium for condensates. Increasing exciton lifetimes by suppressing radiative recombination is therefore necessary to observe coherence phenomena in these materials. Longer exciton lifetimes would also lead to longer diffusion lengths, which can enable devices based on long-range exciton transport.[225,226] This possibility is especially interesting for 2D TMDs, which exhibit spin-valley locking and can therefore support spin-polarized exciton fluxes.[55,72] Moreover, extending exciton lifetimes beyond electronic timescales ($\approx$ ns) could allow dynamic electronic control within the excited state lifetime for applications in photon storage.

Interlayer excitons, in which the electron and hole reside in two different TMD monolayers stacked on top of one another, have demonstrated the longest lifetimes in these materials to date.[69,206,217,221,223] These heterostructure systems support excitons with up to microsecond lifetimes and are a promising platform for explorations of Bose-Einstein condensation, superfluidity, and other many-body effects.[206,217,221] However, generating interlayer coupling between two distinct monolayers requires precise control of interlayer separation and twist angle, which impact the electron-hole wavefunction overlap.[69] Moiré potentials, formed from the heterostructure superlattice, can further complicate exciton dynamics by imposing additional optical selection rules and can impede long-range transport in exitonic devices.[227]

In this work, we aimed to generate long-lived, direct excitons in a single monolayer of $MoSe_2$ by embedding it in an off-resonant optical cavity. For optical excitations with in-plane dipole moments, the planar cavity suppresses emission at wavelengths longer than a cut-off determined by the cavity size,[228] as discussed in Chapter 1. We investigated the impact of the off-resonant cavity environment on exciton dynamics by probing the photoluminescence linewidth, reflectivity linewidth, and photoluminescence lifetime of excitons and trions in $MoSe_2$.

6.2 Simulations of emission suppression

To determine the geometric parameters of a planar cavity capable of supppressing exciton emission, we used finite difference time domain software (Lumerical FDTD) to simulate a range of metal-insulator-metal heterostructures. In all simulations, we considered the behavior of an in-plane dipole emitter at the center of the layered structure (z = 0 nm). Immediately surrounding this dipole source we input a layer of material with refractive index n = 2.12, chosen to approximate the encapsulating hexagonal boron nitride (hBN) around the 2D TMD. Above and below this central heterostructure we added dielectric layers, the refractive indices of which were varied to approximate different oxide or polymer materials. Underneath, we simulated a single crystal silver substrate using ellipsometry data from previous work.[120] Finally, the top layer of the structure was formed by a thin (< 50 nm) polycrystalline silver layer, which was input using pre-loaded optical parameters from the Johnson and Christy reference dataset.

Because excitons in 2D TMDs are fundamentally delocalized excitations with center-of-mass momentum, it is not obvious that their optical emission should be well approximated by a point dipole source. To verify the accuracy of our FDTD simulations, we considered the impact of these uniquely excitonic features on spontaneous emission near metal interfaces and cavities, as detailed in Ref. [229]. In these calculations, the exciton was modelled as a planar dipole source, a current density distributed across a 2D plane. While there are some regimes, particularly at extremely low temperatures, where exciton emission behavior would diverge from that of point dipoles in a planar metal cavity, we confirmed that the point dipole approximation is valid for 2D excitons at 4K.[229]

The primary figure of merit we considered when designing an emission-suppressing planar cavity for excitons in $MoSe_2$ was the Purcell factor in the wavelength range 750-770 nm, which corresponds to $MoSe_2$ exciton and trion emission. Typically, without electrical gating, we observe more intense photoluminescence from $MoSe_2$ monolayers at the trion emission wavelength ($\approx$ 770 nm) than at the exciton emission wavelength ($\approx$ 750 nm), which suggests slight intrinsic n doping. Because PL is the most readily accessible experimental metric for this work and because trion lifetimes tend to be longer than exciton lifetimes, we optimized our devices for 770 nm operation.

We explored a range of dielectric materials as spacer layers in the off-resonant cavity, including SiO_2, Al_2O_3, PMMA, and hBN. Overall, when considering parallel dipole emission, materials with lower refractive index, like SiO_2 (n $\approx$ 1.45) and PMMA (n $\approx$ 1.48) yielded the lowest Purcell factors in simulations. In the most extreme case, we calculated a Purcell factor of 0.03 for 770 nm dipole emission in a silver-SiO_2-silver cavity, which represents a greater than 30-fold emission suppression. We interpret these results as evidence that the parallel dipole is best isolated from nonradiative emission into plasmonic oscillations in the silver layers when the surrounding dielectric has a low index. However, other optical and mechanical properties of the dielectric medium and its integration capability are not fully captured by simulations. For example, SiO_2 deposited with e-beam deposition often includes charge traps, and PMMA is not compatible with our heterostructure dry transfer process (Chapter 1) because it dissolves in chloroform. We therefore chose to explore a silver-hBN-silver cavity in our initial experiments to avoid these potential issues and simplify fabrication.

Figure 6.1 illustrates a set of simulation results for a silver-hBN-silver cavity with varying hBN and top silver layer thicknesses. The Purcell factor at 770 nm is displayed as a function of these layer thicknesses. Reading a row in Figure 6.1 from left to right, the lowest Purcell factor values occur when the hBN layer is 80-100 nm thick. With a thinner dielectric, nonradiative emission into the metal increases. If the dielectric layer becomes too thick, meanwhile, the cavity can support an optical mode and then enhance ($F_P > 1$) rather than suppress the dipole emission. Looking from the top of a column downwards, we can see that a thicker top silver layer generally results in greater destructive interference and emission suppression at the cavity center. However, it is important to note that there is a tradeoff between this suppression effect and our ability to probe the device experimentally, as when the top silver layer becomes thick (several skin depths), less far field light will be transmitted to the material we aim to optically probe. The boxes outlined in red represent the geometrical parameters we targeted during our sample fabrication, which were simulated to yield a Purcell factor of 0.09 at 770 nm.

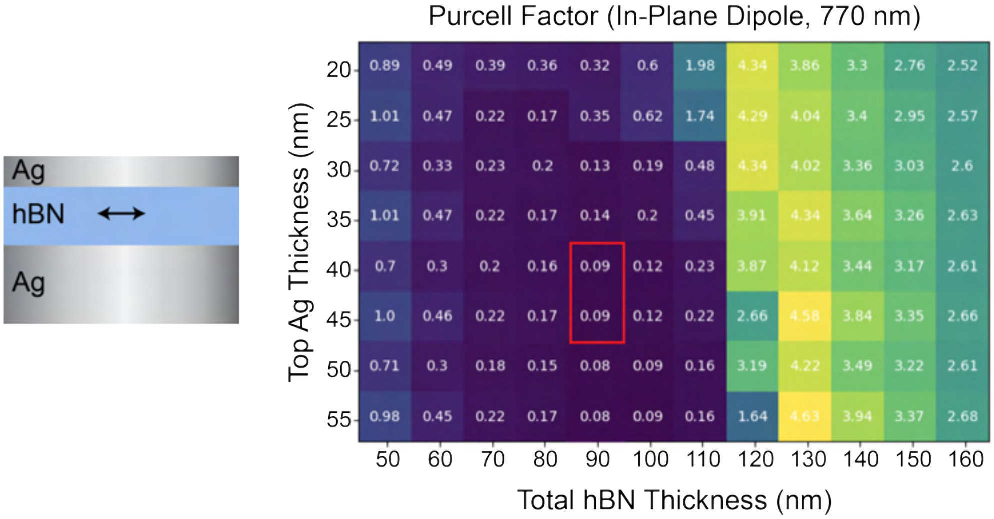

Figure 6.1 – Simulated suppression of trion emission in $MoSe_2$ by a planar cavity. (Left) Schematic of the metal-insulator-metal structure used in simulations. The total hBN thickness and the thickness of the top silver layer were both varied linearly. (Right) Purcell factor at 770 nm wavelength for an in-plane dipole source located at the center of the cavity as a function of total hBN thickness and top silver thickness. The region outlined in red represents the parameters targeted during sample fabrication.

6.3 Sample fabrication

To fabricate the optimized metal-insulator-metal structure, we began by depositing single crystal silver via eptiaxy on cleaved mica. Single crystal silver is desirable due to its lack of grain boundaries and because silver has a favorable (less lossy) plasmonic response in the visible wavelength range compared to other metals. To generate a single crystal film, the substrate must be heated to 300-350 C during deposition and the deposition rate must be extremely high, in the range 1.5-2.0 nm/s.[120,230] These parameters balance the dewetting of the silver film with agglomeration enabled by surface diffusion in order to yield a smooth final surface. In our process, we used thermal deposition of 99.999% silver at 350 C and a deposition rate of 1.7 nm/s in order to produce smooth 300 nm thick films. The results are shown in Figure 6.2a. Atomic force microscopy demonstrates a surface with sub-nm roughness (RMS ≈ 0.4 nm) and a triangular morphology which results from the [111] crystal plane of the silver epitaxy on mica.

Following substrate preparation, we transferred an hBN-MoSe$_2$-hBN heterostructure directly onto the silver surface. Figure 6.2b shows an optical microscope image of the heterostructure on the silver substrate. The thickness of the individual layers of this Van der Waals stack were determined in advance by AFM in order to ensure they matched the desired parameters from simulations. Each hBN flake was 45 ± 2 nm. The sample was cooled to 4K and an initial set of optical measurements was taken. Finally, the sample was returned to room temperature and a final silver top layer was deposited using thermal evaporation at a rate of 0.15 nm/s and no substrate heating. The deposition rate of this process was calibrated in advance so that the final deposition yielded a 50 nm thick film. The sample, pictured in Figure 6.3a, was then cooled to 4K again for a second set of measurements to which we compared the original data set and analyzed changes in emitter lifetime.

6.4 Experimental results

We probed the impact of the off-resonant planar cavity on the MoSe$_2$ exciton and trion lifetimes by measuring PL linewidths, reflectivity linewidths, and PL lifetimes before and after the final top silver layer was added to the device. Figure 6.3b shows a PL scan of the monolayer region after the device was completed. Comparing this image to Figure 6.2c, one can immediately see increased inhomogeneity in the intensity of the MoSe$_2$ excitonic response. In these scans, the material was probed with a 660 nm diode laser and PL from both exciton and trion peaks was collected using a long pass filter. This initial result,

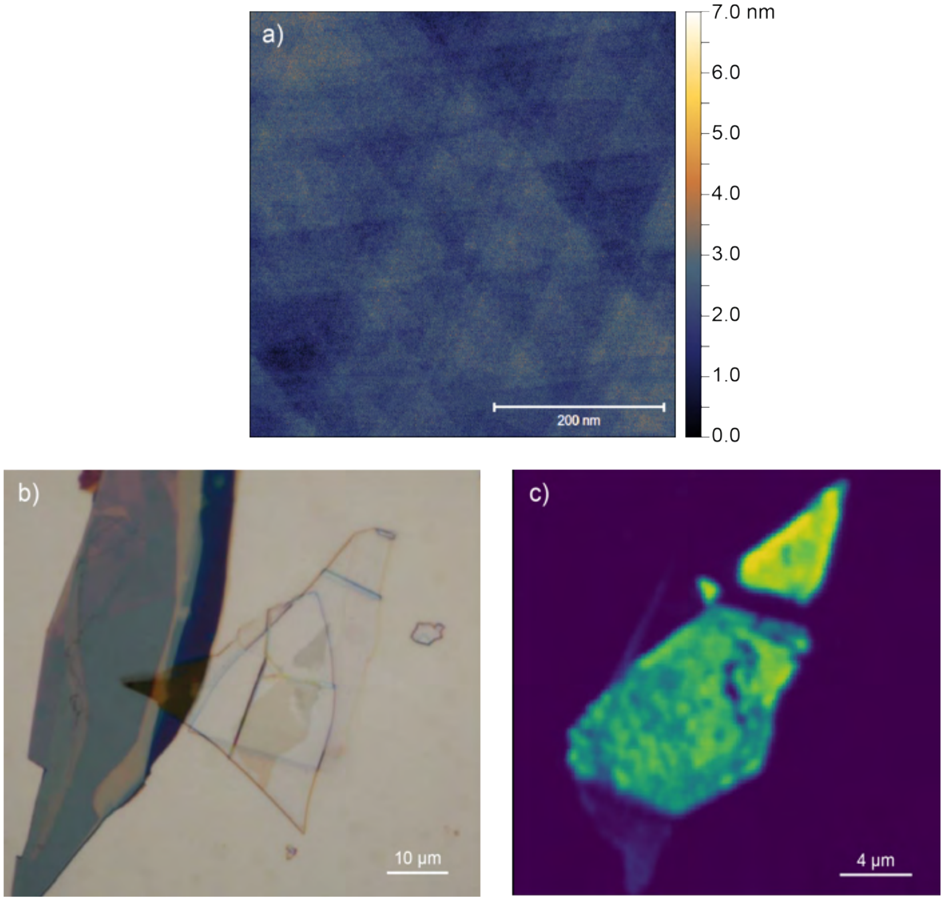

,

Figure 6.2 – Preparation of $MoSe_2$ heterostructure on single-crystal silver. (a) AFM scan of [111] single crystal silver epitaxy on cleaved mica with RMS roughness of 0.4 nm. (b) Optical microscope image of an hBN-$MoSe_2$-hBN heterostructured after transfer onto the silver substrate. (c) PL scan of the enacpsulated monolayer $MoSe_2$ using 660 nm laser excitation.

combined with the optical image in Figure 6.3a, qualitatively suggests that the addition of the top silver layer introduced disorder in the system, potentially including a varying local strain profile. AFM scans of the top silver layer show significant agglomeration and an RMS roughness of 10 nm. Additionally, PL spectra taken from over twenty locations on the $MoSe_2$ before and after the top silver deposition showed significant degradation of the material optical response in most areas. The only region of the monolayer which demonstrated two easily identifiable peaks, the exciton and trion features, after the top silver deposition was the separate triangular region at the top right of the 2D PL scans. We focused on this region in the rest of our experiments.

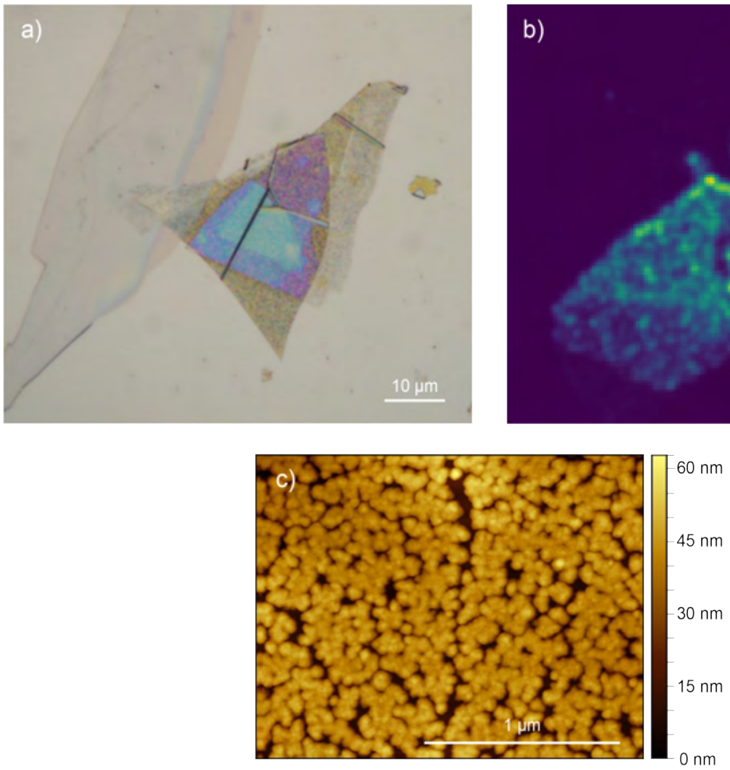

Figure 6.3 – $MoSe_2$ heterostructure in a metal-insulator-metal cavity. (a) Optical microscope image of the structure in Figure 6.2a after an additional 40 nm silver layer was deposited to complete the planar cavity. (b) PL scan of the enacpsulated monolayer $MoSe_2$ inside of the completed cavity using 660 nm laser excitation. (C) AFM scan of top silver layer demonstrating significant agglomeration and 10 nm RMS roughness.

To quantitatively assess the impact of the top silver layer, we first considered modifications to the PL linewidth of the exciton and trion peaks from ten locations within the top region of the monolayer. These results are displayed in Figure 6.4. We extracted linewidths by fitting Lorentzian peaks to each PL feature. For the exciton feature, half of the locations demonstrated narrowed linewidths, and half were broadened. With these results, we cannot make definitive conclusions about the impact of the off-resonant device on the exciton lifetime. The trion feature, however, showed linewidth narrowing in the majority of locations measured, which suggests increased trion lifetimes, as expected from simulations.

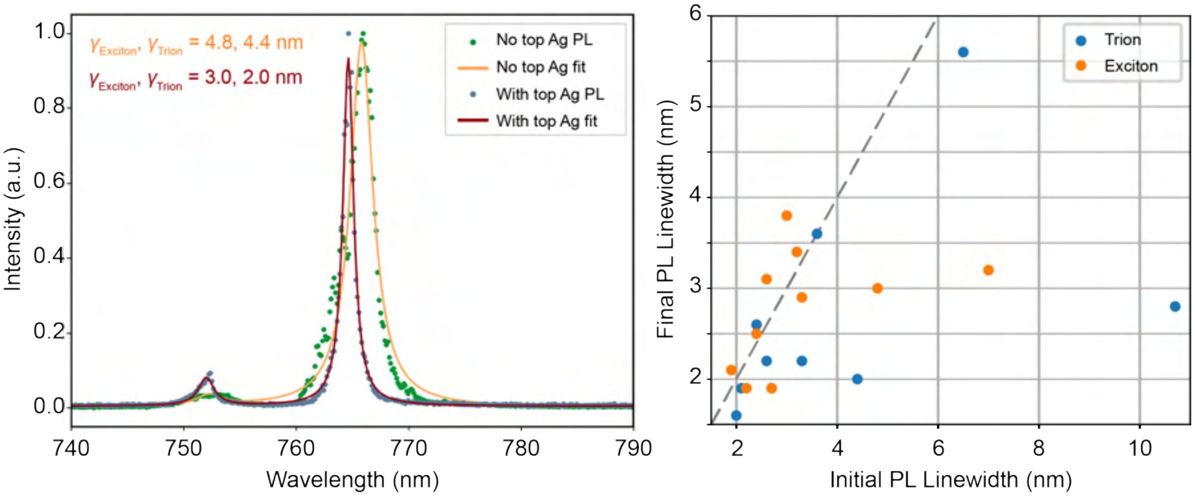

Figure 6.4 – MoSe$_2$ PL in a metal-insulator-metal cavity. (Left) Spectra before and after the top silver layer deposition at nominally the same location on the MoSe$_2$ sample. Exciton and trion peak linewidths were extracted from a double Lorentzian fit. (Right) Summary of PL linewidths at ten locations before and after the top silver layer was added. The dashed line represents $\gamma_{\text{Initial}} = \gamma_{\text{Final}}$.

We next compared the reflection spectra before and after the top silver layer was deposited. These spectra primarily feature the exciton response, which appears as an asymmetric Fano dip over the background signal.[61] Reflectivity resonantly probes the exciton optical oscillations, in contrast to non-resonant PL measurements which include nonradiative decay pathways. To collect this data, we filtered a white LED source with a long pass filter in order to prevent PL contributions and collected light reflected from the sample. We subtracted the background signal by referencing an area of the sample that included the full silver-hBN-silver stack without the monolayer $MoSe_2$ and normalized the result to the background level. Figure 6.5 displays the resulting spectra and a summary of linewidth changes. As the plot in Figure 6.5a shows, the magnitude of the reflectivity signal is reduced when the top silver layer is added, which is expected due to limited transmission through the film to the monolayer. The shape of the signal is also modified, as additional broadband reflections interfere with the exciton resonance. Overall, the linewidth of the exciton resonance was reduced in eight of the nine locations from which we gathered data (one of the previously measured points did not show a resonance feature). In some cases, the linewidth was reduced by nearly a factor of four. For reference, other studies demonstrating a factor of two change to exciton reflectivity linewidth claim an order of magnitude change in emitter lifetime.[80,81]

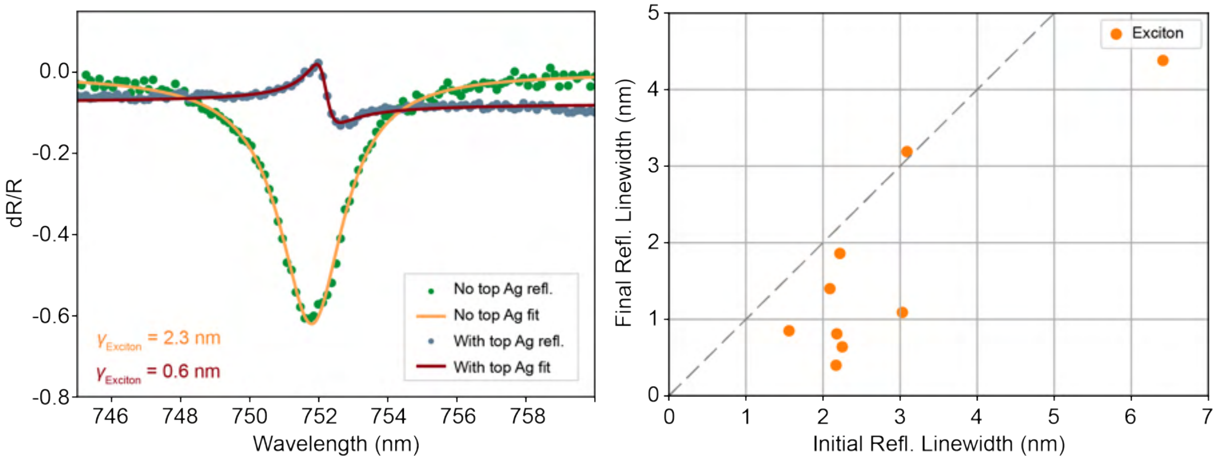

Figure 6.5 – $MoSe_2$ reflectivity in a metal-insulator-metal cavity. (Left) Spectra before and after the top silver layer deposition at nominally the same location on the $MoSe_2$ sample. Exciton peak linewidths were extracted from a Fano fit. (Right) Summary of reflectivity linewidths at nine locations before and after the top silver layer was added. The dashed line represents $\gamma_{\text{Initial}} = \gamma_{\text{Final}}$.

The third dataset we compared was the time-domain PL decay of the exciton and trion features. For these measurements, we fiber-coupled a pulsed laser source (Mira) with 728 nm center wavelength and approximately 200 fs pulse width. While we did not measure the pulse width after the source propagated through the optical fiber, it is unlikely that broadening would impact the experimental results due to the limited time resolution of our measurement. The resolution was determined by the avalanche photodetector (APD) used for time-domain collection, which was ≈ 35 ps (MPD). This APD was connected via an NIM electrical signal to a single photon counting module which time tagged each incoming photon from the $MoSe_2$ PL. In the lifetime experiments, we separately considered the excition and trion emission by using narrowband bandpass filters on the collection channel (750 ± 5 nm and 766 ± 6 nm, Semrock).

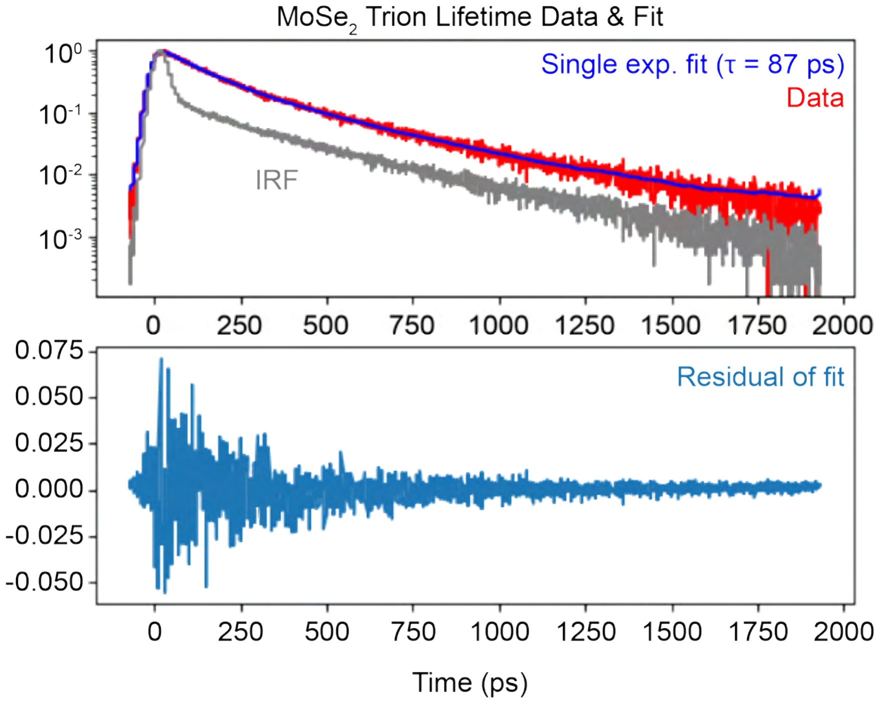

Figure 6.6 – Photoluminescence lifetime deconvolution. (Top) Instrument response function (IRF, grey), trion PL decay data (red), and fit to a single exponential decay convolved with the measured IRF (blue). The extracted PL lifetime for this dataset was 87 ps. (Bottom) Residuals of the fit displayed in the upper plot.

Interpreting the lifetime data extracted in these experiments requires deconvolving the instrument response function (IRF) of the apparatus from the PL decay. The IRF is a result of the nonlinear response of the detector to the pulsed laser signal. The grey curve plotted in Figure 6.6 represents the IRF in our experiment, which was obtained by recording the pulsed laser signal reflected from a region on the silver-hBN sample away from the $MoSe_2$ monolayer. A sharp Gaussian peak convolved with a slowly decaying tail is characteristic of fast-response silicon APDs. The tail is a result of photoexcited charge carriers diffusing into the active region of the device after the initial excitation. PL decay can be modelled as a single or multi-exponential function which is convolved with this IRF. To extract decay time constants, we iterate a curve fitting algorithm that convolves an exponential decay function with the experimentally obtained IRF, compares the output to the PL dataset, and then iterates the exponential parameters until the fit is optimized. An example of the results of this fitting procedure is shown in Figure 6.6.

With the resolution afforded by our experimental apparatus, we are unable to probe exciton PL decay in the time domain. Trion PL decay, however, can be clearly discriminated from the background IRF, as shown in Figure 6.7. By fitting these curves using the procedure previously described, we successfully detected increased trion PL decay constants, indicating extended optical lifetimes. In the regions corresponding to the three plots in Figure 6.7, the trion decay was extended by up to a factor of 2.5. Furthermore, the regions in which the decay tiem constant was increased generally corresponded to the regions that displayed narrowed trion PL linewidths, as predicted.

6.5 Conclusion and Outlook

Taken as a whole, the PL spectroscopy, reflection spectroscopy, and PL time-domain measurements in this work indicate the successful application of an off-resonant planar cavity to extend exciton lifetimes. We demonstrated modifications to the lifetimes of exciton species in monolayer $MoSe_2$ by embedding the material in a silver-hBN-silver cavity. In some regions of the $MoSe_2$ sample, we observed PL and reflectivity linewidth narrowing of the excitonic features and an increase in PL decay times, which are consistent with FDTD simulations. However, our results are complicated by fabrication inhomogeneities which degraded the optical response from a large portion of the $MoSe_2$ sample and may independently lead to changes in the emitter lifetimes due to the presence of strain or the diffusion of metal atoms

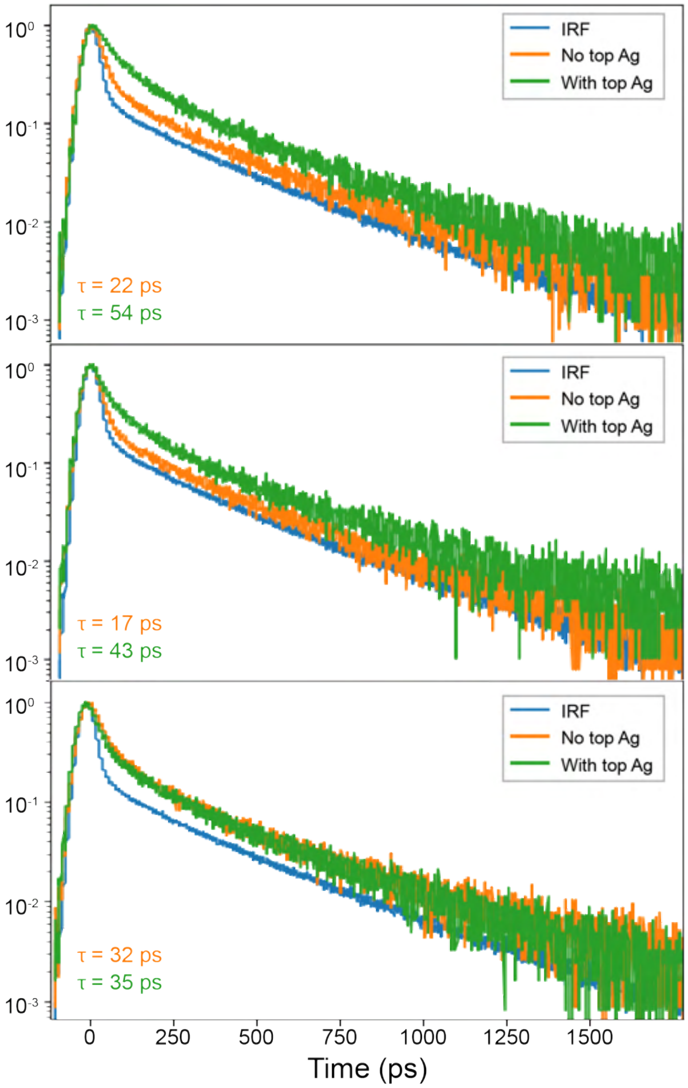

Figure 6.7 – $MoSe_2$ trion lifetime on silver versus in an off-resonant cavity. Each plot corresponds to a different location on the sample. Extracted lifetimes from fitting a single exponential convolved with the IRF are labelled.

into the hBN in close proximity to the 2D TMD. Improving the fabrication procedure used in this work will clarify the impact of the off-resonant cavity geometry on exciton lifetimes and may yield more dramatic emission suppression. One promising integration approach is the transfer of pre-deposited metal films directly onto Van der Waals heterostructures in place of metal deposition through evaporation or sputtering. Several techniques to pattern, strip, and transfer metal films onto 2D materials have recently been explored[231,232] and will likely improve interfaces between metals and van der Waals materials in future nanophotonic engineering applications.

Chapter 7

Summary and Outlook

The body of work presented in this dissertation demonstrates the importance of flexible nanofabrication processes for building light-matter interfaces. As discussed in the introductory chapters, engineering optical environments on the nanoscale allows us to manipulate the rate, spatial distribution, and spectral distribution of light emission for a range of quantum and classical optoelectronic applications. In Chapter 3, we introduced a platform for nanophotonic device fabrication that uses templated atomic layer deposition of TiO_2 to build integrated photonics without damaging underlying substrates. We delved into the most critical elements of this process, the electron beam lithography and TiO_2 deposition, and provided insights into their most essential variables. Then, Chapter 4 detailed two applications of this platform to quantum materials. In the first, photonic crystal cavities were integrated with diamond membranes for spin-photon interfacing with color centers. In the second, an integrated waveguide was used to generate an electrically controllable chiral optical interface with a 2D semiconductor. Both of these applications are dependent on the high quality and integration capability of the ALD TiO_2 fabrication platform, which can efficiently couple light to sensitive underlying materials. Chapter 5 further showed the flexibility of this approach by extending it to a novel device geometry, azimuthally segmented bullseye antennas, which enable both wavelength and polarization multiplexing in a single nanoscale volume.

The work presented in Chapter 6 is disparate from the others in that it explored metal rather than dielectric nanostructures and was aimed at suppressing rather than enhancing spontaneous emission. By embedding a 2D semiconductor in a silver-insulator-silver planar heterostructure, we successfully observed signatures of increased exciton and trion lifetimes. Fabrication inhomogeneities, however, complicated these results. Difficulties depositing high quality films on Van der Waals materials restricted the materials available in our device and degraded the exciton response in a large portion of our sample. These experiments only further underline the importance of flexible nanofabrication methods for hybrid material integration.

Future work leveraging the approaches introduced in this thesis will require careful consideration of process parameters. Although the TiO_2 ALD process presented here is highly reproducible, certain aspects, such as the e-beam lithography parameters, are critically dependent on template geometry and should be re-optimized for new applications. A set of fabrication recipes essential to the work in this thesis can be found in the appendix and may serve as a useful starting point for future projects. Understanding the physical mechanisms at play during each process step is the best approach to troubleshooting and for identifying the root cause of process issues when they inevitably arise. We believe that the uniquely high integration capability and broad wavelength operation of the TiO_2 ALD platform will make it an important asset to future nanophotonic engineering with quantum materials.

REFERENCES

(1) Novotny, L.; Hecht, B., *Principles of Nano-Optics*; Cambridge University Press: 2006.

(2) Purcell, E. M. Resonance Absorption by Nuclear Magnetic Moments in a Solid. *Phys. Rev.* **1946**, *69*.

(3) Weisskopf, V.; Wigner, E. Berechnung der natürlichen Linienbreite auf Grund der Diracschen Lichttheorie. *Zeitschrift für Physik* **1930**, *63*, 54–73.

(4) Pelton, M. Modified spontaneous emission in nanophotonic structures. *Nature Photonics* **2015**, *9*, 427–435.

(5) Haroche, S.; Raimond, J. M., *Exploring the Quantum: Atoms, Cavities, and Photons*; Oxford Univ. Press: Oxford, 2006.

(6) Ashkin, A. Optical trapping and manipulation of small neutral particles using lasers. *Proceedings of the National Academy of Sciences* **2010**, *94*, 4853–4860.

(7) Wolfowicz, G.; Heremans, F. J.; Anderson, C. P.; Kanai, S.; Seo, H.; Gali, A.; Galli, G.; Awschalom, D. D. Quantum guidelines for solid-state spin defects. *Nature Reviews Materials* **2021**, *6*, 906–925.

(8) Noda, S.; Kitamura, K.; Okino, T.; Yasuda, D.; Tanaka, Y. Photonic-crystal surface-emitting lasers: Review and introduction of modulated-photonic crystals. *IEEE Journal of Selected Topics in Quantum Electronics* **2017**, *23*, DOI: `10.1109/JSTQE.2017.2696883`.

(9) Krasnok, A.; Lepeshov, S.; Alú, A. Nanophotonics with 2D transition metal dichalcogenides [Invited]. *Optics Express* **2018**, *26*, 15972.

(10) Vollmer, F.; Yang, L.; Fainman, S. Label-free detection with high-Q microcavities: A review of biosensing mechanisms for integrated devices. *Nanophotonics* **2012**, *1*, 267–291.

(11) Schröder, T.; Mouradian, S. L.; Zheng, J.; Trusheim, M. E.; Walsh, M.; Chen, E. H.; Li, L.; Bayn, I.; Englund, D. Quantum nanophotonics in diamond [Invited]. *Journal of the Optical Society of America B* **2016**, *33*, B65.

(12) Bradac, C.; Gao, W.; Forneris, J.; Trusheim, M. E.; Aharonovich, I. Quantum nanophotonics with group IV defects in diamond. *Nature Communications* **2019**, *10*, 5625.

(13) Zhong, T.; Goldner, P. Emerging rare-earth doped material platforms for quantum nanophotonics. *Nanophotonics* **2019**, *8*, 2003–2015.

(14) Fox, M., *Quantum optics: an introduction*; Oxford master series in atomic, optical, and laser physics; Oxford Univ. Press: Oxford, 2006.

(15) Drexhage, K. H. Influence of a dielectric interface on fluorescence decay time. *Journal of Luminescence* **1970**, *1-2*, 693–701.

(16) Chen, B.; He, Z.; Liu, Z. J.; Wang, Y. K.; Gao, Y. N.; Aharonovich, I.; Xu, Z. Q.; Liu, J. Simultaneously enhanced linear and nonlinear photon generations from WS2by using dielectric circular Bragg resonators. *Nanophotonics* **2020**, *9*, 2587–2592.

(17) Jhe, W.; Anderson, A.; Hinds, E. A.; Meschede, D.; Moi, L.; Haroche, S. Suppression of spontaneous decay at optical frequencies: Test of vacuum-field anisotropy in confined space. *Phys. Rev. Lett.* **1987**, *58*, 666–669.

(18) Markos, P.; Soukoulis, C. M., *Wave Propagation: From Electrons to Photonic Crystals and Left-Handed Materials*; Princeton University Press: 2008, pp 1–376.

(19) Harrow, A. W.; Montanaro, A. Quantum computational supremacy. *Nature* **2017**, *549*, 203–209.

(20) Georgescu, I. M.; Ashhab, S.; Nori, F. Quantum simulation. *Reviews of Modern Physics* **2014**, *86*, 153–185.

(21) Degen, C. L.; Reinhard, F.; Cappellaro, P. Quantum sensing. *Reviews of Modern Physics* **2017**, *89*, 1–39.

(22) Gisin, N.; Thew, R. Quantum communication. *Nature Photonics* **2007**, *1*, 165–171.

(23) Kimble, H. J. The quantum internet. *Nature* **2008**, *453*, 1023–1030.

(24) Wehner, S.; Elkouss, D.; Hanson, R. Quantum internet: A vision for the road ahead. *Science* **2018**, *362*.

(25) Northup, T. E.; Blatt, R. Quantum information transfer using photons. *Nature Photonics* **2014**, *8*, 356–363.

(26) Gobby, C.; Yuan, Z. L.; Shields, A. J. Quantum key distribution over 122 km of standard telecom fiber. *Applied Physics Letters* **2004**, *84*, 3762–3764.

(27) Hensen, B. et al. Loophole-free Bell inequality violation using electron spins separated by 1.3 kilometres. *Nature* **2015**, *526*, 682–686.

(28) Cirac, J. I.; Zoller, P.; Kimble, H. J.; Mabuchi, H. Quantum State Transfer and Entanglement Distribution among Distant Nodes in a Quantum Network. *Physical Review Letters* **1997**, *78*, 3221–3224.

(29) Duan, L.-M.; Kimble, H. J. Scalable Photonic Quantum Computation through Cavity-Assisted Interactions. *Physical Review Letters* **2004**, *92*, 127902.

(30) Tiecke, T. G.; Thompson, J. D.; De Leon, N. P.; Liu, L. R.; Vuletić, V.; Lukin, M. D. Nanophotonic quantum phase switch with a single atom. *Nature* **2014**, *508*, 241–244.

(31) Ritter, S.; Nölleke, C.; Hahn, C.; Reiserer, A.; Neuzner, A.; Uphoff, M.; Mücke, M.; Figueroa, E.; Bochmann, J.; Rempe, G. An elementary quantum network of single atoms in optical cavities. *Nature* **2012**, *484*, 195–200.

(32) Reiserer, A.; Rempe, G. Cavity-based quantum networks with single atoms and optical photons. *Reviews of Modern Physics* **2015**, *87*, 1379–1418.

(33) Aharonovich, I.; Englund, D.; Toth, M. Solid-state single-photon emitters. *Nature Photonics* **2016**, *10*, 631–641.

(34) Weber, J. R.; Koehl, W. F.; Varley, J. B.; Janotti, A.; Buckley, B. B.; Van De Walle, C. G.; Awschalom, D. D. Quantum computing with defects. *Proceedings of the National Academy of Sciences* **2010**, *107*, 8513–8518.

(35) Sipahigil, A. et al. An integrated diamond nanophotonics platform for quantum-optical networks. *Science* **2016**, *354*, 847–850.

(36) Doherty, M. W.; Manson, N. B.; Delaney, P.; Jelezko, F.; Wrachtrup, J.; Hollenberg, L. C. The nitrogen-vacancy colour centre in diamond. *Physics Reports* **2013**, *528*, 1–45.

(37) Rondin, L.; Tetienne, J. P.; Hingant, T.; Roch, J. F.; Maletinsky, P.; Jacques, V. Magnetometry with nitrogen-vacancy defects in diamond. *Reports on Progress in Physics* **2014**, *77*, DOI: `10.1088/0034-4885/77/5/056503`.

(38) Toyli, D. M.; De Las Casas, C. F.; Christle, D. J.; Dobrovitski, V. V.; Awschalom, D. D. Fluorescence thermometry enhanced by the quantum coherence of single spins in diamond. *Proceedings of the National Academy of Sciences of the United States of America* **2013**, *110*, 8417–8421.

(39) Faraon, A.; Santori, C.; Huang, Z.; Acosta, V. M.; Beausoleil, R. G. Coupling of nitrogen-vacancy centers to photonic crystal cavities in monocrystalline diamond. *Physical Review Letters* **2012**, *109*, 2–6.

(40) Wolters, J.; Sadzak, N.; Schell, A. W.; Schröder, T.; Benson, O. Measurement of the ultrafast spectral diffusion of the optical transition of nitrogen vacancy centers in nano-size diamond using correlation interferometry. *Physical Review Letters* **2013**, *110*, 1–5.

(41) Palyanov, Y. N.; Kupriyanov, I. N.; Borzdov, Y. M.; Surovtsev, N. V. Germanium: A new catalyst for diamond synthesis and a new optically active impurity in diamond. *Scientific Reports* **2015**, *5*, 1–8.

(42) Iwasaki, T. et al. Germanium-Vacancy Single Color Centers in Diamond. *Scientific Reports* **2015**, *5*, 1–7.

(43) Sipahigil, A.; Jahnke, K. D.; Rogers, L. J.; Teraji, T.; Isoya, J.; Zibrov, A. S.; Jelezko, F.; Lukin, M. D. Indistinguishable photons from separated silicon-vacancy centers in diamond. *Physical Review Letters* **2014**, *113*, 1–5.

(44) Gali, A.; Maze, J. R. Ab initio study of the split silicon-vacancy defect in diamond: Electronic structure and related properties. *Phys. Rev. B* **2013**, *88*, 235205.

(45) Iwasaki, T.; Miyamoto, Y.; Taniguchi, T.; Siyushev, P.; Metsch, M. H.; Jelezko, F.; Hatano, M. Tin-Vacancy Quantum Emitters in Diamond. *Physical Review Letters* **2017**, *119*, 1–6.

(46) Tchernij, S. D.; Herzig, T.; Forneris, J.; Küpper, J.; Pezzagna, S.; Traina, P.; Moreva, E.; Degiovanni, I. P.; Brida, G.; Skukan, N.; Genovese, M.; Jakšić, M.; Meijer, J.; Olivero, P. Single-Photon-Emitting Optical Centers in Diamond Fabricated upon Sn Implantation. *ACS Photonics* **2017**, *4*, 2580–2586.

(47) Ditalia Tchernij, S et al. Single-Photon Emitters in Lead-Implanted Single-Crystal Diamond. *ACS Photonics* **2018**, *5*, 4864–4871.

(48) Trusheim, M. E.; Wan, N. H.; Chen, K. C.; Ciccarino, C. J.; Flick, J.; Sundararaman, R.; Malladi, G.; Bersin, E.; Walsh, M.; Lienhard, B.; Bakhru, H.; Narang, P.; Englund, D. Lead-related quantum emitters in diamond. *Phys. Rev. B* **2019**, *99*, 075430.

(49) Siyushev, P. et al. Optical and microwave control of germanium-vacancy center spins in diamond. *Physical Review B* **2017**, *96*, 081201.

(50) Evans, R. E.; Sipahigil, A.; Sukachev, D. D.; Zibrov, A. S.; Lukin, M. D. Narrow-Linewidth Homogeneous Optical Emitters in Diamond Nanostructures via Silicon Ion Implantation. *Physical Review Applied* **2016**, *5*, 1–8.

(51) Bhaskar, M. K.; Sukachev, D. D.; Sipahigil, A.; Evans, R. E.; Burek, M. J.; Nguyen, C. T.; Rogers, L. J.; Siyushev, P.; Metsch, M. H.; Park, H.; Jelezko, F.; Lončar, M.; Lukin, M. D. Quantum Nonlinear Optics with a Germanium-Vacancy Color Center in a Nanoscale Diamond Waveguide. *Physical Review Letters* **2017**.

(52) Bray, K.; Regan, B.; Trycz, A.; Previdi, R.; Seniutinas, G.; Ganesan, K.; Kianinia, M.; Kim, S.; Aharonovich, I. Single Crystal Diamond Membranes and Photonic Resonators Containing Germanium Vacancy Color Centers. *ACS Photonics* **2018**, *5*, 4817–4822.

(53) Guo, X.; Delegan, N.; Karsch, J. C.; Li, Z.; Liu, T.; Shreiner, R.; Butcher, A.; Awschalom, D. D.; Heremans, F. J.; High, A. A. Tunable and Transferable Diamond Membranes for Integrated Quantum Technologies. *Nano Letters* **2021**, *21*, 10392–10399.

(54) Mak, K. F.; Shan, J. Photonics and optoelectronics of 2D semiconductor transition metal dichalcogenides. *Nature Photonics* **2016**, *10*, 216–226.

(55) Wang, G.; Chernikov, A.; Glazov, M. M.; Heinz, T. F.; Marie, X.; Amand, T.; Urbaszek, B. Colloquium: Excitons in atomically thin transition metal dichalcogenides. *Reviews of Modern Physics* **2018**, *90*, 21001.

(56) Kormányos, A.; Burkard, G.; Gmitra, M.; Fabian, J.; Zólyomi, V.; Drummond, N. D.; Falko, V. K P Theory for Two-Dimensional Transition Metal Dichalcogenide Semiconductors. *2D Materials* **2015**, *2*, 022001.

(57) Cadiz, F. et al. Excitonic Linewidth Approaching the Homogeneous Limit in MoS_2-Based van der Waals Heterostructures. *Physical Review X* **2017**, *7*, 021026.

(58) Chernikov, A.; Berkelbach, T. C.; Hill, H. M.; Rigosi, A.; Li, Y.; Aslan, O. B.; Reichman, D. R.; Hybertsen, M. S.; Heinz, T. F. Exciton binding energy and nonhydrogenic Rydberg series in monolayer WS_2. *Physical Review Letters* **2014**, *113*, 1–5.

(59) Latini, S.; Olsen, T.; Thygesen, K. S. Excitons in van der Waals heterostructures: The important role of dielectric screening. *Physical Review B - Condensed Matter and Materials Physics* **2015**, *92*, 1–13.

(60) Chichibu, S.; Azuhata, T.; Sota, T.; Nakamura, S. Spontaneous emission of localized excitons in InGaN single and multiquantum well structures. *Applied Physics Letters* **1996**, *69*, 4188–4190.

(61) Scuri, G.; Zhou, Y.; High, A. A.; Wild, D. S.; Shu, C.; De Greve, K.; Jauregui, L. A.; Taniguchi, T.; Watanabe, K.; Kim, P.; Lukin, M. D.; Park, H. Large Excitonic Reflectivity of Monolayer $MoSe_2$ Encapsulated in Hexagonal Boron Nitride. *Physical Review Letters* **2018**, *120*, 37402.

(62) Ajayi, O. A.; Ardelean, J. V.; Shepard, G. D.; Wang, J.; Antony, A.; Taniguchi, T.; Watanabe, K.; Heinz, T. F.; Strauf, S.; Zhu, X. Y.; Hone, J. C. Approaching the intrinsic photoluminescence linewidth in transition metal dichalcogenide monolayers. *2D Materials* **2017**, *4*.

(63) Chernikov, A.; Van Der Zande, A. M.; Hill, H. M.; Rigosi, A. F.; Velauthapillai, A.; Hone, J.; Heinz, T. F. Electrical Tuning of Exciton Binding Energies in Monolayer WS_2. *Physical Review Letters* **2015**, *115*, 1–6.

(64) Xiao, D.; Liu, G.-B.; Feng, W.; Xu, X.; Yao, W. Coupled Spin and Valley Physics in Monolayers of MoS_2 and Other Group-VI Dichalcogenides. *Physical Review Letters* **2012**, *108*, 196802.

(65) Cao, T.; Wang, G.; Han, W.; Ye, H.; Zhu, C.; Shi, J.; Niu, Q.; Tan, P.; Wang, E.; Liu, B.; Feng, J. Valley-selective circular dichroism of monolayer molybdenum disulphide. *Nature Communications* **2012**, *3*, DOI: `10.1038/ncomms1882`.

(66) Srivastava, A.; Sidler, M.; Allain, A. V.; Lembke, D. S.; Kis, A.; Imamoglu, A. Valley Zeeman effect in elementary optical excitations of monolayer WSe_2, volume = 11, year = 2015. *Nature Physics*, 141–147.

(67) Aivazian, G.; Gong, Z.; Jones, A. M.; Chu, R. L.; Yan, J.; Mandrus, D. G.; Zhang, C.; Cobden, D.; Yao, W.; Xu, X. Magnetic control of valley pseudospin in monolayer WSe_2. *Nature Physics* **2015**, *11*, 148–152.

(68) Geim, A. K.; Grigorieva, I. V. Van der Waals heterostructures. *Nature* **2013**, *499*, 419–425.

(69) Jiang, Y.; Chen, S.; Zheng, W.; Zheng, B.; Pan, A. Interlayer exciton formation, relaxation, and transport in TMD van der Waals heterostructures. *Light: Science and Applications* **2021**, *10*, 1–29.

(70) Huang, D.; Choi, J.; Shih, C.-k.; Li, X. Excitons in semiconductor moiré superlattices. *Nature Nanotechnology* **2022**, *17*, DOI: `10.1038/s41565-021-01068-y`.

(71) Pizzocchero, F.; Gammelgaard, L.; Jessen, B. S.; Caridad, J. M.; Wang, L.; Hone, J.; Bøggild, P.; Booth, T. J. The hot pick-up technique for batch assembly of van der Waals heterostructures. *Nature Communications* **2016**, *7*, DOI: `10.1038/ncomms11894`.

(72) Shreiner, R.; Hao, K.; Butcher, A.; High, A. A. Electrically controllable chirality in a nanophotonic interface with a two-dimensional semiconductor. *Nature Photonics* **2022**, *16*, DOI: `10.1038/s41566-022-00971-7`.

(73) Li, J.; Goryca, M.; Yumigeta, K.; Li, H.; Tongay, S.; Crooker, S. A. Valley relaxation of resident electrons and holes in a monolayer semiconductor: Dependence on carrier density and the role of substrate-induced disorder. *Physical Review Materials* **2021**, *5*, 1–11.

(74) Huang, Y. et al. Universal mechanical exfoliation of large-area 2D crystals. *Nature Communications* **2020**, *11*, DOI: `10.1038/s41467-020-16266-w`.

(75) Liu, F.; Wu, W.; Bai, Y.; Chae, S. H.; Li, Q.; Wang, J.; Hone, J.; Zhu, X. Y. Disassembling 2D van der Waals crystals into macroscopic monolayers and reassembling into artificial lattices. *Science* **2020**, *367*, 903–906.

(76) Ma, X.; Youngblood, N.; Liu, X.; Cheng, Y.; Cunha, P.; Kudtarkar, K.; Wang, X.; Lan, S. Engineering photonic environments for two-dimensional materials. *Nanophotonics* **2021**, *10*, 1031–1058.

(77) Liu, X.; Galfsky, T.; Sun, Z.; Xia, F.; Lin, E. C.; Lee, Y. H.; Kéna-Cohen, S.; Menon, V. M. Strong light-matter coupling in two-dimensional atomic crystals. *Nature Photonics* **2014**, *9*, 30–34.

(78) Cotrufo, M.; Sun, L.; Choi, J.; Alù, A.; Li, X. Enhancing functionalities of atomically thin semiconductors with plasmonic nanostructures. *Nanophotonics* **2019**, *8*, 577–598.

(79) Rogers, C.; Gray, D.; Bogdanowicz, N.; Taniguchi, T.; Watanabe, K.; Mabuchi, H. Coherent feedback control of two-dimensional excitons. *Physical Review Research* **2020**, *2*, 12029.

(80) Zhou, Y.; Scuri, G.; Sung, J.; Gelly, R. J.; Wild, D. S.; De Greve, K.; Joe, A. Y.; Taniguchi, T.; Watanabe, K.; Kim, P.; Lukin, M. D.; Park, H. Controlling Excitons in an Atomically Thin Membrane with a Mirror. *Physical Review Letters* **2020**, *124*, 27401.

(81) Fang, H. H.; Han, B.; Robert, C.; Semina, M. A.; Lagarde, D.; Courtade, E.; Taniguchi, T.; Watanabe, K.; Amand, T.; Urbaszek, B.; Glazov, M. M.; Marie, X. Control of the Exciton Radiative Lifetime in van der Waals Heterostructures. *Physical Review Letters* **2019**, *123*, 67401.

(82) Wu, S.; Buckley, S.; Schaibley, J. R.; Feng, L.; Yan, J.; Mandrus, D. G.; Hatami, F.; Yao, W.; Vučković, J.; Majumdar, A.; Xu, X. Monolayer semiconductor nanocavity lasers with ultralow thresholds. *Nature* **2015**, *520*, 69–72.

(83) Gong, S. H.; Gong, S. H.; Komen, I.; Alpeggiani, F.; Kuipers, L. Nanoscale Optical Addressing of Valley Pseudospins through Transverse Optical Spin. *Nano Letters* **2020**, *20*, 4410–4415.

(84) Li, Y.; Zhang, J.; Huang, D.; Sun, H.; Fan, F.; Feng, J.; Wang, Z.; Ning, C. Z. Room-temperature continuous-wave lasing from monolayer molybdenum ditelluride integrated with a silicon nanobeam cavity. *Nature Nanotechnology* **2017**, *12*, 987–992.

(85) Sortino, L.; Zotev, P. G.; Mignuzzi, S.; Cambiasso, J.; Schmidt, D.; Genco, A.; Aßmann, M.; Bayer, M.; Maier, S. A.; Sapienza, R.; Tartakovskii, A. I. Enhanced light-matter interaction in an atomically thin semiconductor coupled with dielectric nanoantennas. *Nature Communications* **2019**, *10*, DOI: `10.1038/s41467-019-12963-3`.

(86) Salehzadeh, O.; Djavid, M.; Tran, N. H.; Shih, I.; Mi, Z. Optically Pumped Two-Dimensional MoS2 Lasers Operating at Room-Temperature. *Nano Letters* **2015**, *15*, 5302–5306.

(87) Javerzac-Galy, C.; Kumar, A.; Schilling, R. D.; Piro, N.; Khorasani, S.; Barbone, M.; Goykhman, I.; Khurgin, J. B.; Ferrari, A. C.; Kippenberg, T. J. Excitonic Emission of Monolayer Semiconductors Near-Field Coupled to High-Q Microresonators. *Nano Letters* **2018**, *18*, 3138–3146.

(88) Gatto Monticone, D.; Katamadze, K.; Traina, P.; Moreva, E.; Forneris, J.; Ruo-Berchera, I.; Olivero, P.; Degiovanni, I. P.; Brida, G.; Genovese, M. Beating the abbe diffraction limit in confocal microscopy via nonclassical photon statistics. *Physical Review Letters* **2014**, *113*, 1–5.

(89) Butcher, A.; Guo, X.; Shreiner, R.; Delegan, N.; Hao, K.; Duda, P.; Awschalom, D.; Awschalom, D.; Heremans, F.; Heremans, F.; High, A.; High, A. High- Q Nanophotonic Resonators on Diamond Membranes using Templated Atomic Layer Deposition of TiO_2. *Nano Letters* **2020**, *20*, DOI: `10.1021/acs.nanolett.0c01467`.

(90) Aarik, J.; Aidla, A.; Kiisler, A. A.; Uustare, T.; Sammelselg, V. Effect of crystal structure on optical properties of TiO_2 films grown by atomic layer deposition. *Thin Solid Films* **1997**, *305*, 270–273.

(91) Wood, M. G.; Chen, L.; Burr, J. R.; Reano, R. M. Optimization of electron beam patterned hydrogen silsesquioxane mask edge roughness for low-loss silicon waveguides. *Journal of Nanophotonics* **2014**, *8*, 083098.

(92) Walker, E. J. Reduction of photoresist standing-wave effects by post-exposure bake. *IEEE Transactions on Electron Devices* **1975**, *22*, 464–466.

(93) Miyoshi, H.; Taniguchi, J. Fabricating a high-resolution mask with improved line-edge roughness by using a nonchemically amplified resist and a postexposure bake. *Journal of vacuum science and technology. B, Nanotechnology and microelectronics : materials, processing, measurement, and phenomena : JVST B* **2015**, *33*, 06FD05–06FD05.

(94) Hu, W. W.; Sarveswaran, K.; Lieberman, M.; Bernstein, G. H. Sub-10 nm electron beam lithography using cold development of poly(methylmethacrylate). *Journal of Vacuum Science and Technology B: Microelectronics and Nanometer Structures* **2004**, *22*, 1711.

(95) Devlin, R. C.; Khorasaninejad, M.; Chen, W. T.; Oh, J.; Capasso, F. Broadband high-efficiency dielectric metasurfaces for the visible spectrum. *Proceedings of the National Academy of Sciences of the United States of America* **2016**, *113*, 10473–10478.

(96) Khorasaninejad, M.; Chen, W. T.; Devlin, R. C.; Oh, J.; Zhu, A. Y.; Capasso, F. Metalenses at visible wavelengths: Diffraction-limited focusing and subwavelength resolution imaging. *Science* **2016**, *352*, 1190–1194.

(97) Bakri, A. S.; Sahdan, M. Z.; Adriyanto, F.; Raship, N. A.; Said, N. D.; Abdullah, S. A.; Rahim, M. S. Effect of annealing temperature of titanium dioxide thin films on structural and electrical properties. *AIP Conference Proceedings* **2017**, *1788*, DOI: `10.1063/1.4968283`.

(98) Pham, H. H.; Wang, L. W. Oxygen vacancy and hole conduction in amorphous TiO_2. *Physical Chemistry Chemical Physics* **2015**, *17*, 541–550.

(99) Bogaerts, W.; De Heyn, P.; Vaerenbergh, T. V.; De Vos, K.; Selvaraja, S. K.; Claes, T.; Dumon, P.; Bienstman, P.; Thourhout, V.; Baets, R. Silicon microring resonators. *Laser Photonics Rev* **2012**, *6*, 47–73.

(100) Martin-Cano, D.; Haakh, H. R.; Rotenberg, N. Chiral Emission into Nanophotonic Resonators. *ACS Photonics* **2019**, *6*, 961–966.

(101) Faraon, A.; Santori, C.; Huang, Z.; Fu, K. M. C.; Acosta, V. M.; Fattal, D.; Beausoleil, R. G. Quantum photonic devices in single-crystal diamond. *New Journal of Physics* **2013**, *15*.

(102) Choy, J. T.; Bradley, J. D. B.; Deotare, P. B.; Burgess, I. B.; Evans, C. C.; Mazur, E.; Lončar, M. Integrated TiO_2 resonators for visible photonics. *Optics Letters* **2012**, *37*, 539.

(103) Awschalom, D. D.; Hanson, R.; Wrachtrup, J.; Zhou, B. B. Quantum technologies with optically interfaced solid-state spins. *Nature Photonics* **2018**, *12*, 516–527.

(104) Burek, M. J.; De Leon, N. P.; Shields, B. J.; Hausmann, B. J.; Chu, Y.; Quan, Q.; Zibrov, A. S.; Park, H.; Lukin, M. D.; Lončar, M. Free-standing mechanical and photonic nanostructures in single-crystal diamond. *Nano Letters* **2012**, *12*, 6084–6089.

(105) Burek, M. J.; Chu, Y.; Liddy, M. S.; Patel, P.; Rochman, J.; Meesala, S.; Hong, W.; Quan, Q.; Lukin, M. D.; Loncar, M. High quality-factor optical nanocavities in bulk single-crystal diamond. *Nature Communications* **2014**, *5*, 1–7.

(106) Bayn, I.; Mouradian, S.; Li, L.; Goldstein, J. A.; Schröder, T.; Zheng, J.; Chen, E. H.; Gaathon, O.; Lu, M.; Stein, A.; Ruggiero, C. A.; Salzman, J.; Kalish, R.; Englund, D. Fabrication of triangular nanobeam waveguide networks in bulk diamond using single-crystal silicon hard masks. *Applied Physics Letters* **2014**, *105*.

(107) Mouradian, S.; Wan, N. H.; Schröder, T.; Englund, D. Rectangular photonic crystal nanobeam cavities in bulk diamond. *Applied Physics Letters* **2017**, *111*, 0–4.

(108) Piracha, A. H.; Rath, P.; Ganesan, K.; Kühn, S.; Pernice, W. H.; Prawer, S. Scalable Fabrication of Integrated Nanophotonic Circuits on Arrays of Thin Single Crystal Diamond Membrane Windows. *Nano Letters* **2016**, *16*, 3341–3347.

(109) Hausmann, B. J.; Shields, B.; Quan, Q.; Maletinsky, P.; McCutcheon, M.; Choy, J. T.; Babinec, T. M.; Kubanek, A.; Yacoby, A.; Lukin, M. D.; Lončar, M. Integrated diamond networks for quantum nanophotonics. *Nano Letters* **2012**, *12*, 1578–1582.

(110) Gould, M.; Schmidgall, E. R.; Dadgostar, S.; Hatami, F.; Fu, K. M. C. Efficient Extraction of Zero-Phonon-Line Photons from Single Nitrogen-Vacancy Centers in an Integrated GaP-on-Diamond Platform. *Physical Review Applied* **2016**, *6*, 2–7.

(111) Schmidgall, E. R.; Chakravarthi, S.; Gould, M.; Christen, I. R.; Hestroffer, K.; Hatami, F.; Fu, K. M. C. Frequency Control of Single Quantum Emitters in Integrated Photonic Circuits. *Nano Letters* **2018**, *18*, 1175–1179.

(112) Barclay, P. E.; Fu, K. M. C.; Santori, C.; Beausoleil, R. G. Chip-based microcavities coupled to nitrogen-vacancy centers in single crystal diamond. *Applied Physics Letters* **2009**, *95*, 93–96.

(113) Li, L.; Schröder, T.; Chen, E. H.; Walsh, M.; Bayn, I.; Goldstein, J.; Gaathon, O.; Trusheim, M. E.; Lu, M.; Mower, J.; Cotlet, M.; Markham, M. L.; Twitchen, D. J.; Englund, D. Coherent spin control of a nanocavity-enhanced qubit in diamond. *Nature Communications* **2015**, *6*.

(114) Myers, B. A.; Das, A.; Dartiailh, M. C.; Ohno, K.; Awschalom, D. D.; Bleszynski Jayich, A. C. Probing surface noise with depth-calibrated spins in diamond. *Physical Review Letters* **2014**, *113*, 1–6.

(115) Kim, M.; Mamin, H. J.; Sherwood, M. H.; Ohno, K.; Awschalom, D. D.; Rugar, D. Decoherence of Near-Surface Nitrogen-Vacancy Centers Due to Electric Field Noise. *Physical Review Letters* **2015**, *115*, 1–5.

(116) Sangtawesin, S. et al. Origins of Diamond Surface Noise Probed by Correlating Single-Spin Measurements with Surface Spectroscopy. *Physical Review X* **2019**, *9*, 1–17.

(117) Dobrovitski, V. V.; Fuchs, G. D.; Falk, A. L.; Santori, C.; Awschalom, D. D. Quantum control over single spins in diamond. *Annual Review of Condensed Matter Physics* **2013**, *4*, 23–50.

(118) Hepp, C.; Müller, T.; Waselowski, V.; Becker, J. N.; Pingault, B.; Sternschulte, H.; Steinmüller-Nethl, D.; Gali, A.; Maze, J. R.; Atatüre, M.; Becher, C. Electronic structure of the silicon vacancy color center in diamond. *Physical Review Letters* **2014**, *112*, 1–5.

(119) Payne, F. P.; Lacey, J. P. A theoretical analysis of scattering loss from planar optical waveguides. *Optical and Quantum Electronics* **1994**, *26*, 977–986.

(120) High, A. A.; Devlin, R. C.; Dibos, A.; Polking, M.; Wild, D. S.; Perczel, J.; De Leon, N. P.; Lukin, M. D.; Park, H. Visible-frequency hyperbolic metasurface. *Nature* **2015**, *522*, 192–196.

(121) Magyar, A. P.; Lee, J. C.; Limarga, A. M.; Aharonovich, I.; Rol, F.; Clarke, D. R.; Huang, M.; Hu, E. L. Fabrication of thin, luminescent, single-crystal diamond membranes. *Applied Physics Letters* **2011**, *99*, 1–4.

(122) Tao, Y.; Degen, C. Facile fabrication of single-crystal-diamond nanostructures with ultrahigh aspect ratio. *Advanced Materials* **2013**, *25*, 3962–3967.

(123) Jung, T.; Kreiner, L.; Pauly, C.; Mücklich, F.; Edmonds, A. M.; Markham, M.; Becher, C. Reproducible fabrication and characterization of diamond membranes for photonic crystal cavities. *Physica Status Solidi (A) Applications and Materials Science* **2016**, *213*, 3254–3264.

(124) Holzwarth, C. W.; Barwicz, T.; Smith, H. I. Optimization of hydrogen silsesquioxane for photonic applications. *Journal of Vacuum Science and Technology B: Microelectronics and Nanometer Structures* **2007**, *25*, 2658.

(125) Choi, S.; Word, M. J.; Kumar, V.; Adesida, I. Comparative study of thermally cured and electron-beam-exposed hydrogen silsesquioxane resists. *Journal of Vacuum Science and Technology B: Microelectronics and Nanometer Structures* **2008**, *26*, 1654.

(126) Zhang, J. L.; Sun, S.; Burek, M. J.; Dory, C.; Tzeng, Y. K.; Fischer, K. A.; Kelaita, Y.; Lagoudakis, K. G.; Radulaski, M.; Shen, Z. X.; Melosh, N. A.; Chu, S.; Lončar, M.; Vučković, J. Strongly Cavity-Enhanced Spontaneous Emission from Silicon-Vacancy Centers in Diamond. *Nano Letters* **2018**, *18*, 1360–1365.

(127) Bhaskar, M. K.; Riedinger, R.; Machielse, B.; Levonian, D. S.; Nguyen, C. T.; Knall, E. N.; Park, H.; Englund, D.; Lončar, M.; Sukachev, D. D.; Lukin, M. D. Experimental demonstration of memory-enhanced quantum communication. *Nature* **2020**, *580*, 60–64.

(128) Mosor, S.; Hendrickson, J.; Richards, B. C.; Sweet, J.; Khitrova, G.; Gibbs, H. M.; Yoshie, T.; Scherer, A.; Shchekin, O. B.; Deppe, D. G. Scanning a photonic crystal slab nanocavity by condensation of xenon. *Applied Physics Letters* **2005**, *87*, 1–3.

(129) Christle, D. J.; Falk, A. L.; Andrich, P.; Klimov, P. V.; Hassan, J. U.; Son, N. T.; Janzén, E.; Ohshima, T.; Awschalom, D. D. Isolated electron spins in silicon carbide with millisecond coherence times. *Nature Materials* **2015**, *14*, 160–163.

(130) Widmann, M. et al. Coherent control of single spins in silicon carbide at room temperature. *Nature Materials* **2015**, *14*, 164–168.

(131) Crook, A. L.; Anderson, C. P.; Miao, K. C.; Bourassa, A.; Lee, H.; Bayliss, S. L.; Bracher, D. O.; Zhang, X.; Abe, H.; Ohshima, T.; Hu, E. L.; Awschalom, D. D. Purcell enhancement of a single silicon carbide color center with coherent spin control. *Nano Letters* **2020**, *20*, 3427–3434.

(132) Aiello, A.; Banzer, P.; Neugebauer, M.; Leuchs, G. From transverse angular momentum to photonic wheels. *Nature Photonics* **2015**, *9*, 789–795.

(133) Bliokh, K. Y.; Rodríguez-Fortuño, F. J.; Nori, F.; Zayats, A. V. Spin-orbit interactions of light. *Nature Photonics* **2015**, *9*, 796–808.

(134) Watts, A. B. et al. Chiral nanophotonic waveguide interface based on spin-orbit interaction of light. *Science* **2014**, *346*, 67–72.

(135) Mitsch, R.; Sayrin, C.; Albrecht, B.; Schneeweiss, P.; Rauschenbeutel, A. Quantum state-controlled directional spontaneous emission of photons into a nanophotonic waveguide. *Nature Communications* **2014**, *5*, 1–5.

(136) Sayrin, C.; Junge, C.; Mitsch, R.; Albrecht, B.; O'Shea, D.; Schneeweiss, P.; Volz, J.; Rauschenbeutel, A. Nanophotonic optical isolator controlled by the internal state of cold atoms. *Physical Review X* **2015**, *5*, 1–9.

(137) Shomroni, I.; Rosenblum, S.; Lovsky, Y.; Bechler, O.; Guendelman, G.; Dayan, B. All-optical routing of single photons by a one-atom switch controlled by a single photon. *Science* **2014**, *345*, 903–906.

(138) Le Feber, B.; Rotenberg, N.; Kuipers, L. Nanophotonic control of circular dipole emission. *Nature Communications* **2015**, *6*, 2–7.

(139) Söllner, I.; Mahmoodian, S.; Hansen, S. L.; Midolo, L.; Javadi, A.; Kiršanske, G.; Pregnolato, T.; El-Ella, H.; Lee, E. H.; Song, J. D.; Stobbe, S.; Lodahl, P. Deterministic photon-emitter coupling in chiral photonic circuits. *Nature Nanotechnology* **2015**, *10*, 775–778.

(140) Kapitanova, P. V.; Ginzburg, P.; Rodríguez-Fortuño, F. J.; Filonov, D. S.; Voroshilov, P. M.; Belov, P. A.; Poddubny, A. N.; Kivshar, Y. S.; Wurtz, G. A.; Zayats, A. V. Photonic spin Hall effect in hyperbolic metamaterials for polarization-controlled routing of subwavelength modes. *Nature Communications* **2014**, *5*.

(141) Lin, J.; Mueller, J. P.; Wang, Q.; Yuan, G.; Antoniou, N.; Yuan, X. C.; Capasso, F. Polarization-controlled tunable directional coupling of surface plasmon polaritons. *Science* **2013**, *340*, 331–334.

(142) Tang, L.; Tang, J.; Zhang, W.; Lu, G.; Zhang, H.; Zhang, Y.; Xia, K.; Xiao, M. On-chip chiral single-photon interface: Isolation and unidirectional emission. *Physical Review A* **2019**, *99*, 43833.

(143) Lodahl, P.; Mahmoodian, S.; Stobbe, S.; Rauschenbeutel, A.; Schneeweiss, P.; Volz, J.; Pichler, H.; Zoller, P. Chiral quantum optics. *Nature* **2017**, *541*, 473–480.

(144) Hendry, E.; Carpy, T.; Johnston, J.; Popland, M.; Mikhaylovskiy, R. V.; Lapthorn, A. J.; Kelly, S. M.; Barron, L. D.; Gadegaard, N.; Kadodwala, M. Ultrasensitive detection and characterization of biomolecules using superchiral fields. *Nature Nanotechnology* **2010**, *5*, 783–787.

(145) Tang, Y.; Cohen, A. E. Enhanced enantioselectivity in excitation of chiral molecules by superchiral light. *Science* **2011**, *332*, 333–336.

(146) Zhao, Y.; Askarpour, A. N.; Sun, L.; Shi, J.; Li, X.; Alù, A. Chirality detection of enantiomers using twisted optical metamaterials. *Nature Communications* **2017**, *8*, 6–13.

(147) Zhang, Q.; Hernandez, T.; Smith, K. W.; Jebeli, S. A. H.; Dai, A. X.; Warning, L.; Baiyasi, R.; McCarthy, L. A.; Guo, H.; Chen, D. H.; Dionne, J. A.; Landes, C. F.; Link, S. Unraveling the origin of chirality from plasmonic nanoparticle-protein complexes. *Science* **2019**, *365*, 1475–1478.

(148) Mak, K. F.; Lee, C.; Hone, J.; Shan, J.; Heinz, T. F. Atomically thin MoS_2: A new direct-gap semiconductor. *Physical Review Letters* **2010**, *105*, 2–5.

(149) Splendiani, A.; Sun, L.; Zhang, Y.; Li, T.; Kim, J.; Chim, C. Y.; Galli, G.; Wang, F. Emerging photoluminescence in monolayer MoS_2. *Nano Letters* **2010**, *10*, 1271–1275.

(150) Zeng, H.; Dai, J.; Yao, W.; Xiao, D.; Cui, X. Valley polarization in MoS_2 monolayers by optical pumping. *Nature Nanotechnology* **2012**, *7*, 490–493.

(151) Mak, K. F.; He, K.; Shan, J.; Heinz, T. F. Control of valley polarization in monolayer MoS_2 by optical helicity. *Nature Nanotechnology* **2012**, *7*, 494–498.

(152) Chervy, T.; Azzini, S.; Lorchat, E.; Wang, S.; Gorodetski, Y.; Hutchison, J. A.; Berciaud, S.; Ebbesen, T. W.; Genet, C. Room Temperature Chiral Coupling of Valley Excitons with Spin-Momentum Locked Surface Plasmons. *ACS Photonics* **2018**, *5*, 1281–1287.

(153) Sun, L.; Wang, C. Y.; Krasnok, A.; Choi, J.; Shi, J.; Gomez-Diaz, J. S.; Zepeda, A.; Gwo, S.; Shih, C. K.; Alù, A.; Li, X. Separation of valley excitons in a MoS_2 monolayer using a subwavelength asymmetric groove array. *Nature Photonics* **2019**, *13*, 180–184.

(154) Yang, Z.; Aghaeimeibodi, S.; Waks, E. Chiral light-matter interactions using spin-valley states in transition metal dichalcogenides. *Optics Express* **2019**, *27*, 21367.

(155) Guo, Q.; Fu, T.; Tang, J.; Pan, D.; Zhang, S.; Xu, H. Routing a Chiral Raman Signal Based on Spin-Orbit Interaction of Light. *Physical Review Letters* **2019**, *123*, 183903.

(156) Liu, W.; Ji, Z.; Wang, Y.; Modi, G.; Hwang, M.; Zheng, B.; Sorger, V. J.; Pan, A.; Agarwal, R. Generation of helical topological exciton-polaritons. *Science* **2020**, *370*, 600–604.

(157) Barbone, M. et al. Charge-tuneable biexciton complexes in monolayer WSe_2. *Nature Communications* **2018**, *9*.

(158) Dey, P.; Yang, L.; Robert, C.; Wang, G.; Urbaszek, B.; Marie, X.; Crooker, S. A. Gate-Controlled Spin-Valley Locking of Resident Carriers in WSe_2 Monolayers. *Physical Review Letters* **2017**, *119*, 1–5.

(159) Rice, W. D.; Ambwani, P.; Bombeck, M.; Thompson, J. D.; Haugstad, G.; Leighton, C.; Crooker, S. A. Persistent optically induced magnetism in oxygen-deficient strontium titanate. *Nature Materials* **2014**, *13*, 481–487.

(160) Lalieu, M. L.; Lavrijsen, R.; Koopmans, B. Integrating all-optical switching with spintronics. *Nature Communications* **2019**, *10*, 1–6.

(161) Zhou, Y.; Scuri, G.; Wild, D. S.; High, A. A.; Dibos, A.; Jauregui, L. A.; Shu, C.; De Greve, K.; Pistunova, K.; Joe, A. Y.; Taniguchi, T.; Watanabe, K.; Kim, P.; Lukin, M. D.; Park, H. Probing dark excitons in atomically thin semiconductors via near-field coupling to surface plasmon polaritons. *Nature Nanotechnology* **2017**, *12*, 856–860.

(162) Ye, Z.; Waldecker, L.; Ma, E. Y.; Rhodes, D.; Antony, A.; Kim, B.; Zhang, X. X.; Deng, M.; Jiang, Y.; Lu, Z.; Smirnov, D.; Watanabe, K.; Taniguchi, T.; Hone, J.; Heinz, T. F. Efficient generation of neutral and charged biexcitons in encapsulated WSe_2 monolayers. *Nature Communications* **2018**, *9*, 6–11.

(163) Li, Z.; Wang, T.; Lu, Z.; Jin, C.; Chen, Y.; Meng, Y.; Lian, Z.; Taniguchi, T.; Watanabe, K.; Zhang, S.; Smirnov, D.; Shi, S. F. Revealing the biexciton and trion-exciton complexes in BN encapsulated WSe_2. *Nature Communications* **2018**, *9*, 1–7.

(164) Kulig, M.; Zipfel, J.; Nagler, P.; Blanter, S.; Schüller, C.; Korn, T.; Paradiso, N.; Glazov, M. M.; Chernikov, A. Exciton Diffusion and Halo Effects in Monolayer Semiconductors. *Physical Review Letters* **2018**, *120*, 207401.

(165) Glazov, M. M. Quantum Interference Effect on Exciton Transport in Monolayer Semiconductors. *Physical Review Letters* **2020**, *124*, 166802.

(166) Unuchek, D.; Ciarrocchi, A.; Avsar, A.; Watanabe, K.; Taniguchi, T.; Kis, A. Room-temperature electrical control of exciton flux in a van der Waals heterostructure. *Nature* **2018**, *560*, 340–344.

(167) Unuchek, D.; Ciarrocchi, A.; Avsar, A.; Sun, Z.; Watanabe, K.; Taniguchi, T.; Kis, A. Valley-polarized exciton currents in a van der Waals heterostructure. *Nature Nanotechnology* **2019**, *14*, 1104–1109.

(168) Jin, C.; Regan, E. C.; Yan, A.; Iqbal Bakti Utama, M.; Wang, D.; Zhao, S.; Qin, Y.; Yang, S.; Zheng, Z.; Shi, S.; Watanabe, K.; Taniguchi, T.; Tongay, S.; Zettl, A.; Wang, F. Observation of moiré excitons in WSe_2/WS_2 heterostructure superlattices. *Nature* **2019**, *567*, 76–80.

(169) Costache, M. V.; Sladkov, M.; Watts, S. M.; Van Der Wal, C. H.; Van Wees, B. J. Electrical detection of spin pumping due to the precessing magnetization of a single ferromagnet. *Physical Review Letters* **2006**, *97*, 1–4.

(170) Sanchez, O. L.; Ovchinnikov, D.; Misra, S.; Allain, A.; Kis, A. Valley Polarization by Spin Injection in a Light-Emitting van der Waals Heterojunction. *Nano Letters* **2016**, *16*, 5792–5797.

(171) Zutic, I.; Fabian, J.; Das Sarma, S. Spintronics: Fundamentals and applications. *Rev. Mod. Phys.* **2004**, *76*, 323–410.

(172) Cadiz, F.; Robert, C.; Courtade, E.; Manca, M.; Martinelli, L.; Taniguchi, T.; Watanabe, K.; Amand, T.; Rowe, A. C.; Paget, D.; Urbaszek, B.; Marie, X. Exciton diffusion in WSe_2 monolayers embedded in a van der Waals heterostructure. *Applied Physics Letters* **2018**, *112*.

(173) Liu, E.; Van Baren, J.; Lu, Z.; Altaiary, M. M.; Taniguchi, T.; Watanabe, K.; Smirnov, D.; Lui, C. H. Gate Tunable Dark Trions in Monolayer WSe_2. *Physical Review Letters* **2019**, *123*, 27401.

(174) Datta, I.; Chae, S. H.; Bhatt, G. R.; Tadayon, M. A.; Li, B.; Yu, Y.; Park, C.; Park, J.; Cao, L.; Basov, D. N.; Hone, J.; Lipson, M. Low-loss composite photonic platform based on 2D semiconductor monolayers. *Nature Photonics* **2020**, *14*, 256–262.

(175) Seol, M.; Lee, M. H.; Kim, H.; Shin, K. W.; Cho, Y.; Jeon, I.; Jeong, M.; Lee, H. I.; Park, J.; Shin, H. J. High-Throughput Growth of Wafer-Scale Monolayer Transition Metal Dichalcogenide via Vertical Ostwald Ripening. *Advanced Materials* **2020**, *32*, DOI: `10.1002/adma.202003542`.

(176) Mannix, A. J.; Ye, A.; Sung, S. H.; Ray, A.; Mujid, F.; Park, C.; Lee, M.; Kang, J. H.; Shreiner, R.; High, A. A.; Muller, D. A.; Hovden, R.; Park, J. Robotic four-dimensional pixel assembly of van der Waals solids. *Nature Nanotechnology* **2022**, DOI: `10.1038/s41565-021-01061-5`.

(177) Tran, K. et al. Evidence for moiré excitons in van der Waals heterostructures. *Nature* **2019**, *567*, 71–75.

(178) Seyler, K. L.; Rivera, P.; Yu, H.; Wilson, N. P.; Ray, E. L.; Mandrus, D. G.; Yan, J.; Yao, W.; Xu, X. Signatures of moiré-trapped valley excitons in $MoSe_2/WSe_2$ heterobilayers. *Nature* **2019**, *567*, 66–70.

(179) Ciarrocchi, A.; Unuchek, D.; Avsar, A.; Watanabe, K.; Taniguchi, T.; Kis, A. Polarization switching and electrical control of interlayer excitons in two-dimensional van der Waals heterostructures. *Nature Photonics* **2019**, *13*, 131–136.

(180) High, A. A.; Novitskaya, E. E.; Butov, L. V.; Hanson, M.; Gossard, A. C. Control of exciton fluxes in an excitonic integrated circuit. *Science* **2008**, *321*, 229–231.

(181) Jauregui, L. A. et al. Electrical control of interlayer exciton dynamics in atomically thin heterostructures. *Science* **2019**, *366*, 870–875.

(182) Liu, Y.; Dini, K.; Tan, Q.; Liew, T.; Novoselov, K. S.; Gao, W. Electrically controllable router of interlayer excitons. *Science Advances* **2020**, *6*, 3–7.

(183) Robert, C. et al. Spin/valley pumping of resident electrons in WSe_2 and WS_2 monolayers. *Nature Communications* **2021**, *12*, 1–7.

(184) Hao, K.; Shreiner, R.; High, A. A. Optically controllable magnetism in atomically thin semiconductors. *arXiv:2108.05931* **2021**.

(185) Guddala, S.; Kawaguchi, Y.; Komissarenko, F.; Kiriushechkina, S.; Vakulenko, A.; Chen, K.; Alù, A.; M. Menon, V.; Khanikaev, A. B. All-optical nonreciprocity due to valley polarization pumping in transition metal dichalcogenides. *Nature Communications* **2021**, *12*, DOI: `10.1038/s41467-021-24138-0`.

(186) Butcher, A.; High, A. A. All-dielectric multi-resonant bullseye antennas. *Optics E* **2022**, *30*, 12092–12103.

(187) Zhong, T.; Kindem, J. M.; Miyazono, E.; Faraon, A. Nanophotonic coherent light-matter interfaces based on rare-earth-doped crystals. *Nature Communications* **2015**, *6*, 1–6.

(188) Xavier, J.; Yu, D.; Vollmer, F.; Jones, C.; Zossimova, E. Quantum nanophotonic and nanoplasmonic sensing: Towards quantum optical bioscience laboratories on chip. *Nanophotonics* **2021**, *10*, 1387–1435.

(189) Schubert, E. F.; Hunt, N. E. J.; Micovic, M; Malik, R. J.; Sivco, D. L.; Cho, A. Y.; Zydzik, G. J. Highly Efficient Light-Emitting Diodes with Microcavities. *Science* **1994**, *265*, 943–945.

(190) Pelton, M.; Santori, C.; Vuckovic, J.; Zhang, B.; Solomon, G. S.; Plant, J.; Yamamoto, Y. Efficient Source of Single Photons: A Single Quantum Dot in a Micropost Microcavity. *Physical Review Letters* **2002**, *89*, 1–4.

(191) Qi, Y.; Li, Y. Integrated lithium niobate photonics. *Nanophotonics* **2020**, *9*, 1287–1320.

(192) Moody, G.; Chang, L.; Steiner, T. J.; Bowers, J. E. Chip-scale nonlinear photonics for quantum light generation. *AVS Quantum Science* **2020**, *2*, DOI: `10.1116/5.0020684`.

(193) Fathpour, S. Heterogeneous Nonlinear Integrated Photonics. *IEEE Journal of Quantum Electronics* **2018**, *54*, 1–16.

(194) Hendrickson, S. M.; Foster, A. C.; Camacho, R. M.; Clader, B. D. Integrated nonlinear photonics: emerging applications and ongoing challenges [Invited]. *Journal of the Optical Society of America B* **2014**, *31*, 3193.

(195) Buckley, S.; Rivoire, K.; Vuckovic, J. Multiply resonant photonic crystal cavities for nonlinear frequency conversion. *Optics Express* **2012**, *19*, 22198–22207.

(196) Ouyang, L.; Meyer-Zedler, T.; See, K. M.; Chen, W. L.; Lin, F. C.; Akimov, D.; Ehtesabi, S.; Richter, M.; Schmitt, M.; Chang, Y. M.; Gräfe, S.; Popp, J.; Huang, J. S. Spatially Resolving the Enhancement Effect in Surface-Enhanced Coherent Anti-Stokes Raman Scattering by Plasmonic Doppler Gratings. *ACS Nano* **2021**, *15*, 809–818.

(197) Tali, S. A. S.; Zhou, W. Multiresonant plasmonics with spatial mode overlap: Overview and outlook. *Nanophotonics* **2019**, *8*, 1199–1225.

(198) Fossati, S.; Hageneder, S.; Menad, S.; Maillart, E.; Dostalek, J. Multiresonant plasmonic nanostructure for ultrasensitive fluorescence biosensing. *Nanophotonics* **2020**, *9*, 3673–3685.

(199) Levy, J. S.; Foster, M. A.; Gaeta, A. L.; Lipson, M. Harmonic generation in silicon nitride ring resonators. *Optics Express* **2011**, *19*, 11415.

(200) Absil, P. P.; Hryniewicz, J. V.; Little, B. E.; Cho, P. S.; Wilson, R. A.; Joneckis, L. G.; Ho, P.-T. Wavelength conversion in GaAs micro-ring resonators. *Optics Letters* **2000**, *25*, 554.

(201) Sun, Y.; Fan, X. Optical ring resonators for biochemical and chemical sensing. *Analytical and Bioanalytical Chemistry* **2011**, *399*, 205–211.

(202) Guo, X.; Zou, C. L.; Schuck, C.; Jung, H.; Cheng, R.; Tang, H. X. Parametric down-conversion photon-pair source on a nanophotonic chip. *Light: Science and Applications* **2017**, *6*, 1–8.

(203) Bauer, C.; Giessen, H.; Schnabel, B.; Kley, E. B.; Schmitt, C.; Scherf, U.; Mahrt, R. F. A surface-emitting circular grating polymer laser. *Advanced Materials* **2001**, *13*, 1161–1164.

(204) Jordan, R. H.; Hall, D. G.; King, O.; Wicks, G.; Rishton, S. Lasing behavior of circular grating surface-emitting semiconductor lasers. *Journal of the Optical Society of America B* **1997**, *14*, 449.

(205) Schönenberger, S.; Moll, N.; Stöferle, T.; Mahrt, R. F.; Offrein, B. J.; Götzinger, S.; Sandoghdar, V.; Bolten, J.; Wahlbrink, T.; Plötzing, T.; Waldow, M.; Först, M. Circular Grating Resonators as Small Mode-Volume Microcavities for Switching. *Optics Express* **2009**, *17*, 5953.

(206) Wang, Z.; Rhodes, D. A.; Watanabe, K.; Taniguchi, T.; Hone, J. C.; Shan, J.; Mak, K. F. Evidence of high-temperature exciton condensation in two-dimensional atomic double layers. *Nature* **2019**, *574*, 76–80.

(207) Duong, N. M. H.; Xu, Z. Q.; Kianinia, M.; Su, R.; Liu, Z.; Kim, S.; Bradac, C.; Tran, T. T.; Wan, Y.; Li, L. J.; Solntsev, A.; Liu, J.; Aharonovich, I. Enhanced Emission from WSe2 Monolayers Coupled to Circular Bragg Gratings. *ACS Photonics* **2018**, *5*, 3950–3955.

(208) De Leo, E.; Cocina, A.; Tiwari, P.; Poulikakos, L. V.; Marqués-Gallego, P.; Le Feber, B.; Norris, D. J.; Prins, F. Polarization Multiplexing of Fluorescent Emission Using Multiresonant Plasmonic Antennas. *ACS Nano* **2017**, *11*, 12167–12173.

(209) Moll, N.; Stöferle, T.; Schönenberger, S.; Mahrt, R. F. Ultra-high quality-factor resonators with perfect azimuthal modal-symmetry. *Optics Express* **2009**, *17*, 20998.

(210) Banerji, S.; Meem, M.; Majumder, A.; Vasquez, F. G.; Sensale-Rodriguez, B.; Menon, R. Imaging with flat optics: metalenses or diffractive lenses? *Optica* **2019**, *6*, 805.

(211) Molesky, S.; Lin, Z.; Piggott, A. Y.; Jin, W.; Vucković, J.; Rodriguez, A. W. Inverse design in nanophotonics. *Nature Photonics* **2018**, *12*, 659–670.

(212) Oh, S. H.; Altug, H.; Jin, X.; Low, T.; Koester, S. J.; Ivanov, A. P.; Edel, J. B.; Avouris, P.; Strano, M. S. Nanophotonic biosensors harnessing van der Waals materials. *Nature Communications* **2021**, *12*, 1–18.

(213) Seyler, K. L.; Schaibley, J. R.; Gong, P.; Rivera, P.; Jones, A. M.; Wu, S.; Yan, J.; Mandrus, D. G.; Yao, W.; Xu, X. Electrical control of second-harmonic generation in a WSe2 monolayer transistor. *Nature Nanotechnology* **2015**, *10*, 407–411.

(214) Hernandez-Rueda, J.; Noordam, M. L.; Komen, I.; Kuipers, L. Nonlinear Optical Response of a WS2Monolayer at Room Temperature upon Multicolor Laser Excitation. *ACS Photonics* **2021**, *8*, 550–556.

(215) Vashistha, V.; Vaidya, G.; Gruszecki, P.; Serebryannikov, A. E.; Krawczyk, M. Polarization tunable all-dielectric color filters based on cross-shaped Si nanoantennas. *Scientific Reports* **2017**, *7*, 1–8.

(216) Martinez, A. Polarimetry enabled by nanophotonics. *Science* **2018**, *362*, 750–751.

(217) Wilson, N. P.; Yao, W.; Shan, J.; Xu, X. Excitons and emergent quantum phenomena in stacked 2D semiconductors. *Nature* **2021**, *599*, 383–392.

(218) Lin, T. N.; Santiago, S. R.; Caigas, S. P.; Yuan, C. T.; Lin, T. Y.; Shen, J. L.; Chen, Y. F. Many-body effects in doped WS_2 monolayer quantum disks at room temperature. *npj 2D Materials and Applications* **2019**, *3*, DOI: `10.1038/s41699-019-0129-z`.

(219) Voronova, N. S.; Kurbakov, I. L.; Lozovik, Y. E. Bose Condensation of Long-Living Direct Excitons in an Off-Resonant Cavity. *Physical Review Letters* **2018**, *121*, 235702.

(220) Xiao, K.; Yan, T.; Liu, Q.; Yang, S.; Kan, C.; Duan, R.; Liu, Z.; Cui, X. Many-Body Effect on Optical Properties of Monolayer Molybdenum Diselenide. *Journal of Physical Chemistry Letters* **2021**, *12*, 2555–2561.

(221) Fogler, M. M.; Butov, L. V.; Novoselov, K. S. High-temperature superfluidity with indirect excitons in van der Waals heterostructures. *Nature Communications* **2014**, *5*, 1–5.

(222) Schneider, C.; Glazov, M. M.; Korn, T.; Höfling, S.; Urbaszek, B. Two-dimensional semiconductors in the regime of strong light-matter coupling. *Nature Communications* **2018**, *9*, 2695.

(223) Zhu, Q.; Tu, M. W. Y.; Tong, Q.; Yao, W. Gate tuning from exciton superfluid to quantum anomalous Hall in van der Waals heterobilayer. *Science Advances* **2019**, *5*.

(224) Robert, C.; Lagarde, D.; Cadiz, F.; Wang, G.; Lassagne, B.; Amand, T.; Balocchi, A.; Renucci, P.; Tongay, S.; Urbaszek, B.; Marie, X. Exciton radiative lifetime in transition metal dichalcogenide monolayers. *Physical Review B* **2016**, *93*, 1–10.

(225) Shi, J.; Lin, M. H.; Chen, I. T.; Estakhri, N. M.; Zhang, X. Q.; Wang, Y.; Chen, H. Y.; Chen, C. A.; Shih, C. K.; Alu, A.; Li, X.; Lee, Y. H.; Gwo, S. Cascaded exciton energy transfer in a monolayer semiconductor lateral heterostructure assisted by surface plasmon polariton. *Nature Communications* **2017**, *8*, 1–6.

(226) Hotta, T.; Higuchi, S.; Ueda, A.; Shinokita, K.; Miyauchi, Y.; Matsuda, K.; Ueno, K.; Taniguchi, T.; Watanabe, K.; Kitaura, R. Exciton diffusion in hBN -encapsulated monolayer $MoSe_2$. *Physical Review B* **2020**, *102*, 115424.

(227) Choi, J. et al. Moiré potential impedes interlayer exciton diffusion in van der Waals heterostructures. *Science Advances* **2020**, *6*, 1–7.

(228) Dutra, S. M.; Knight, P. L. Spontaneous emission in a planar Fabry-Pérot microcavity. *Physical Review A - Atomic, Molecular, and Optical Physics* **1996**, *53*, 3587–3605.

(229) Chen, G. H.; Li, D. Z.; Butcher, A.; High, A. A.; Chang, D. E. Engineering the radiative dynamics of thermalized excitons with metal interfaces. *New Journal of Physics* **2022**, *24*, 023015.

(230) Park, J. H.; Ambwani, P.; Manno, M.; Lindquist, N. C.; Nagpal, P.; Oh, S. H.; Leighton, C.; Norris, D. J. Single-crystalline silver films for plasmonics. *Advanced Materials* **2012**, *24*, 3988–3992.

(231) Went, C. M.; Wong, J.; Jahelka, P. R.; Kelzenberg, M.; Biswas, S.; Hunt, M. S.; Carbone, A.; Atwater, H. A. A new metal transfer process for van der Waals contacts to vertical Schottky-junction transition metal dichalcogenide photovoltaics. *Science Advances* **2019**, *5*, 1–9.

(232) Liu, Y.; Guo, J.; Zhu, E.; Liao, L.; Lee, S. J.; Ding, M.; Shakir, I.; Gambin, V.; Huang, Y.; Duan, X. Approaching the Schottky-Mott limit in van der Waals metal-semiconductor junctions. *Nature* **2018**, *557*, 696–700.

Appendix A

Nanofabrication Recipes and Notes

Table A.1 – E-beam lithography parameters for nanophotonic device templates in PMMA. Resist thickness was typically 275-475 nm, depending on targeted device height.

E-beam lithography parameters	
Beam step size	0.002 µm
Writing resolution	0.0005 µm
Multipass exposure	4x
Dose	175-300 uC/cm2
Beam current	0.3 nA
High resolution mode	True
Fracturing mode	LRFT

Table A.2 – TiO_2 atomic layer deposition parameters. Typical deposition rate was 0.061 nm/cycle.

TiO_2 atomic layer depsotion recipe	
N_2 flow rate	100 sccm
Chamber temperature	90 C
TDMAT pulse	0.08 s
TDMAT purge	5 s
Stop valve closed	-
Water pulse	0.1 s
Wait	2.9 s
Stop valve opened	-
Water purge	7 s

Table A.3 – ICP chlorine etch parameters. Typical etch rates are 1.5-1.7 nm/s.

ICP chlorine etch recipe	
Substrate bias	150 W
ICP power	400 W
Cl_2 flow	12 sccm
BCl_3 flow	8 sccm

Table A.4 – Single-crystal silver deposition parameters. Epitaxy was successful on cleaved mica.

Single-crystal silver deposition	
Base pressure	3.5×10^{-6} Torr
Substrate temperature	350 C
Soak 1 power	25%
Soak 1 time	180 s
Soak 2 power	40%
Soak 2 time	30 s
Deposition rate	1.7 nm/s
Deposition thickness	> 300 nm